POLITECNICO
MILANO 1863

SCUOLA DI INGEGNERIA INDUSTRIALE
E DELL'INFORMAZIONE

HALOGEN BONDING IN 2D HYBRID HALIDE PEROVSKITES

Synthesis, Structural Characterization and Photophysical Properties

TESI DI LAUREA MAGISTRALE IN MATERIALS ENGINEERING AND NANOTECHNOLOGY - INGEGNERIA DEI MATERIALI E DELLE NANOTECNOLOGIE

Author: **Alessandra Panizza**

Student ID:	941368
Supervisor:	Gabriella Cavallo
Academic Year:	2020-2021

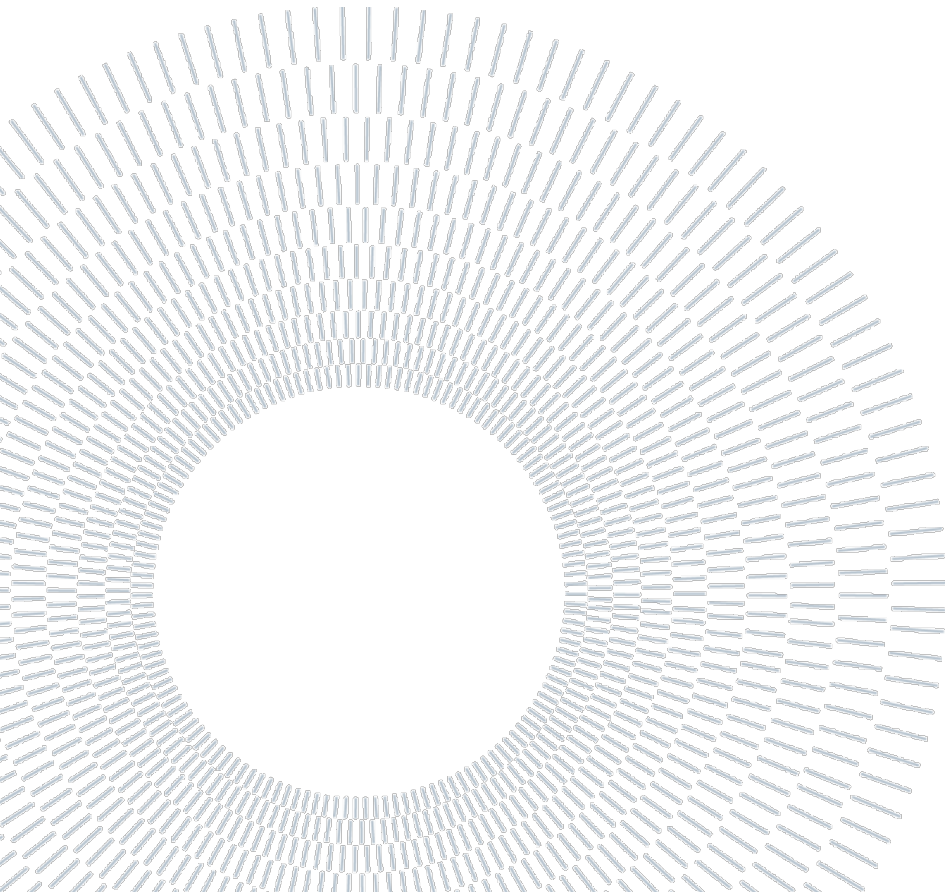

Abstract

Hybrid perovskites are attracting growing interest in the optoelectronic field since they combine both organic and inorganic advantages, emerging as promising replacements of other commercial semiconductors. Despite the competing costs and efficiencies of perovskite-based devices, stability stands as the main factor which has limited their marketing, to date. A recent strategy widely adopted by researchers to overcome this issue is the introduction of functional templating cations in perovskite lattice, able to build organic-inorganic interactions stabilizing the structure and leading to the formation of low-dimensional perovskites due to their large size. Among all the possible intermolecular interactions, halogen bond (XB) comes out as a peculiar tool due to its unique characteristics. In this work, the role of XB in layered 2D lead iodide perovskites has been explored, trying to correlate the structure with the optical properties of these materials. New low-dimensional perovskites were synthesized by selecting different aromatic XB-donors as organic ammonium mono-cations. The occurrence of XB between organic and inorganic domains has been proven, directly or indirectly, and the tunability of its strength has been investigated, also in correlation with structural constraints and nature of XB-acceptor. In particular, 4-iodoanilinium (IA) and (4-X-2,3,5,6-tetrafluoroaniline)-ethan-1-ammonium (X-FEA, with X = Cl, Br, I) cations have been chosen as weaker and stronger XB-donors, respectively. XRD and NMR have been exploited to understand the crystalline structure of the materials, while TGA and DSC have been conducted to study their thermal properties. Vibrational modes and binding energies associated to XB-donor synthons have been also examined by Raman and FT-IR spectroscopies and XPS, respectively, in order to identify the binding mode of organic cations. This wide characterization allowed to put forward some hypotheses about possible rotational dynamics of X-FEA cations in perovskite lattice. The assumption was further supported by UV-vis absorption and PL measurements. This study suggests that XB can be applied as a powerful tool to control structure and photophysical properties in low-dimensional perovskites, hence paving the way towards the development of highly stable materials with tunable dimensionality and functional properties.

Key-words: *2D perovskites · halogen bond · aromatic cations · crystalline structures*

Abstract in lingua italiana

Le perovskiti ibride stanno attirando un interesse crescente nel campo optoelettronico poiché combinano sia vantaggi organici che inorganici, emergendo come promettenti sostituti di altri semiconduttori commerciali. Nonostante le efficienze e i costi competitivi dei dispositivi a base perovskitica, la stabilità è il fattore principale che ha limitato la loro commercializzazione, ad oggi. Una recente strategia ampiamente adottata dai ricercatori per cercare di risolvere questo problema è l'introduzione di cationi funzionali nel reticolo, in grado di costruire interazioni organico-inorganiche che stabilizzino la struttura e portino alla formazione di perovskiti bidimensionali a causa del loro maggiore ingombro sterico. Tra tutte le possibili interazioni intermolecolari, il legame ad alogeno (XB) emerge come un interessante strumento grazie alle sue caratteristiche uniche. In questo lavoro, è stato esplorato il ruolo del XB in perovskiti stratificate 2D, cercando di correlare la struttura con le proprietà ottiche di questi materiali. Sono state sintetizzate nuove perovskiti a bassa dimensionalità selezionando diversi donatori aromatici di XB come monocationi organici. È stata dimostrata la presenza di XB tra domini organici e inorganici e ne è stata studiata l'intensità, al variare anche dei vincoli strutturali e della natura dell'accettore di XB. In particolare, i cationi 4-iodoanilinio (IA) e (4-X-2,3,5,6-tetrafluoroanilina)-etan-1-ammonio (X-FEA, con X = Cl, Br, I) sono stati scelti come donatori più deboli e più forti di XB, rispettivamente. XRD e NMR sono stati sfruttati per capire la struttura cristallina dei materiali, mentre TGA e DSC sono stati condotti per studiare le loro proprietà termiche. I modi vibrazionali e le energie di legame associati ai sintoni dei donatori di XB sono stati esaminati tramite le spettroscopie Raman e FT-IR e XPS, rispettivamente, così da verificare le modalità di legame dei cationi organici. Questa ampia caratterizzazione ha permesso inoltre di avanzare alcune ipotesi sulla possibile dinamica rotazionale dei cationi X-FEA nel reticolo della perovskite. Tale teoria è stata ulteriormente supportata dalle misure di assorbimento UV-vis e PL. Questo studio suggerisce che XB può essere impiegato come potente strumento per il controllo della struttura e delle proprietà fotofisiche in perovskiti a bassa dimensionalità, aprendo quindi la strada verso lo sviluppo di materiali ad alta stabilità con dimensionalità e funzionalità variabili.

Parole chiave: *perovskiti 2D · legame ad alogeno · cationi aromatici · strutture cristalline*

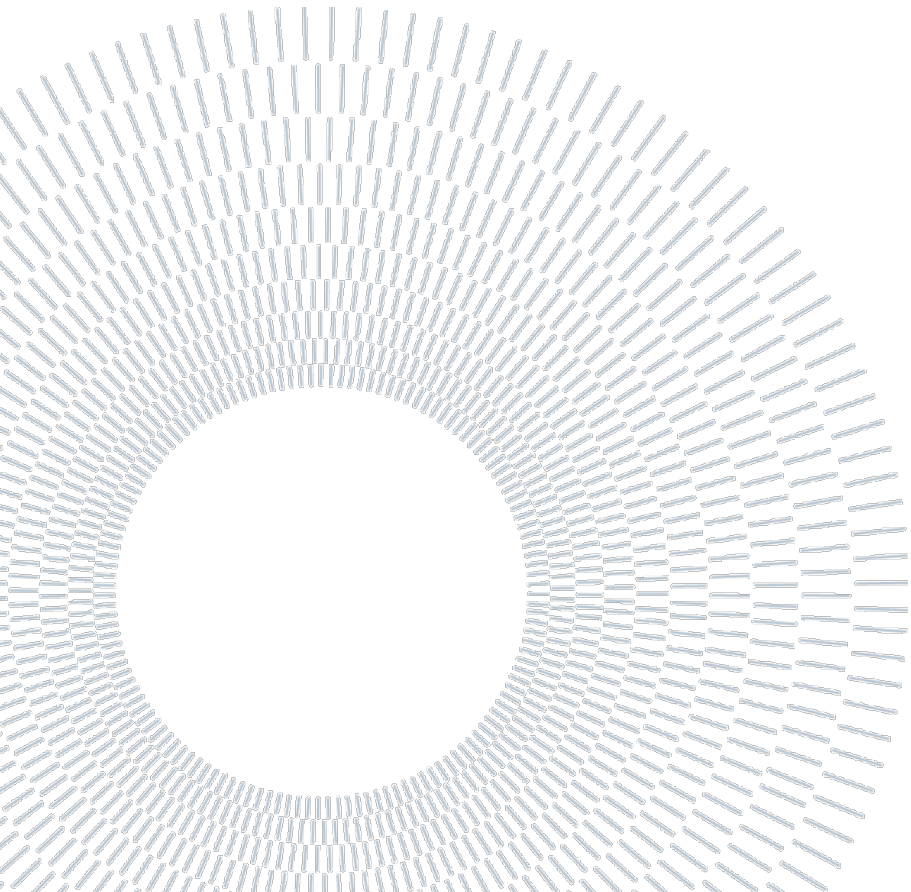

Contents

Introduction

General Structure and Classification of Perovskites

Originally discovered perovskite, found in the Ural Mountains of Russia by Gustav Rose in 1839 and named after Russian mineralogist Lev Perovski, is a calcium titanium oxide mineral ($CaTiO_3$) and it gives its name to all the other synthetic crystals with the same structure ABX_3, where A and B are cations – generally A larger than B - and X is an anion. The ideal cubic structure has the B cation in 6-fold coordination, surrounded by an octahedron of anions, and the A cation in 12-fold cuboctahedral coordination (Figure 1).[1] A large number of different elements can be combined together to form perovskite structures; therefore, a first classification can be done by considering their chemical nature. *Inorganic oxide perovskites* contain O^{2-} anions – like the original mineral – while *halide perovskite*s are based on halide anions, like Cl^-, Br^- or I^-. B is typically a bivalent cation belonging to the IV group in the periodic table, like Ge, Sn or Pb, while A is a monovalent cation from the I group, like K, Rb or Cs – affording to *alkali-halide perovskites* – or an organic molecule – providing *organo-metal halide perovskites* (Figure 2).

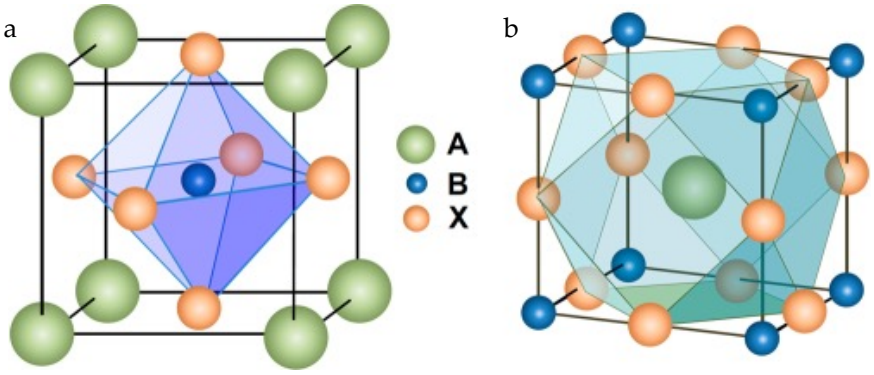

Figure 1. *Schematic 3D representation of the ideal cubic structure of the perovskite crystal cell, highlighting (a) BX_6 octahedral and (b) AX_{12} cuboctahedral geometry.*[1]

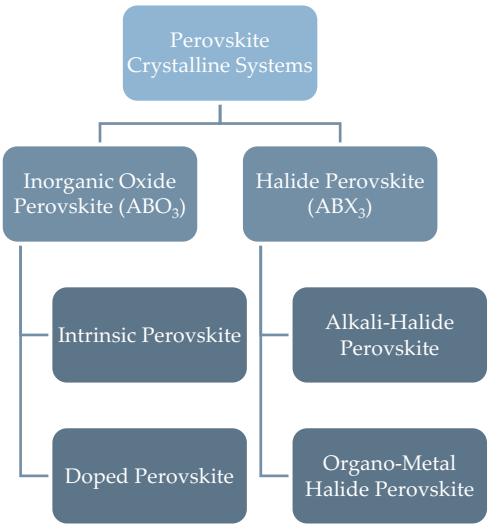

Figure 2. *Classification of perovskites based on their composition.*[1]

The choice of each of these elements will influence the structure and consequently the properties of the material. For example, for a fixed B cation, increasing the size of the halogen will induce an increase in the lattice parameter and a more covalent character in the B-X bond as a consequence of the lower electronegativity of the halogen. This provides a red shift in the absorption spectrum and a decrease in the band gap. Whereas tuning B cation, for example from germanium to tin to lead, leads to an increase of the B^{II} oxidation state stability, indeed lead is typically preferred in terms of stability of the material and efficiency of the device, although its toxicity raises some concerns. Thus, in order to avoid toxicity, research efforts are devoted to replace Pb with Sn or Ge. Finally, A cation is the most tunable species, leading to the biggest modifications, both in chemical-physical properties and crystal structure. In particular, exploiting organic cations of different size affords to perovskites with lower dimensionality (*i.e.* 2D, 1D or 0D) with interesting implications in material properties.[1,2]

Geometric Parameters

The relative ion size requirements for stability of the cubic structure are quite stringent, so slight buckling and distortion can produce several lower-symmetry distorted structures, in which the coordination numbers of A cations, B cations or both are lower than those in the cubic structure. Many physical properties of perovskites depend crucially on the details of these distortions, particularly the electronic, magnetic and dielectric properties, which are very important for several applications of perovskite materials. For perovskites, the measure of the mismatch between the average equilibrium A–X and B–X bond lengths is expressed by the semiempirical formula of the Goldschmidt's tolerance factor:

$$t = \frac{R_A + R_X}{\sqrt{2}(R_B + R_X)} \qquad (1)$$

where R_A, R_B and R_X are the ionic radii of A, B and X, respectively. Generally, ABX_3 can crystallize into orthorhombic, tetragonal, and cubic polymorphs (Figure 3). The stabilization of the material in a certain phase strongly depends on tolerance factor. The ideal perovskite cubic structure requires t to be in the range from 0.813 to 1.107 and ideally close to 1.[3,4] When t < 0.813, lower-symmetry phases will appear. The smaller the A-site cation, the lower is the t value. In fact, in this case the A cation is too small to fit in the cavities between the BX_6 octahedra. On the other hand, when the t value is greater than 1.11, it indicates that the A-site cations are too large to have an octahedral framework and 2D layered structures, one dimensional (1D) chain structures, and even zero dimensional (0D) isolated clusters can be formed. Therefore, measuring the radius of various ions is critical to determine the proper tolerance factor, which allows to estimate through simple geometric consideration whether a stable perovskite structure can be formed. Note that t is not the only prediction criteria. Octahedral factor μ is another parameter for predicting stable crystal structure of perovskite materials. A μ value between 0.442 and 0.895 usually results in stable perovskite structures.[3,4] The octahedral factor is given by the formula:

$$\mu = \frac{R_B}{R_X} \qquad (2)$$

and it can be used to empirically evaluate whether a B-site atom prefers an octahedral coordination of the X-site atom.[3–7]

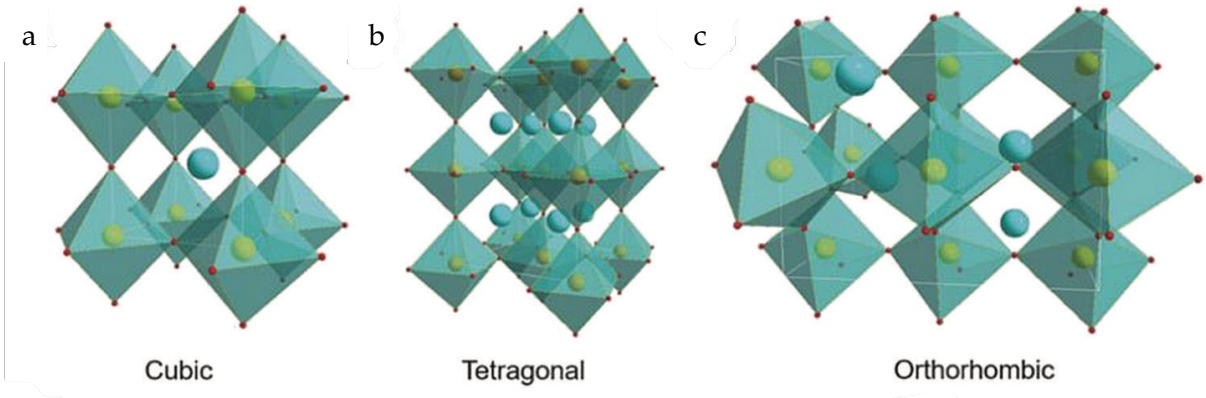

Figure 3. *The crystal structures of perovskite materials with different symmetries: (a) cubic phase, (b) tetragonal phase, and (c) orthorhombic phase.*[7]

The most studied organic inorganic halide perovskites are $(CH_3NH_3)BX_3$ and $(CH(NH_2)_2)BX_3$, where methylammonium (MA) and formamidinium (FA) substitute the typical inorganic A-site cations (Cs^+, Ru^+, K^+) of all-inorganic halide perovskites. Considering, for example, organolead halide perovskites, tolerance factors for $(CH_3NH_3)PbX_3$ are calculated at 0.85, 0.84, and 0.83 for X = Cl, Br, and I, respectively, based on the radii of MA^+ = 180 pm, Pb^{2+} = 119 pm, Cl^- = 181 pm, Br^- = 196 pm, and I^- = 220 pm. Thus, methylammonium lead halide perovskites are expected to have a cubic structure, maintaining the 3D geometry.[3,4,7]

Hybrid Halide Perovskites: Properties and Applications

Hybrid organic inorganic halide perovskites have attracted more and more researchers in the last decades because they are direct band gap semiconductors which combine the advantages of both organic (facile and cheap solution processability) and inorganic (high charge carriers mobility) materials, making them competitive with all the other semiconducting materials, especially in optoelectronic field. Their intrinsic ambipolar transport, high optical absorption coefficient, intense PL, changeable band gap, high quantum efficiency and long carrier diffusion are the physical, electrical and photophysical properties that make hybrid halide perovskites excellent candidates for optoelectronic devices, such as solar cells (SCs), light-emitting diodes (LEDs), light-emitting electrochemical cells (LECs), LASERs (Light Amplification by Stimulated Emission of Radiation), field-effect transistors (FETs), photodetectors.

By virtue of their tunable low band gap, perovskites have been applied as light absorbers in dye-sensitized solar cells (DSSCs, Figure 4a). The perovskite absorbers showed superior advantages over traditional dyes by much more strongly absorbing over a broader range, enabling complete light absorption in films as thin as 500 nm. The ionic nature of this material leads it to easily dissolve and degrade in organic liquid electrolyte, thus, initial perovskite solar cells were unstable. The employment of solid-state electrolytes as hole transport materials (HTL) helped in overcoming these problems, increasing the power conversion efficiencies (PCE) of the devices. When perovskite was discovered to be not only a strong absorber, but also an efficient charge transport material, thanks to its crystallinity, it was employed for building a new class of solar cells (SCs), different from DSSCs (Figure 4b,c). Moreover, the presence of organic cations in the lattice brings the further advantages of solution processability and optical property tunability. It is not often that such a cheap and easily available material can perform all the three basic tasks required in solar cell operation, that is, light absorption, carrier generation, and ambipolar transport. Power conversion efficiencies (PCEs) have overcome values of 20%, thanks to the molecular engineering of HTL[8] and to the improved crystalline morphology of perovskite layer[9].

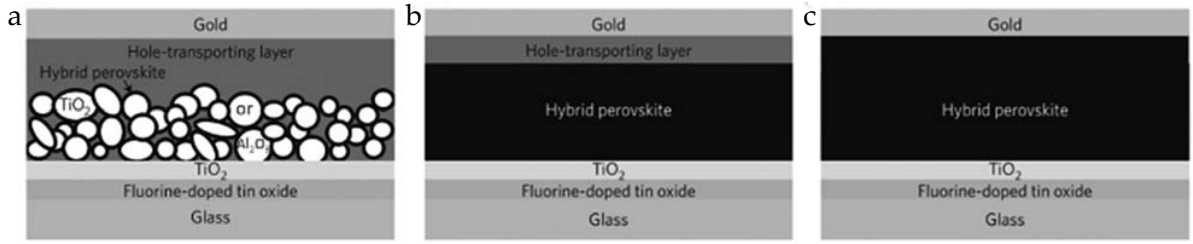

Figure 4. *Architectures of typical perovskite solar cells: from (a) dye-sensitized solar cells to (c) perovskite solar cells.*[1]

General photodetectors, that convert incident light into electrical signals, are critical for a variety of industrial and scientific applications such as optical communications, environmental monitoring, day- and night-time surveillance and chemical/biological sensing. Hybrid organic inorganic perovskites have also good emission optical properties, like photoluminescence (PL), making them suitable for LEDs and LECs.

Benefiting from large exciton binding energy and low defect density, organic inorganic halide perovskites exhibit superior performance also in lasing. The wide tunability of emission color across the visible spectrum, combined with the facile solution growth technique, make lead halide perovskites excellent material for implementing nanostructured lasers in a wide range of applications, such as nanophotonics, optical computing and chemical/biological sensing.

Unlike traditional inorganic semiconductors, the low-temperature solution process enables organometal halide perovskites to deposit on a broader range of substrate materials such as plastics, opening up opportunities to flexible electronic and photonic applications.[1,10]

Among all the advantages provided by perovskites in optoelectronics - absorption coefficient, long electron and hole diffusion lengths, low exciton binding energies, low effective masses and high mobilities - the presence of only shallow defects in the bandgap emerges. This peculiar feature, attributed also to some other semiconductors, tie to the presence of filled Pb 6*s* orbitals, deriving from the partial oxidation of Pb relative to its Pb^{4+} oxidation state. In the model applied by R. E. Brandt *et al.* to $MAPbI_3$[11], and previously pioneered by Zhang, Lany, Zakutayev *et al.* for $CuInSe_2$[12], defect tolerance emerges from having bonding orbitals at the conduction band

minimum (CBM), and antibonding orbitals at the valence band maximum (VBM), exceptional condition with respect to most of semiconductors. The defect tolerance deriving from such an electronic structure is easily described using atomic vacancies as examples. Namely, if predominantly antibonding orbitals occur at the VBM and bonding at the CBM, the dangling bonds that are formed upon creating the vacancy (of any kind) will likely appear as resonances inside the bands, leaving the bandgap free of deep states that could act as carrier traps. As shown in Figure 5 for the valence band of $MAPbI_3$, this is a consequence of the position of valence atomic orbitals relative to the bonding and antibonding bands formed due to interactions. Analogous considerations are also valid for other types of intrinsic defects, such as interstitials and/or anti-sites, as well as for structural defects such as grain boundaries, which consist of many dangling bonds. The electronic bandgap is formed between the antibonding VBM, originating from the Pb(6*s*)-I(5*p*) interactions, and the antibonding CBM resulting from the Pb(6*p*)-I(5*p*) interactions. Bonding-type defect-tolerance can, therefore, only be applied to the defects that would tend to create valence band-derived states, such as cation (Pb or MA) vacancies. On the other hand, if anion (I^-) vacancies form, the resulting dangling bonds will appear as resonances inside the conduction band only if the bandwidth and the dispersion of the conduction band are such that the CBM falls well below the energy of the Pb(6*p*) atomic orbitals. In the case of Pb, contrary to Sn and Ge compounds, for example, this condition is more likely due to relativistic spin-orbit interaction effects that increase the width of the Pb(6*p*) conduction band.[13] Thus, Pb(*6p*) and I(*5p*) orbital hybridization and the overlap between the Pb(*6s*) and I(*5p*) orbitals make common vacancies fall inside or near the edges of the energy band so as not to form deep traps that cause the carriers to be trapped (Figure 6).[11] Importantly, due to the formation energy of the defects being much larger than that of the vacancy, they rarely appear in the perovskite material system and the high dielectric constant of the perovskite system also contributes to the tolerance of defects.[7]

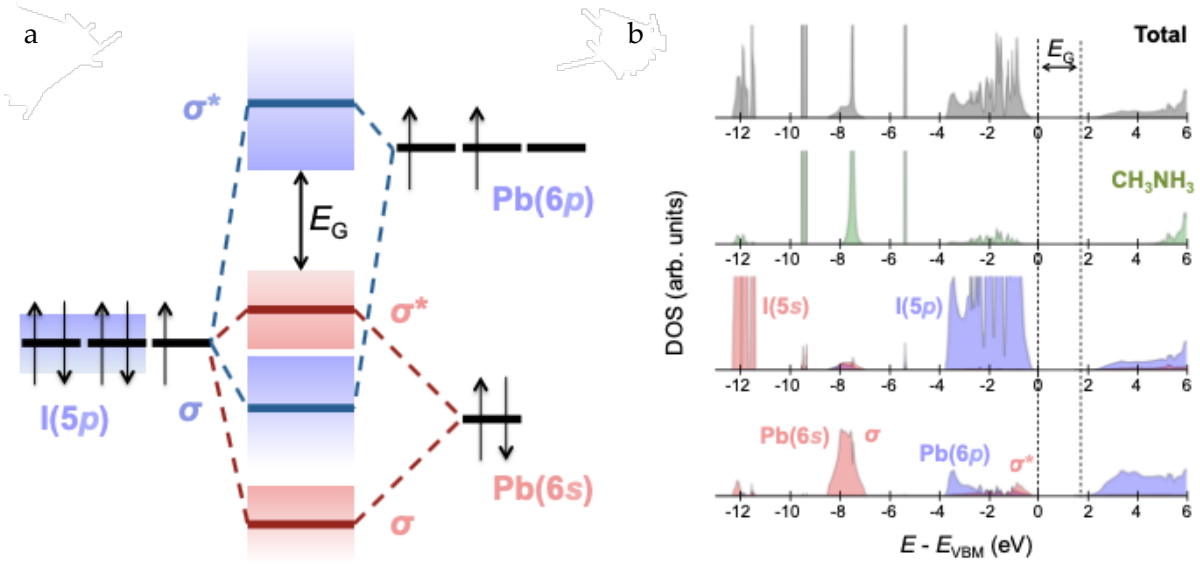

Figure 5. *(a) Bonding/antibonding orbitals in $MAPbI_3$; (b) Density of states (DOS) of $MAPbI_3$ separated into cation and anion s and p orbital contributions. The MA^+ cation does not introduce states at the band edge.*[13]

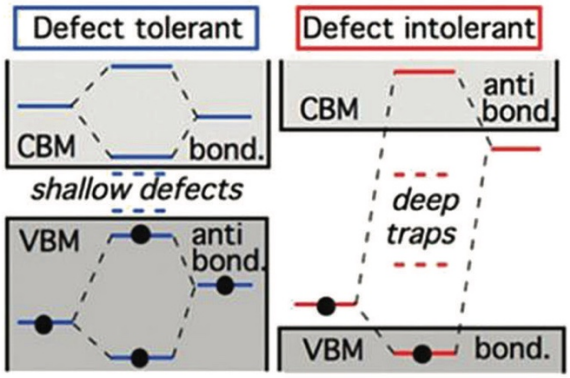

Figure 6. *The relationship between defect tolerance and the energy band structure.*[11]

Hybrid materials can also combine the advantages of organic and inorganic materials in terms of excitonic characteristics, which are fundamental since the optical properties

near and below the band gap are dominated by the exciton transitions. Excitons correspond to a bound state of one electron and one hole and can be created by light (SCs) or can appear as a result of relaxation processes of free electrons and holes, which, for example, may be injected electrically (LEDs). The two main models used to classify these quasi-particles are: large-radius and low-energy Wannier-Mott exciton for inorganic semiconductors, and small-radius and high-energy Frenkel model for molecular crystals. The different excitonic radius (electron-hole distance) and, thus, the different exciton binding energy, in organic and inorganic materials is mainly due to the different screening potential. Hybrid structures, in which Frenkel and Wannier excitons are in resonance with each other and coupled through their dipole–dipole interaction at the interface, can combine both large radius of Wannier excitons, leading to good transport of charge carriers, and high oscillator strength of Frenkel excitons, as demonstrated by D. Basko *et al.* at a covalent-semiconductor/molecular-solid interface.[14,15]

Limitations on 3D Structure

Despite all characteristics and properties matching the requirements in optoelectronic field, there are still two main challenges to overcome: how to fabricate large areas and high quality devices, since usually their energy conversion efficiencies decline quickly with the increased active areas; and how to increase the device stability, since the soft ionic structure, which allows the presence of a charge in the form of local lattice distortions, or polarons, that shield carriers and lower the energetic barrier to charge separation, suffer also from environmental instability and degradation. Moisture and oxygen, which tend to interact with organic cations, together with heat and light itself, have been proved to be the main factors causing the degradation of organometal halide perovskites.

In addition, due to the ionic nature and solution processability, perovskite thin films unavoidably possess noteworthy levels of impurities and defects. Taking $MAPbI_3$ as an example, undercoordinated $Pb^{2+}/^{1+}/^{0}$ and $I^{1+}/^{0}$ are two typical defects in perovskites, including mobile I^- anions, I_2 interstitials, undercoordinated MA^+ and $Pb^{2+}/^{1+}$ cations, and Pb^0 clusters. The undercoordinated ions induce a local excess of positive or

negative charges, *i.e.*, the loss of I^- induces a positive charge on the Pb atom, while uncoordinated I^- anions cause excess negative charges. These charged sites are able to trap photoexcited electrons and holes, lowering the photon-to-electron conversion efficiency of the photovoltaic device.[16] The addition of a small amount of I_2 or an excess of PbI_2 at the grain boundaries could theoretically avoid I^- defects by passivating them, but in both cases the material can undergo photodecomposition due to irreversible degradation of I_2 molecules and generation of metallic Pb that are deleterious to device stability.[5,17–21] Although perovskites have superior defect tolerance benefiting from their inherently defect-tolerant electronic structure, as previously mentioned, the perovskite-based device efficiency could be strongly affected, besides the fact that extrinsic impurities could still introduce deep traps inside the bandgap depending on the position of their atomic orbitals relative to the energy bands of the host material.[13] Non-radiative recombination induced by the inevitably deep traps still limit the carrier lifetime and cause energy losses, which act as barriers for solar cells to reach the Shockley–Queisser limit (33.5%, achievable by GaAs cells).[22] Moreover, the more pronounced ion migration at the grain boundaries, accelerated by defects, speeds up the degradation process and reduces the stability of optoelectronic devices.

Furthermore, perovskites are unstable in the presence of many polar solvents, still because of their ionic crystal attributes. MA^+, for example, gives higher photo-induced instability than FA^+, and both the organic cations leads to the formation of more volatile products than Cs^+, having the most stable structure among the three. Additionally, tunability of optoelectronic properties is restricted by a limited selection of cations which must fit the geometrical parameters.

Therefore, in order to exploit the advantages of hybrid organic-inorganic devices, some strategies must be applied to increase the chemical, thermal and photochemical stability, but also to improve all the other properties, maintaining high device efficiencies.[11,12] An important contribution to the improvement in device stability has been done with the introduction of low dimensional perovskites.

Low-Dimensional Perovskites

By increasing the size of the A cation, thus increasing tolerance factor (eq. (1)), the structure reduces its symmetry, arranging in lower dimensionalities with respect to the standard 3D one. 2D, 1D and 0D perovskites are getting more and more attractive because of their higher stability and tunability with respect to 3D ones. The dimensionality is given by the quantum confinement of the inorganic sublattice, since it is possible to model the alternated organic and inorganic layers of 2D perovskites with quantum wells, the inorganic chains of 1D perovskites as quantum wires and the isolated octahedrons of 0D ones as quantum dots (Figure 7).
The wider selection of A cations allows to expand the energy gap tunability and to introduce further intermolecular interactions that can strengthen and stabilize the structure. A higher stability with respect to 3D is also given by the lower volatility of the bigger organic cations and by the metal halide isolation, which slow down the material degradation.

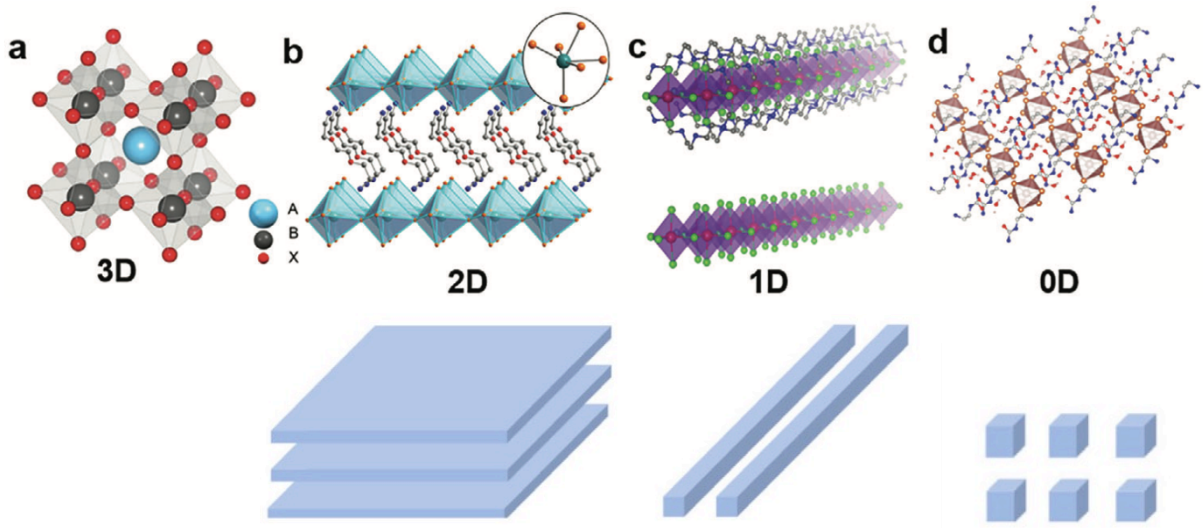

Figure 7. *Dimensional reduction at the molecular level and quantum confinement.*[25]

Even though lower dimensionalities present numerous advantage (easily tunable photo response, shorter response time and better stability), the higher crystallinity of 3D perovskites makes them still the most efficient charge-transport materials. One of the highest reported values of PCE in 2D perovskite SCs is around 18%, which is still much lower than that of 3D ones (25%).[6] Thus, instead of being directly used as solar cells absorbers, low-dimensional perovskites find suitable application as integration of 3D perovskite-based devices, enhancing the surface properties of 3D perovskite grains and films.

For example, the fabrication of solar cells containing 2D/3D mixed perovskite active layer is often chosen for the higher stability maintaining a high efficiency. 2D layers are introduced in the lattice in order to passivate the undercoordinated species and to strengthen the interactions. Thus, they will be located where undercoordinated species gather: at the surface, forming an interlayer between 3D perovskite and HTL and favoring the charge transport across the device as showed in Figure 8, and at the grain boundaries, preventing the accumulation of defects which can act as trap sites for charges moving across the perovskite grains (Figure 9).

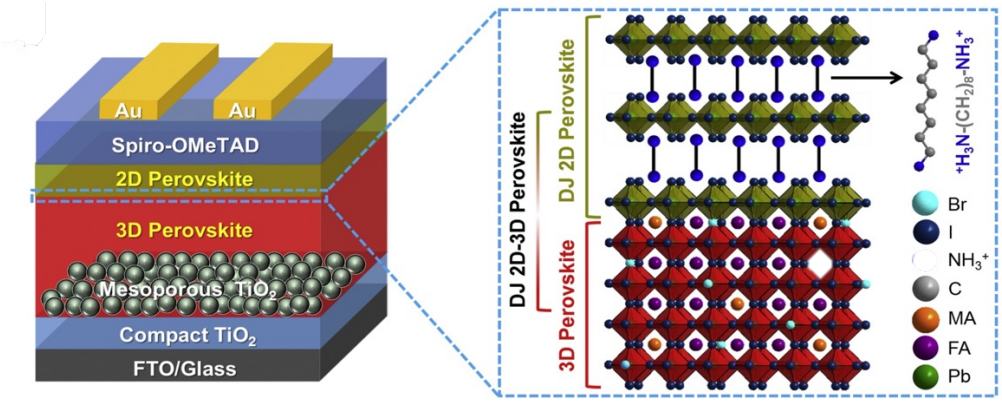

Figure 8. *Schematic illustration of 2D-3D perovskite and SC architecture.*[26]

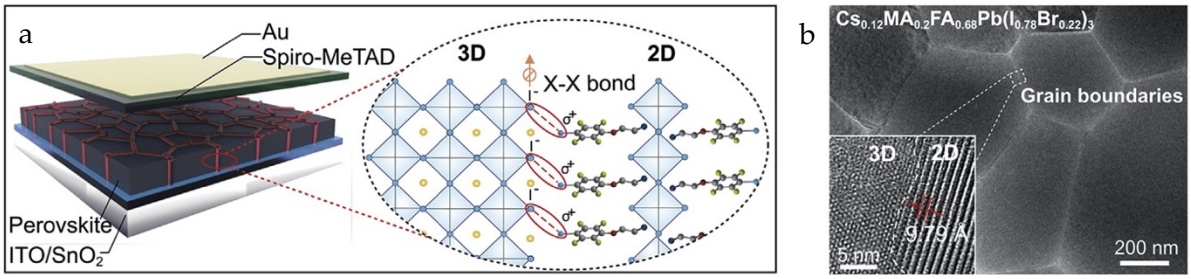

Figure 9. *(a) Schematic illustration of 2D-3D perovskite interactions and SC architecture. (b) TEM image demonstrating the presence of 2D perovskite at the grain boundaries.*[27]

Due to the size effect and significant differences in dielectric constants between the organic and inorganic parts, excitons in low dimensional perovskites are spatially confined. This suppresses the separation of excitons and greatly improves the radiation recombination efficiency. Therefore, organic–inorganic low dimensional perovskites are considered to be good candidate materials for stable LEDs with high photoluminescence quantum yield (PLQE). Some 0D hybrid perovskite nanocrystals have been reported as efficient broadband phosphors (Figure 10a), showing great light-emitting performance up to 85% of PLQE and excellent thermal stability, and making the materials attractive candidates also for white light-emitting diodes (WLEDs) manufacturing. 2D hybrid perovskites have also showed broadband white-light-emitting (Figure 10b,c; *N*-MEDA = N^1-methylethane-1,2-diammonium; EDBE = 2,2-(ethylenedioxy)), with emission almost covering the entire visible spectrum and PLQE up to 18%, due to the formation of self-trapped excitons in the deformable lattice.[25] Exciton self-trapping occurs in a wide variety of materials in presence of a deformable lattice. They form when excitons couple with the soft lattice, inducing elastic structural distortions that lower the system's energy (Figure 11), similarly to small polarons. Unlike free exciton states (FE) PL, STE luminescence is typically broad and significantly Stokes shifted from the FE absorption. The distortion of the self-trapped state with respect to the ground state (GS) - given by the Huang–Rhys parameter, S - broadens the emission. Both S and the stabilization of the self-trapped state with respect to the untrapped state (self-trapping depth) contributes to the Stokes shift.[28]

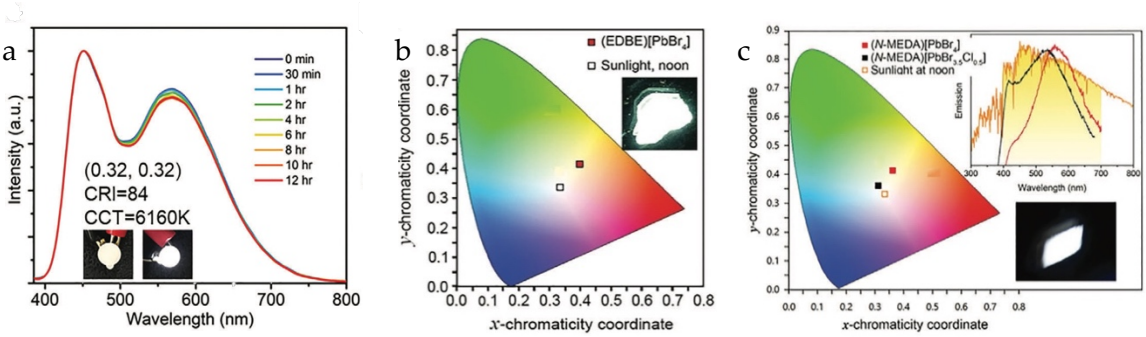

Figure 10. *(a) Emission stability and luminous performance of 0D $(C_4N_2H_{14}Br)_4SnBr_3I_3$ LED. (b) CIE coordinates of (EDBE)($PbBr_4$) and sunlight at noon. Inset is a photograph of (EDBE)($PbBr_4$) under 365 nm irradiation. (c) CIE coordinates and emission spectrum of white-light emitters and sunlight at noon. Inset is a photograph of (N-MEDA)($PbBr_4$) under 380 nm irradiation.*[25]

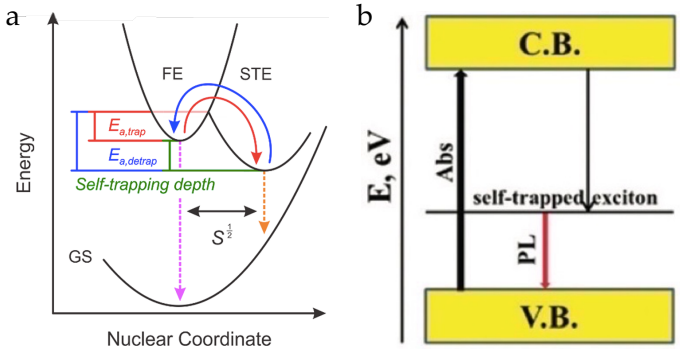

Figure 11. *Two examples of energy diagram representing self-trapped exciton.*[28,29]

In addition, it is has been demonstrated that low dimensional perovskites have higher PCEs, faster decay and larger Stokes shifts compared with 3D ones. These advantages demonstrate their potential for large-area and low-cost scintillator devices in the fields of medical imaging, nondestructive detection and space exploration. For example, some 2D perovskites exhibited less thermal quenching than analogous 3D due to the large exciton binding energy so that moderate light yield could be obtained even at room temperature. 2D perovskite-based scintillators have been applied for alpha particle detection, X-ray imaging and discrimination between alpha particles and

gamma-rays. At the same time, low dimensional perovskites have shown potential in transducer field due to their adjustable structural phase transition and fluorescence emissions, with application of 0D hybrid ones as gas sensor for acetone detection.[25]

Purpose of the Experimental Work

The experimental work focused on studying the effects of halogen bond on structure, optoelectronic properties and stability of 2D perovskites by selecting suitable templating organic cations. The design of the cation (Figure 12) aimed at creating a highly electropositive σ-hole along C-I bond axis, thanks to the fluorination of the aromatic ring, such that it could anchor to the exposed halide anions from lead iodide octahedra of two different inorganic layers, on one side through ionic bonding with the protonated primary aminic group ending the alkyl chain, and on the opposite extremity through halogen bonding with iodine atom, strongly stabilizing the structure. Its effects on perovskite properties were compared with other 2D perovskites containing weaker or no XB.

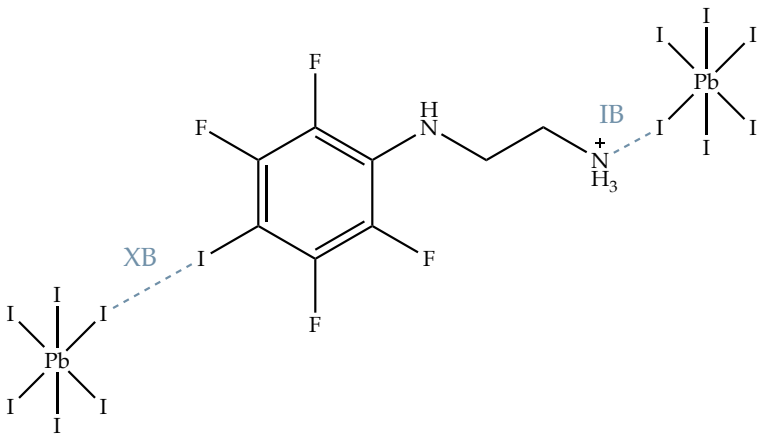

Figure 12. *Schematic structure of the cation which can potentially form strong halogen bond with inorganic octahedron.*

1. 2D Hybrid Halide Perovskites

1.1 Structure

2D hybrid halide perovskites are layered crystalline materials constituted by sheets of inorganic corner-sharing octahedra BX_6 (B = Pb^+, Sn^+, Ge^+; X = I^-, Br^-, Cl^-), typically lead iodide octahedra, alternated with layers of larger organic monovalent (m = 2) or divalent (m = 1) cations (A'), resulting in compositions of formula A'_mBX_4. Generalizing, the formula becomes $A'_mA_{n-1}B_nX_{3n+1}$, where n represents the dimensionality of the system, and it precisely indicates the number of inorganic sheets placed between each organic layer. Thus, strictly defined 2D perovskites have n = 1, 3D perovskites have $n = \infty$, while all the other intermediate structures with $n \geq 2$ are properly called *quasi*-2D perovskites and contain both the large bulky organic cation A' of 2D and small cation A (MA^+, FA^+, Cs^+) of 3D (Figure 13a). More properly, the above mentioned formula refers to the common ⟨100⟩-oriented *quasi*-2D crystal, but there are other possibilities as shown in Figure 13b. 2D perovskites can be imagined as "cleaving" the 3D structure along a crystallographic plane to form sheets, adding halide ions to satisfy the surface metal coordination sites. The cleaving can be along the ⟨100⟩-, ⟨110⟩-, and ⟨111⟩-planes of the 3D structure, giving rise to ⟨100⟩-, ⟨110⟩-, and ⟨111⟩-oriented 2D perovskites, respectively.[6,30–32]

All the 2D hybrid halide perovskites that do not pertain to these families are characterized by inter-octahedral connectivity modes different from the corner-sharing one. Three octahedral connectivity modes have been experimentally observed: corner-sharing, edge-sharing, and face-sharing, as can be seen in Figure 14. In most of the cases, corner-sharing (regular) configuration results to be the lowest energetic one, however, on rare occasions the configurational strain that the cations impose to

the 2D perovskite breaks the standard connectivity pattern and instead stabilizes edge-sharing or face-sharing networks.[33]

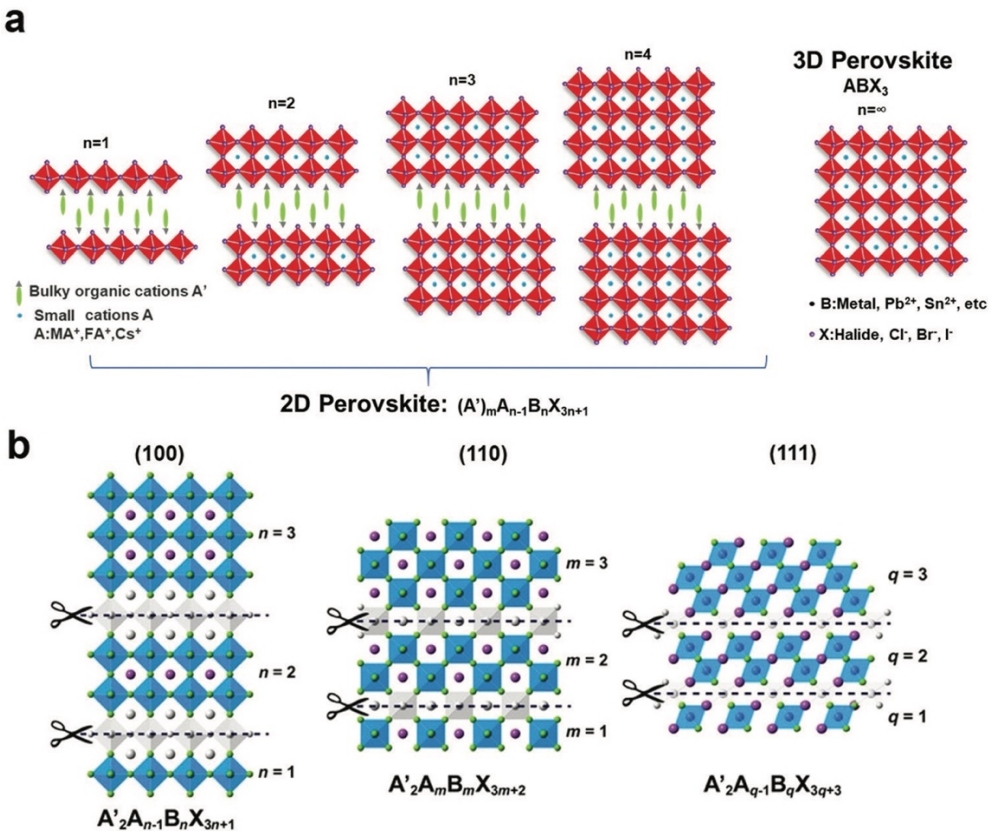

Figure 13. *(a) Schematic comparing 2D, quasi-2D and 3D perovskite structures. (b) Schematic of different oriented families of 2D perovskites.*[6]

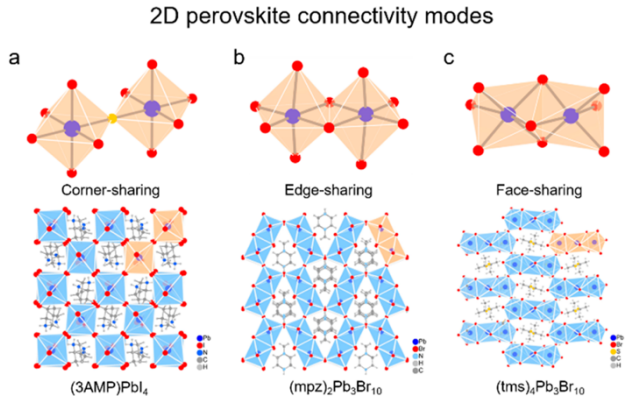

Figure 14. *Connectivity modes in 2D perovskite and their representative examples: (a) corner-sharing, (3AMP)PbI4; (b) edge-sharing, (mpz)2Pb3Br10; and (c) face- sharing, (tms)4Pb3Br10.*[33]

Branching out in a more detailed description of the regular structures of the multilayer ⟨100⟩-oriented, it is possible to distinguish Ruddlesden–Popper (RP) phase, Dion–Jacobson (DJ) phase, and alternating cation in the interlayer space (ACI) phase (Figure 15). RP and DJ classes have general chemical formulae $A'_2A_{n-1}B_nX_{3n+1}$ and $A'A_{n-1}B_nX_{3n+1}$, respectively, from which it is evident they are defined on the charge of the bulky spacer cation. What distinguishes ACI from the RP and DJ perovskites is reflected directly in the formula $A'A_nB_nX_{3n+1}$, as the smaller A-site cation (MA^+, FA^+, or Cs^+) not only resides in the perovskite slab but also fills in the interlayer along with the designated spacing cation A'. Evidently, ACI phase exists only for *quasi*-2D perovskites.[33–35]

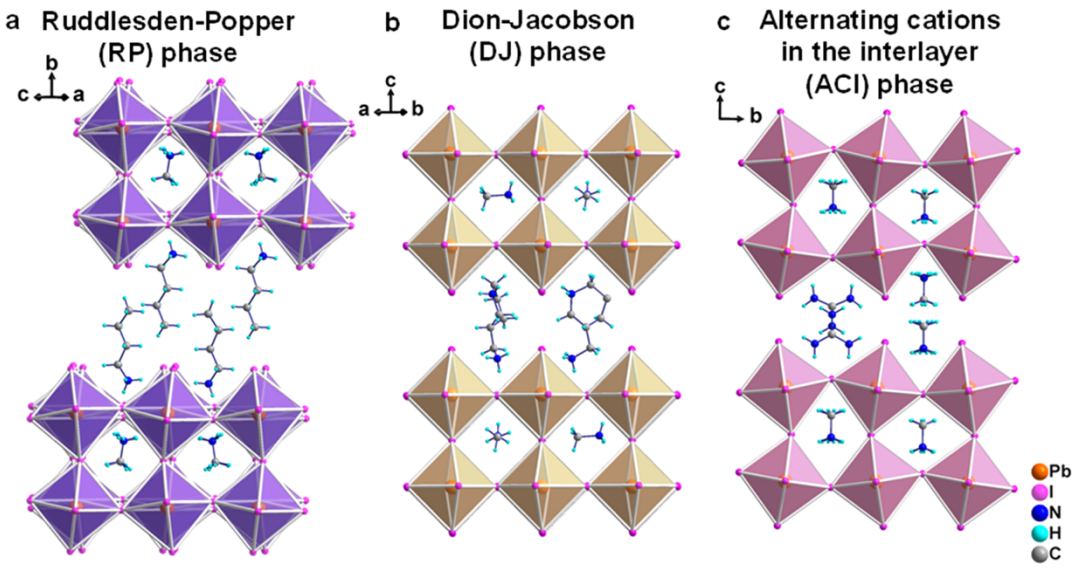

Figure 15. *Structures for ⟨100⟩-oriented 2D perovskites. (a) Ruddlesden–Popper phase with staggered layer stacking. (b) Dion-Jacobson phase with eclipsed layer stacking. (c) Alternating cations in the interlayer phase with staggered layer stacking along the b- and eclipsed along the a- axis.*[31]

For what concerns Ruddlesden–Popper phase in pure 2D perovskites ($n = 1$), repulsion between the two layers of A' divalent cations present between each layer of BX_6 octahedra leads to an offset of one layer of BX_6 octahedra from the next one by one-half of a B-to-B repeat distance in both of the B-X-B directions; this is often referenced to as a (1/2, 1/2) offset (Figure 16b). On the other hand, Dion-Jacobson phase exhibits

perfect stacking with no offset between successive layers (0, 0), or a displacement of (1/2, 0) (*i.e.*, a shift of half a B-to-B repeat distance in one of the two B-X-B directions). This can be attributed to the single layer of ions between each layer of octahedra found in these structures. In addition, it is evident that the organic monocation consists of a charge-bearing headgroup (usually an ammonium group) that interacts with the inorganic layer (electrostatically and/or through hydrogen bonding) and a relatively rigid tail perpendicular to the layer; staggering the layers allows the most efficient packing of the tail groups. On the other hand, a dication in which two head groups are separated by a rigid bridge would be expected to hold adjacent inorganic layers in registry with each other (Figure 16a). However, RP and DJ are ideal configurations, corresponding to very well-defined values of displacement. The organic monocations and dications used in hybrid halide perovskites do not generally have rigid tails or bridges held perpendicular to the layers. In view of their irregular shapes and/or conformational flexibility, and of possible presence of cation–cation and cation–inorganic interactions, most of the real cases can be identified into near-DJ (n-DJ; $x < 1/4$, $y < 1/4$) or near-RP (n-RP; $x > 1/4$, $y > 1/4$), where the offset ranges in a small interval, and some exceptions exist for monocation-DJ (MDJ) and dication-RP (DRP), as schematized in Figure 16c, but it is anyway surprising that so many examples of HOIPs appear to exhibit offsets similar to the ideal expectations with analogous formulae.[32]

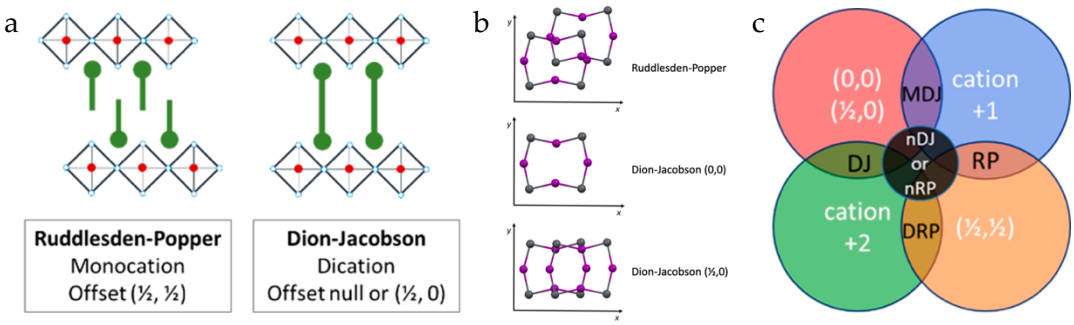

Figure 16. *a) Schematic representation of a Ruddlesden–Popper (RP) and a Dion–Jacobson (DJ) n = 1 layered HOIP. b) Schematic view along z direction of two overlapped inorganic layers with the type of structures corresponding to the ideal offsets. c) Schematic representation of the different possibilities when mixing different offsets and different cations.*[32]

1.2 Properties and Applications

The 2D perovskites exhibit excellent structural diversity, and their properties can be tuned by the inorganic layer thickness, the cage cation and the spacer cation.
In the 2D hybrid halide perovskites, the organic cations act as insulating barriers that confine the charge carriers in two dimensions, but they also serve as dielectric moderators that determine the electrostatic forces exerted on the electron–hole pairs. The specific arrangement of alternating organic–inorganic layers generates an ordered 2D multiple-quantum-well electronic structure that self-assembles in a bottom-up manner. Figure 17 shows how the structures differently contain the organic cation: in 3D the restriction is on the entire cation (Figure 17b), while in 2D (Figure 17b) it is solely on the cross-sectional area of the cation, but not on the length of the organic cation, as highlighted in green. The energy diagram in Figure 17c represents electronic band gap E_g (gray), the optical band gap E_{exc} (blue) of the inorganic framework and the larger HOMO–LUMO gap of the organic cations (green). The organic framework (gray regions) has a dielectric constant ε_2, which is smaller than the dielectric constant ε_1 of the inorganic framework (red regions).
Reducing the dimensionality n, leads the bandgap to increase in defined steps since the structure becomes more quantum confined perpendicular to the stacking direction (Table 1).[30] The feature of bandgap tunability allows for enhanced functional applications in the novel optoelectronic devices including electro-optical modulators, p-n junctions, transistors, photodiodes, and lasers. Evidently, 2D perovskites exhibit wider bandgaps than 3D ones, and the changing trend of bandgaps as a function of the thickness of inorganic layers can be well predicted from first-principle computational studies. A large bandgap of 2D perovskites opens the opportunity for novel applications in power devices, short-wavelength LEDs, and high efficiency tandem solar cells.

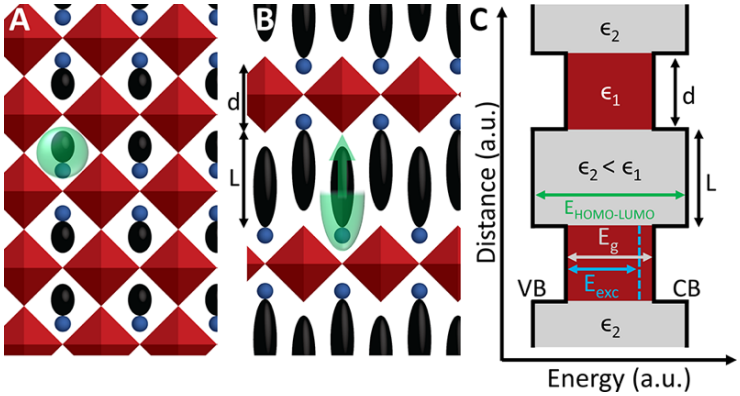

Figure 17. *(a) Schematic of a projection of the 3D hybrid perovskite. (b) Schematic of a projection along the layers of the 2D hybrid perovskite. (c) Energy diagram corresponding to the 2D structure in panel b.*[36]

The cage A-site cation can affect not only the metal-halide-metal (B–X–B) bond angles, like in 3D perovskites, but also the metal-halide (B–X) bond length, both of which can modulate the overlap of the metal and halide orbitals, thus altering the bandgap in a smaller degree than the layer-number. Table 2 summarizes 2D perovskites bandgaps for many different large organic cations. It should be noted that, although the bandgap can be varied via the choice of large organic cation, the bandgaps do not involve the organic orbitals directly. An accurate argument is that the large organic cation can indirectly influence the bandgap via the geometric distortions of the inorganic octahedra, as demonstrated both by DFT calculations and experimental data.[36] Figure 18 shows how the increase in the cross-sectional area of the organic cation affects the orientation of the cations in the organic framework, and for the perovskite to crystallize, how the interoctahedral B-X-B bond angle must change to accommodate the larger cation. Reduction of the X-B-X bond angle from the ideal 180° alters the band structure and increases the band gap of the perovskite.

Additionally, the bandgaps can be tuned through selection of the halide anions: a more electronegative halide anion generally leads to a larger bandgap, and vice versa.

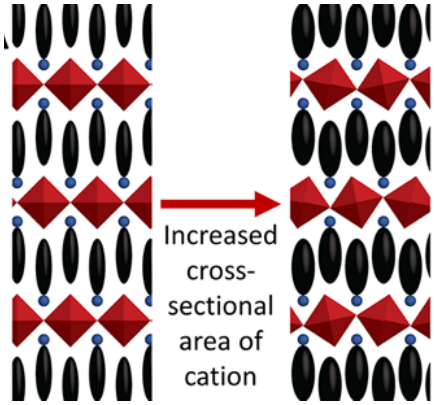

Figure 18. *Effect of increased sectional area of cations on 2D perovskite lattice.*[36]

The properties of 2D perovskites can also be tuned by the spacer cations: they can affect the distortion of each octahedron as well as tilting of the B–X–B bond angles; the exciton binding energy (E_{exc}) of the 2D perovskite (quantum well) structures can be tuned by the dielectric constant of the spacer cation (barrier), since higher dielectric constant of the spacer can lead to less dielectric mismatch between the organic and inorganic layer, thus reducing the E_{exc}; the stability of the materials can be improved as well by introducing hydrophobic cations that can form water-repellent layers and by functionalizing the organic cations with substituents able to form specific intermolecular interactions with the inorganic framework.[30,31,37]

Table 1. *Bandgaps (eV) of several 2D perovskites as a function of dimensionality, n.*[30]

Compound[a]	*n*					
	1	2	3	4	5	∞
Experimental						
$(BA)_2(MA)_{n-1}Pb_nI_{3n+1}$	2.39	2.14	2.02			
$(BA)_2(MA)_{n-1}Pb_nI_{3n+1}$	2.24	1.99	1.85	1.6		1.52
$(BA)_2(MA)_{n-1}Pb_nI_{3n+1}$	2.42	2.15	2.04	1.92	1.85	
$(BA)_2(MA)_{n-1}Pb_nI_{3n+1}$	2.43	2.17	2.03	1.91		1.5
$(BA)_2(MA)_{n-1}Sn_nI_{3n+1}$	1.83	1.64	1.5	1.42	1.37	1.2
$(PEA)_2(MA)_{n-1}Pb_nI_{3n+1}$	2.4	2.2	2			
$(PEA)_2(MA)_{n-1}Pb_nI_{3n+1}$	2.41	2.21	2.18	1.88	1.82	1.68
$(PEA)_2(MA)_2Pb_3I_{10}$			2.1			
$(3AMP)(MA)_{n-1}Pb_nI_{3n+1}$	2.23	2.02	1.92	1.87	1.8	1.59
$(4AMP)(MA)_{n-1}Pb_nI_{3n+1}$	2.38	2.17	1.99	1.89	1.8	1.59
$(GA)(MA)_nPb_nI_{3n+1}$	2.27	1.99	1.73			
DFT						
$(PEA)_2(MA)_{n-1}Pb_nI_{3n+1}$	2.31	2.17	1.95			
$(PEA)_2(MA)_{n-1}Pb_nI_{3n+1}$	1.43	1.2	0.91[a]			
$(BA)_2(MA)_{n-1}Pb_nI_{3n+1}$	1.99		1.78	0.96		
$(BA)_2(MA)_{n-1}Pb_nI_{3n+1}$	2.0		1.7			1.2
$(GA)(MA)_nPb_nI_{3n+1}$	1.12	0.75	0.12			

[a]Denotes the calculations with spin-orbit coupling.

Table 2. *Bandgaps (eV) of several single layer 2D perovskites.*[30]

Compound	Bandgap [eV]	Compound	Bandgap [eV]
Experimental			
$(DA)PbI_4$	2.75	$(CHE)PbCl_4$	3.64
$(HDA)PbI_4$	2.98	$(BZA)_2PbCl_4$	3.65
$(ODA)PbI_4$	2.98	$(PEA)_2PbCl_4$	3.64
$(CA)PbI_4$	3.25	$(PEA)_2PbBr_4$	3.07
$(CHE)PbI_4$	2.87	$(PEA)_2PbI_4$	2.4
$(CA)PbI_4$	3.04	$(PEA)_2PbI_4$	2.49
$(CBA)PbI_4$	2.88	$(MA)_2Pb(SCN)_2I_2$	2.04
$(CPE)PbI_4$	2.86	$(MA)_2Pb(SCN)_2I_2$	1.77
$(DDA)PbI_4$	2.99	$[Ni(OPD)_2(ANC)_2]_n$—$[Pb_4I_{10}]_n$	2.67
$(CM)PbCl_4$	3.7	$(BDA)PbI_4$	2.64
$(PMA)PbCl_4$	3.7	$(PEIM)PbI_3$	2.73
$(TPM)PbCl_4$	3.7	α-$(DMEN)PbBr_4$	3
$(TFM)PbCl_4$	3.77	$(DMAPA)PbBr_4$	2.88
$(MFM)PbCl_4$	3.79	$(DMABA)PbBr_4$	2.85
DFT			
$(MA)_2Pb(SCN)_2I_2$	1.53	$(BZA)_2PbCl_4$	3.34
$(MA)_2Pb(SCN)_2I_2$	2.06	$(BZA)_2PbI_4$	1.42
$(BDA)PbI_4$	2.01	$(BZA)_2SnI_4$	1.33
$(PEIM)PbI_3$	2.91	$(HIA)PbI_4$	1.34
$(EDBE)PbI_4$	2.83	$(HIA)SnI_4$	1.14

The interlayer distance turns out to be also one of the crucial factors that decide the excitonic PL emission from these quantum-well structures. Typically, the RP phases have larger interlayer distance due to the fact that they require a bilayer of spacer organic cations, which inevitably will increase the layer separation from approximately 1.5 times the length of the cation in the case of interdigitation (as in case of benzylammonium) to more than double the cation's length in cases where there is no overlap (like in phenylethylammonium). Thus, in the case of the RP phases the layers are well isolated, showing no inorganic-inorganic interactions, thereby producing an excitonic emission that results directly from the spatial electronic confinement (*n*) of the individual layers. Conversely, the DJ phases, require the organic cations to snugly fit in the perovskite cages created in the interlayer space by the eclipsed stacking conformation of the perovskite layers. The proximity of the layers generates a weak inorganic-inorganic interaction which can be readily observed in the position of the exciton, which shows a pronounced redshift.[33]

As the dimensionality *n* decreases, the exciton binding energy of the layered structure strengthens due to the increase in quantum confinement, leading to the largest E_{exc}, together with the strongest stability, for $n = 1$ ($E_{exc} > 300$ meV), emphasizing the characteristics of Frenkel–Wannier exciton hybridization.[38] High E_{exc} limits photovoltaic efficiency, making 2D perovskites not suitable for solar cell applications, but they enable enhanced photoluminescence (PL) properties for room-temperature light-emitting-diode (LED) applications.[30] Indeed, the organic-inorganic hybrid perovskites offer a high color purity regardless of crystal size because of their multiple quantum well structure. 2D perovskites have been found to emit radiation across the entire visible spectrum upon UV excitation, generating white light. This phenomenon is known as broadband emission, with potential use of layered hybrid perovskites as single-source white-light phosphors. It was demonstrated that PL emission becomes broadened as the degree of distortion of the inorganic layers increases, with the most distorted structure having the broadest emission and longest lifetime.[39–41]

While many works reported the trend of optoelectronic properties by varying *n*, fewer ones focused on fixed n = 1 perovskites finding strategies to tune them. For example, J. Passarelli *et al.* adopted a molecular doping approach to tune the exciton binding energy through incorporation of a TCBQ (tetrachloro-1,2-benzoquinone) dopant into the naphthalene-based organic lattice of a 2D lead iodide perovskite. The naphthalene–TCBQ electron donor–acceptor interactions increased the electrostatic screening of the

exciton, in turn lowering its binding energy relative to the undoped perovskite, thus demonstrating that the strength of electrostatic interactions within semiconductors strongly affects their performance in optoelectronic devices.[38]
Another influencing factor for the band gap is represented by the way individual octahedra are linked among each others, which determines the orbital overlap between the metal and the halide. As a general trend, experimentally determined and theoretically confirmed, the band gap follows the increasing trend "corner-sharing < edge-sharing < face-sharing". This is expected within the special perovskite band structure, since corner sharing provides the strongest bonding between the metal and the halogen (B-X), which in turn gives rise to a "destabilization" of the $5s^2$ lone pair, pushing it to the top of the valence band. As the σ bond weakens through the interactions in the edge-sharing and face-sharing motifs, the lone pair is stabilized, localizing deep within the valence band, while the bottom of the conduction band increases in energy, leading to an opening of the bandgap. The structural diversity obtained in these 2D perovskites could potentially be exploited to further adjust the optical properties of the hybrid perovskites.[42–46]

Among the vast variety of possible organic cation families, aromatic alkyl-ammonium compounds have a number of advantages in terms of design flexibility (Figure 19). On one hand, it is possible to vary the length of the alkylamine tail tethering the mono-/poly-cyclic aromatic group to the inorganic framework. Additionally, the number of fused benzene rings of the acene can be varied (*e.g.*, phenyl-, naphthyl-, and anthryl-) to impact the size and highest occupied molecular orbital–lowest unoccupied molecular orbital (HOMO–LUMO) separation of the organic cation. Finally, substituents or "R" groups (e.g., −H, −F, −Cl, −OH, −CH) can be placed around the acene or alkyl groups to impact the packing or chiral nature of the organic cation or the steric interaction with the inorganic framework (which in turn can impact the detailed structure and therefore the optoelectronic properties of this layer).

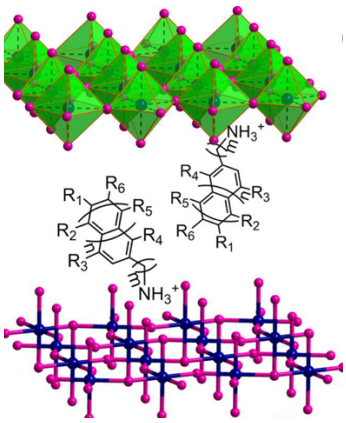

Figure 19. *General acene alkyl-monoammonium cations interacting with the inorganic framework.*[47]

1.3 Aromatic Cations

Aromatic cations were one of the first spacers explored for multilayer 2D perovskites, and they have been widely studied since then. The aromatic rings are believed to be beneficial for charge transport, however, if aromatics such as phenyl groups are involved, they tend to be disordered in the crystal structure frustrating efforts to crystallographically refine the structures. Therefore, the bond lengths and bond angles are usually modeled with restraints and refined to the most stable conformation. Despite the disorder of atoms within each cation, the relative configuration between adjacent spacers can still be determined by refinement since it gives the most stable (lowest energy) structure.

The inclusion of aromatic rings with free and polarizable π-electrons leads to a higher polarizability value than that observed for aliphatic chains, which only have σ-electrons located between their non-polar single covalent bonds (C–C). High polarizability represents a key parameter for improving photovoltaic performance by decreasing the exciton binding energy due to the reduction in the excitons confinement and in the dielectric mismatch between organic and inorganic layers.[48]

The complexity of the aromatic cations provides a tunability of the molecular orbitals of the spacer, which can match with the band structure of the inorganic layer to improve the charge transport. By increasing the conjugation in the cation, the highest

occupied molecular orbitals (HOMO) and lowest unoccupied molecular orbitals (LUMO) of the organic spacers get closer to the valence band maximum (VBM) and conduction band minimum (CBM) of the inorganic layer, which improve the charge transport between them (Figure 20d). In addition, the out-of-plane conductivity increases with the number of the aromatic rings, suggesting better charge transport in the stacking direction (Figure 20e).[49]

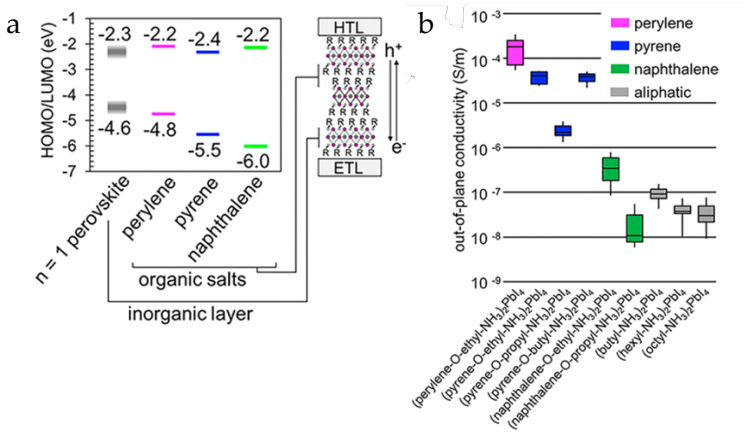

Figure 20. *(a) Energy levels of typical n = 1 perovskites (gray) ($(BA)_2PbI_4$) as compared to the energy levels of the conjugated organic ammonium iodide salts. (b) Out-of-plane electrical conductivity for different n = 1 perovskites.*[31]

The arrangement of aromatic cations in the organic interlayer of 2D perovskites strongly depends on the weak interactions deriving from the presence of delocalized π-electrons clouds. For example, taking the commonly studied $(PEA)_2PbI_4$ (PEA = phenylethylammonium), it incorporates two sheets of organic spacers between the inorganic layers. Within each sheet, the aromatic rings are parallel because of π–π stacking, while between the sheets, the rings adopt a face-to-edge (herringbone) configuration (Figure 21). The penetration depth, defined by the average distance between the N atom of the primary amino group and the plane of terminal halides (Figure 22a), induces different distortions in the inorganic framework (Figure 23), and thus tunable optical properties. It is possible to identify two types of structural distortions: the distortion of the PbX_6 octahedra themselves, quantified through bond length quadratic elongation ($\langle\lambda\rangle$) and bond angle variance (σ^2), and the tilting between

adjacent octahedra, determined from the Pb−X−Pb bond angle, out-of-plane and in-plane distortions, defined as in Figure 22b,c.
The bond length quadratic elongation ⟨λ⟩ can be evaluated as:

$$\langle\lambda\rangle = \frac{1}{6}\sum_{i=1}^{6}\left(\frac{d_i}{d_0}\right)^2 \qquad (3)$$

where d_i are the Pb−X bond lengths, d_0 is the Pb−X bond length for a regular octahedron of the same volume (⟨λ⟩ is dimensionless and independent of the effective size of the octahedron); while bond angle variance σ^2 is calculated as:

$$\sigma^2 = \frac{1}{11}\sum_{i=1}^{12}(\alpha_i - 90)^2 \qquad (4)$$

where α_i are the X−Pb−X bond angles for the octahedra.
The relation between penetrations depth and Pb-X-Pb angle mainly depends on the interactions (*e.g.*, hydrogen bond) between the organic and inorganic layers. When the amino group is way above the plane (negative penetration depth), it has very weak interaction with the halogen atoms, so the octahedra are not tilted (Pb−X−Pb bond angle close to 180°). When the penetration depth is positive, the amino group sinks into the octahedra pocket, and the distances between the N and halogen atoms (both terminal and bridging) decrease. Thus, the interaction between those atoms is stronger and the octahedra have larger tilts (Pb−X−Pb bond angle smaller than 180°). When the penetration depth is around 0.4 Å, the N atom has largest interaction with all the halogen atoms, so the Pb−X−Pb bond angle is smallest. As the penetration depth further increases, the distance increases again (especially for the terminal halogens) and so does the Pb−X−Pb bond angle.
The in-plane Pb−X−Pb bond angle is determined by the projection of the bridging X atoms onto the plane of Pb atoms, while the out-of-plane angle can be defined as the shift of the axial Pb−X bonds away from the normal to the plane of Pb atoms. The in-

plane and out-of-plane distortions contribute to the overall perovskite layer distortion, which in turn has a dominant effect on the exciton absorption and PL for semiconducting 2D HOIPs, as previously mentioned. For example, increased octahedral distortion decreases the bandwidth leading to a larger bandgap, and, at the same time, lowers the energy barrier for some interface defect states leading to a broader PL emission.[31,43,47,50]

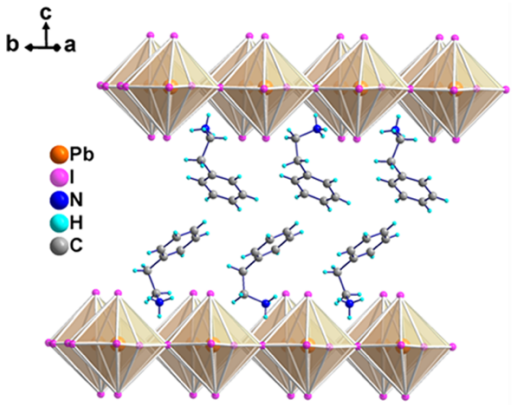

Figure 21. Crystal structure of $(PEA)_2PbI_4$.[31]

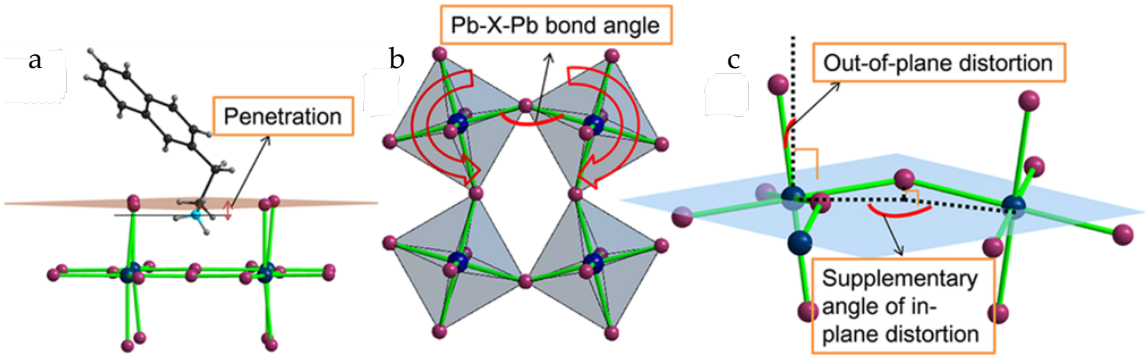

Figure 22. *(a) Definition of organic cation penetration; (b) schematic of perovskite layer distortion; (c) in-/out-of-plane distortion.*[47]

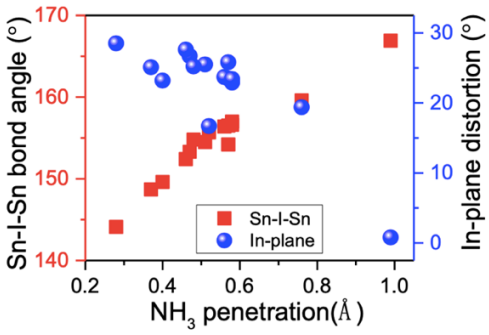

Figure 23. *Sn-I-Sn bond angle and in-plane distortion as a function of the organic cation.*[47]

Penetration depth can be tuned by varying both the number of aromatic rings fused together, thus the conjugation, and the carbon-chain length attached to the aromatic rings of the cation. For example, K. Du *et al*. compared the effects of the cations in Figure 24a to directly have access to these two influencing factors.[47] Furtherly increasing the alkyl chain leads to the reduction in perovskite dimensionality due to the large steric hindrance (3 and 4 in Figure 24b form 1D perovskites), as demonstrated by M. Kamminga *et al.*, with consequent variation in optical properties, always deriving from the increased distortion of the inorganic framework.[43] Shorter alkyl chains provide lower penetration depth, and consequently weaker distortions, but more rigidity due to the decreased flexibility of the lateral substituent.[51]

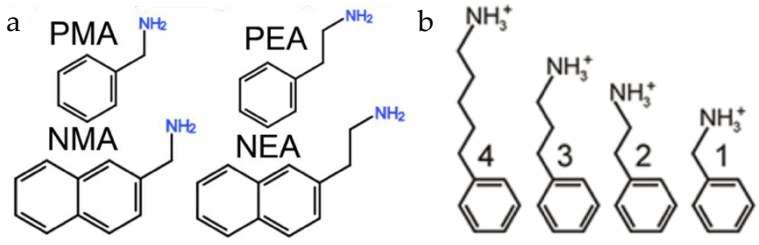

Figure 24. *The molecular structures of the acene alkylamines including (a) PMA = Phenylmethylammonium, PEA = 2-Phenylethylammonium, NMA = 1-(2-Naphthyl)-methanammonium, NEA = 2-(2-Naphthyl)-ethanammonium,*[47] *(b) with increasing alkyl chain.*[43]

1.4 Fluorination of the Aromatic Ring

Fluorine is the most electronegative element in the periodic table and has the similar van der Waal's radii to hydrogen atom. Therefore, the fluorine substitution usually only leads to a minor structural distortion but heavily modify physical and chemical properties. It has effects on surface properties, like inducing hydrophobicity, bulk properties, as piezoelectricity/ferroelectricity and optical properties, or can even be exploited for intermolecular interaction strengthening.

S. Paek *et al.* used 2D perovskites as capping layers for 3D perovskite-based solar cells in order to combine high efficiency and stability. Selecting the right cation was fundamental for improving the passivating role of 2D layer in the device, and fluorinated aromatic rings were demonstrated to lead to a super hydrophobic layered structure with respect to the non-fluorinated/monofluorinated equivalent. In particular, Figure 25a shows the structures of the organic cations. The effect on the contact angle is shown in Figure 25efg, where it is evident how the interactions of external moisture with the device can be suppressed with the presence of perfluorinated aromatic cation. In addition, a strong shift of the intense peak associated to the excitonic 2D feature is visible in the absorption spectrum suggesting a clear variation on the electronic structure induced by the organic substituents (green and pink curves in Figure 25b). From the UV-vis spectra it is also evident how 3D/2D bilayer systems are the best candidate for photovoltaic applications since they preserve high and broad absorption of 3D in the complete visible region, thus high efficiency, but combined with the enhanced stability and protection provided by the 2D perfluorinated perovskite layer.[51]

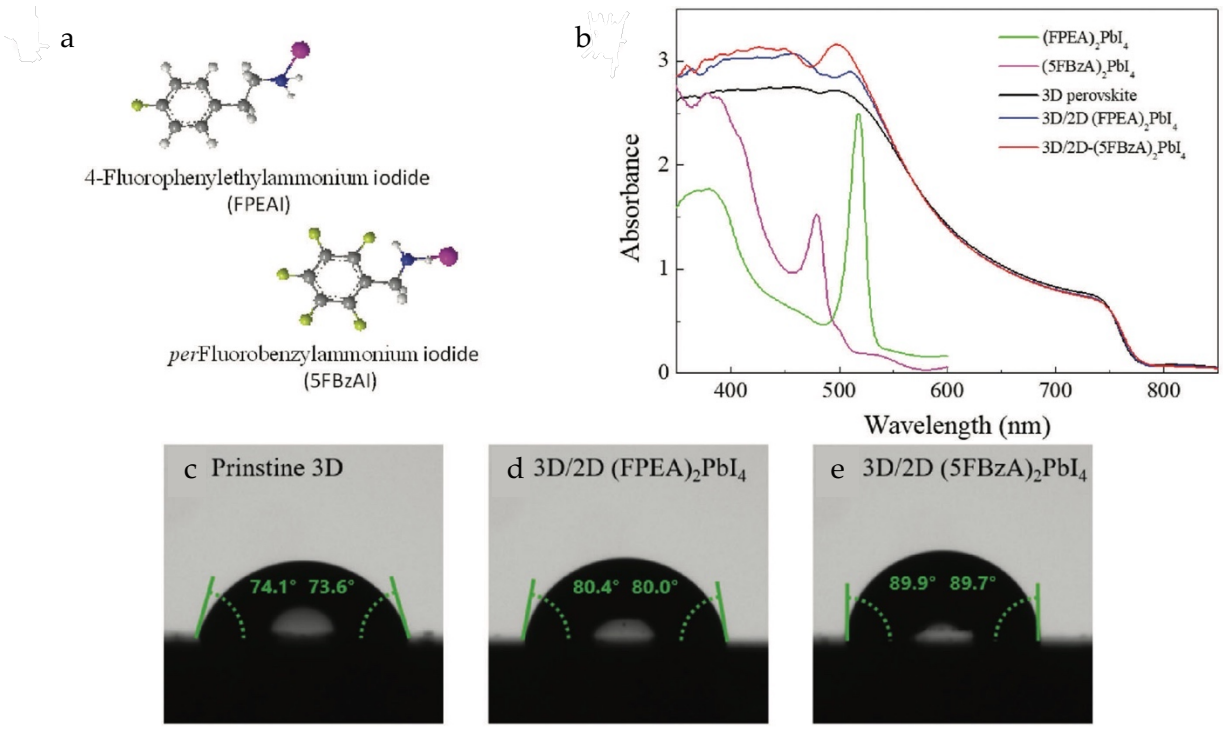

Figure 25. (*a) Schematic of the two ammonium salts, FPEAI and 5FBzAI, employed in the 2D perovskites. (b) UV–vis spectra of the 3D, 2D, and 3D/2D bilayer systems. The contact angle measurements performed on the (c) pristine 3D, (d) 3D/2D (FPEA)₂PbI₄, and (e) 3D/2D (5FBzA)₂PbI₄ surfaces.*[51]

In other cases, crystal structures were investigated, and their deep studies resulted to be fundamental for the understanding of physical properties like phase transition and polarization. For example, P. Shi *et al.* and H. Zhang *et al.* focused on ferroelectricity of these semiconducting layered structures. Ferroelectric materials have been found to be widely used in data storage, capacitors, sensors, energy harvesting, and nonlinear optical devices. Ferroelectrics feature a switchable spontaneous electric polarization and usually also have good piezoelectric performance. Hybrid 2D perovskites, thanks to the well-defined molecular assembly which closely bridges organic and inorganic components, provide combining merits to endow them prominent performances also in piezoelectric and ferroelectric fields. Notably, fluorination strategy was found to strongly affect physical properties, like enhancing Curie temperature and spontaneous polarization. Comparing parent perovskite containing benzylammonium with its

ortho-, *meta*-, *para*- and *per*-fluorinated analogues, different structural symmetries and packing appeared due to the larger steric hindrance between adjacent cations, together with enhanced phase transition temperature and changed polarization. In particular, *ortho* substitution and *per*fluorination showed large piezoelectric response and excellent ferroelectricity, while the centrosymmetric structures of *meta*- and *para*-substituted cations resulted in no polarization, demonstrating that the advantages brought by H/F substitution (especially monofluorinated substitution) seem to be only effective and universal for alkane-based cations, while the effects on rigid rings of aromatic-based cations are limited and not ideal, due to the influence of selective space position for H/F substitution.[52,46]

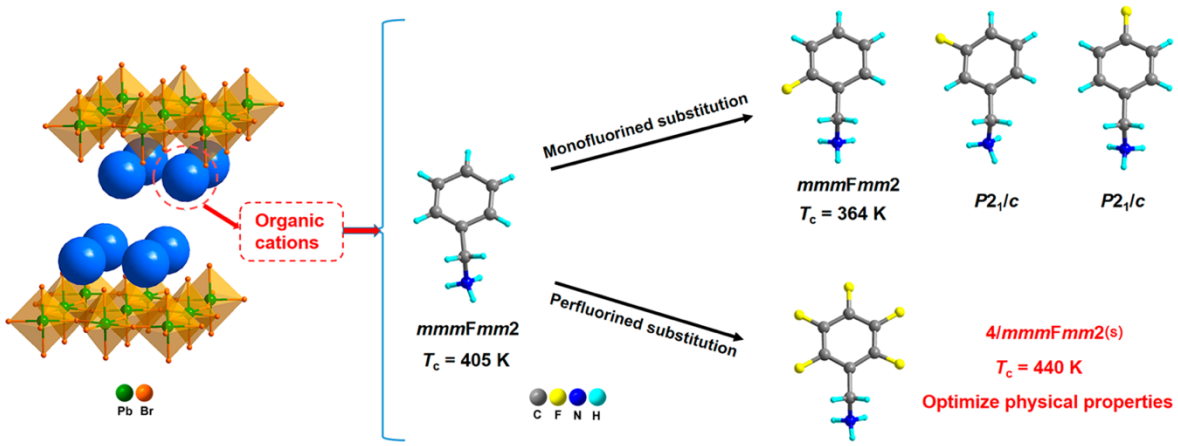

Figure 26. *Design of 2D perovskite highlighting the different molecular structures of fluorinated cations, with structural symmetries and Curie temperatures (T_c).*[52]

The fluorination of organic cations in 2D perovskite SCs opens up also the possibility of strengthening supplementary interactions established with the inorganic framework. Before providing a deeper explanation of this effect, it is appropriate to first introduce interaction engineering and halogen bond.

2. Interaction Engineering in Perovskite-Based Devices

Intermolecular interactions have been extensively employed to ameliorate device performances, by introducing polymers or small molecules both as specific additives or functionalized cations in perovskite lattice. Interesting strategies focused onto the strengthening of intergranular[53] and interalyered[54] interactions through the addition of macromolecules. Y. Du *et al.* utilized polyamidoamine (PAMAM) dendrimers as the dendritic crystallization framework templating the $MAPbI_3$-crystallizing process and demonstrated that the modification of intergranular perovskite/perovskite interface plays a critical role for power conversion efficiency (PCE) and stability of perovskite solar cells (PSCs). With the dendritic polymer backbone crosslinking the perovskite grains, the perovskite intergranular interactions are significantly strengthened (Figure 27). K. Yao *et al.* applied a similar idea by incorporating polyethylenimine (PEI) cations (Figure 28), which in this case led to the formation of a multilayered 2D perovskite structure.

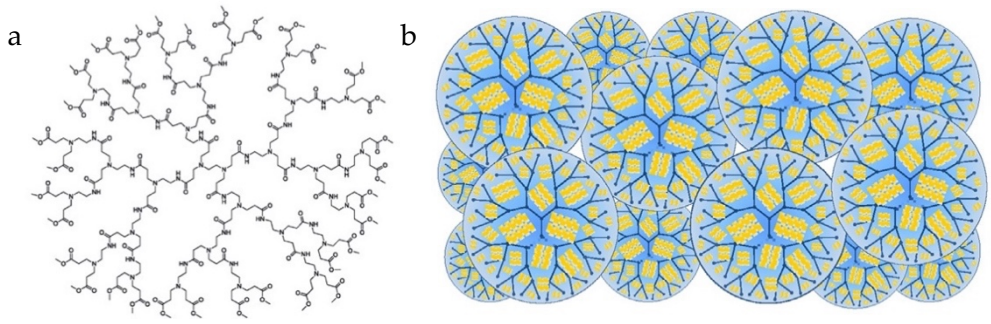

Figure 27. *(a) Diagrammatic skeleton of PAMAM dendrimers bearing the methyl esters at the molecular periphery, whose amino and carbonyl groups can potentially interact with the perovskite grains surface. (b) Representation of the interaction of perovskite grains with PAMAM cations acting as a good crystallization framework.*[53]

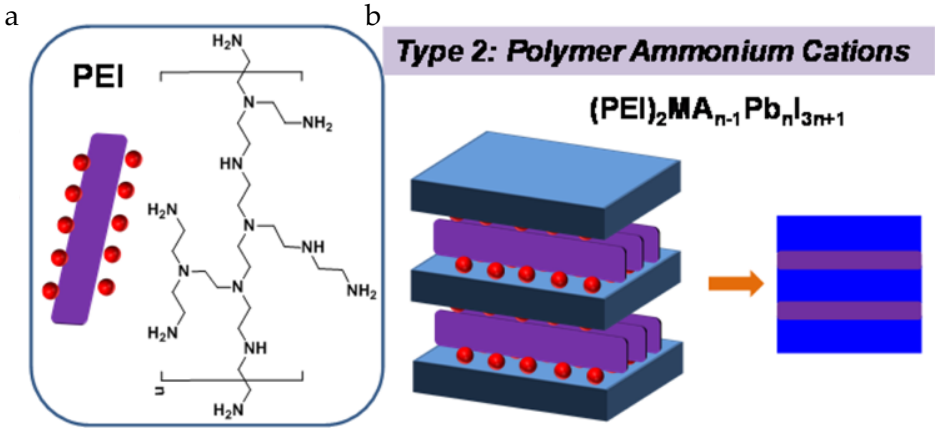

Figure 28. *(a) Diagrammatic skeleton of PEI being a potential multi-ammonium cation. (b) Representation of the interaction of perovskite grains with PEI cations leading to a multilayered structure.*[54]

The common feature of the two polymers is the extended ramification, which is the key for possible multiple interactions with the perovskite basic crystal. In the case of the dendritic polymer, the branching is isotropically extended in the space. Thanks to its three-dimensional spherical configuration, it affords the slight conformation

adjustment in the process of interacting with the perovskite grain boundaries, differently from linear polymers, that struggle to adjust their curly conformation in order to interact with grain boundaries. At the same time, the local aggregation, typical of linear macromolecules that could play a detrimental role for the crystallinity of the material, is effectively avoided (Figure 29). Thus, the internal space of the dendrimers might act as an excellent dendritic crystallization framework. PEI is not a dendrimer, but it has a branched structure too, indeed, the beneficial effects of the incorporation of PAMAM or PEI on the stability and morphology of perovskite layer are the same.

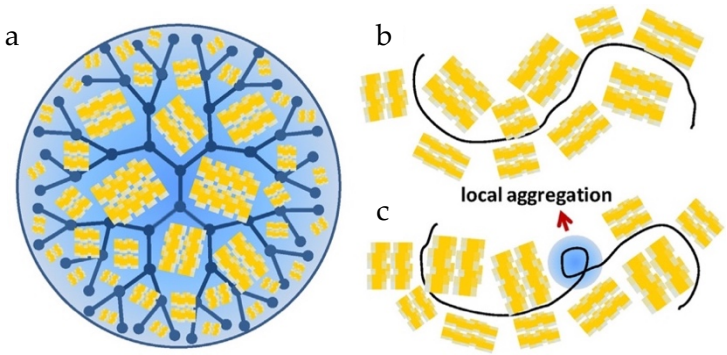

Figure 29. *Schematic mechanism illustrated by the macromolecular steric conformation regulating the perovskite phase morphology: (a) dendritic polymer; (b) linear polymer being completely extended with macromolecular curly conformation; (c) linear polymer with local aggregation in its individual macromolecular chain.*[53]

As shown in Figure 30, by increasing the amount of PAMAM in the precursor solution, a more compact and uniform perovskite morphology is obtained. Notably, the strengthened intergranular interactions could remarkably suppress the perovskite grain boundaries and remove the pinholes in the perovskite film. The excess amount of PAMAM dendrimers induces the separation of PbI_2 as shown in Figure 30f. Similarly, the presence of PEI into perovskite solution leads to the growth of compact, pore-free films with small grain size. The same results of morphology film

improvement with higher grain continuity and less prominent grain boundaries are obtained by enhancing the amount of PEI (Figure 31).

Macromolecular cations can provide stronger steric hindrance, endowing perovskite crystals with considerably improved moisture stability, thanks to the several functionalities that can passivate undercoordinated species, hindering their interaction with water molecules. Moreover, the incorporation of PAMAM or PEI can form more compact perovskite films, further minimizing water intake of the devices.

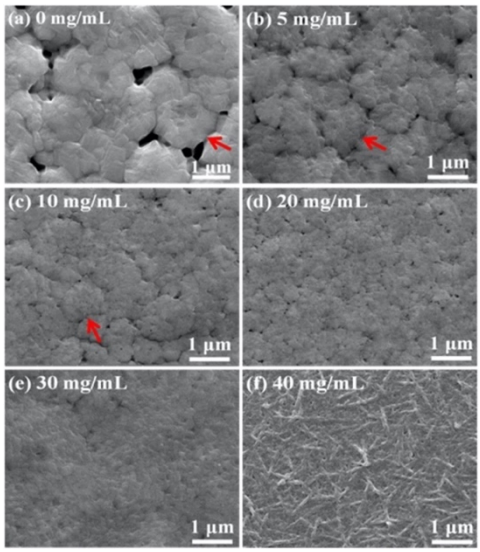

Figure 30. *SEM images of PAMAM-modified perovskite films with different amounts of PAMAM dendrimers.*[53]

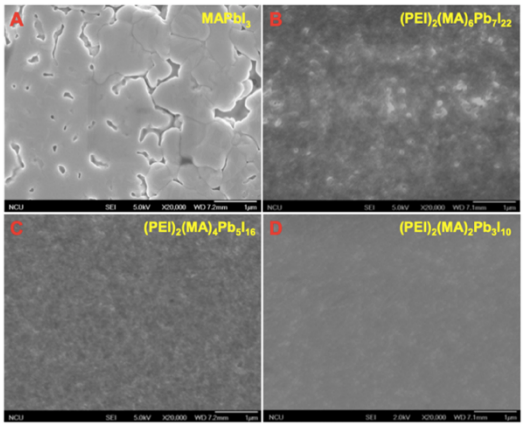

Figure 31. *Top surface SEM images of* $MAPbI_3$ *and* $(PEI)_2(MA)_{n-1}Pb_nI_{3n+1}$ *films.*[54]

Polymers are interesting tools because of the multiplicity of interactions they can introduce in the lattice. The specificity of the interaction can also be investigated by analyzing how the organic cations can interact with the inorganic sublattice or among each others and exploited also through the introduction of additional small molecules. Some other examples from literature will be presented focusing now on the different kind of interaction.

2.4.1 Hydrogen Bond (HB)

Hydrogen bonding (HB) is an important intermolecular interaction, which involves a polar donor group $D^{\delta-}$–$H^{\delta+}$ and an electronegative atom $A^{\delta-}$ as the acceptor of the hydrogen bond (Figure 32), denoted as ''D–H···A''. D and A are very electronegative atoms such as N, O, F, although in some cases even S, Cl, P and C can be involved in weaker HB. HB is well known to play a critical role in structural stabilization.

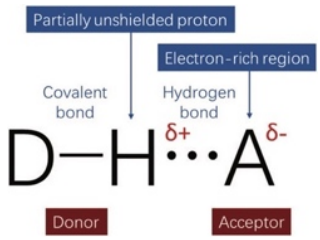

Figure 32. *General representation of HB.*[5]

Hydrogen bonds are found in most basic hybrid halide 3D perovskites since the simplest and most common organic cations are MA (CH_3NH_3), MP (CH_3PH_3) and FA ($HC(NH_2)_2$). S. Ozorio *et al.* analyzed the effects of HB on the relative energy stability of $ASnI_3$ polymorphs (A = MA, MP, FA; Figure 33). Since the structural cohesion of $ASnI_3$ depends on the attractive forces between the A-cations and the inorganic framework, the weak HBs also contribute to the structural stability. In particular, the planar FA-cation has four HB donors from $–(NH_2)_2$ to stabilize the inorganic frame, while MA and MP have only three ($–NH_3$ and $–PH_3$). Hence, the structural cohesion

tends to be higher for $FASnI_3$ than for the $MASnI_3$ structures, which are both more cohesive than $MPSnI_3$. Despite the geometric similarity between MA- and MP-cations, the hydrogen of $–PH_3$ forms a weaker H···I bond, leading to weaker structural cohesion for $MPSnI_3$. Indeed, by considering the absolute cohesive energy per hydrogen donor the MA > MP sequence is found. Due to their weaker structural cohesion, the $MPSnI_3$ structures can be more affected by a moisture and oxygen-rich environment than $MASnI_3$ and $FASnI_3$.[2]

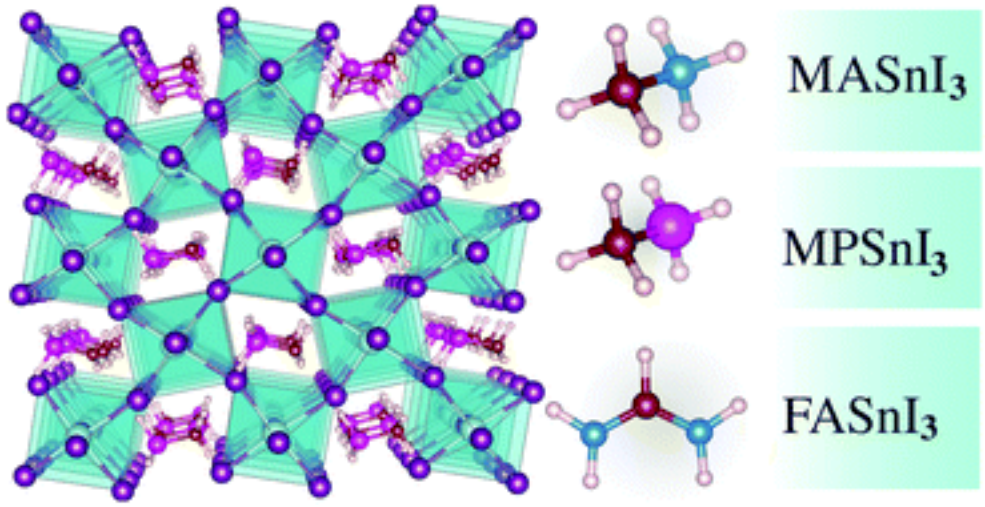

Figure 33. *MA, MP and FA as the most common organic cations forming 3D perovskite structures.*[2]

Similarly, diammonium cations can form hydrogen bonds with the inorganic framework, but the cation size can influence the strength of the interaction. As demonstration of this fact, E. R. Dohner *et al.* studied the crystallography of lead bromide perovskite with two similar organic diammonium cations, N^1-methylethane-1,2-diammonium (N-MEDA) and N^1-methylpropane-1,3-diammonium (N-MPDA). Interestingly, they assemble into (110) and (001) perovskites respectively, due to their different lengths (Figure 34). Due to the corrugated nature of the (110) sheets, the primary ammonium group of N-MEDA can form hydrogen bonds (Figure 35) with halides from two adjacent inorganic sheets, likely stabilizing the (110) structure. In contrast, the longer N-MPDA cations can adequately separate (001) inorganic sheets,

avoiding close contact between adjacent layers and hindering hydrogen bonds formation.[55]

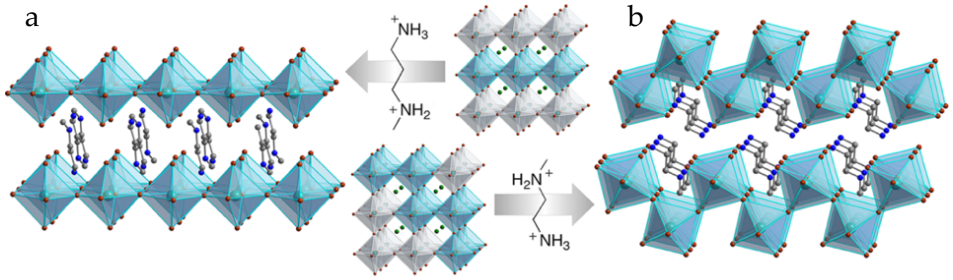

Figure 34. *Structures of (A) the (001) perovskite (N-MPDA)PbBr4 and (B) the (110) perovskite (N-MEDA)PbBr4.*[55]

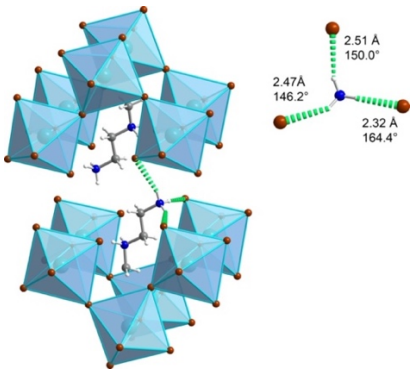

Figure 35. *Hydrogen bonds (green) between the primary ammonium group of N-MEDA and the inorganic layers in (N- MEDA)PbBr4. Inset: H–Br distances and N–H–Br angles for the atoms involved in the hydrogen bonds.*[55]

Further hydrogen bonds have been found into the perovskite lattice through the introduction of surface passivators. For example, Guo *et al.* demonstrated that the phenylalkylammonium groups can stabilize the perovskite lattice through suppression of iodide ion migration. Very interestingly, the stabilization effect is

enhanced by increasing the chain length due to the stronger bonding of the passivating molecule to the perovskite surface and the increased steric hindrance for diffusion of iodide (I^-) on the perovskite surface. In order to understand how the steric and Coulomb interactions of the molecules affect the passivation results, four molecular cations with the same end groups but different alkyl chain lengths were investigated, namely phenylmethylammonium iodide (PMAI, n = 1), phenethylammonium iodide (PEAI, n = 2), PPAI (n = 3), and phenylbutanammonium iodide (PBAI, n = 4), as shown in Figure 36a. About the specific adsorption geometry, the iodide anion adsorbs on top of Pb, while the NH_3 group of the molecular cations points to the corner Pb atom and forms HBs with the surface iodide ions (Figure 36b). The alkyl chain extends along the direction normal to the perovskite surface with the benzene ring pointing out of plane. By calculating the binding energy of the passivation molecules on the perovskite surface, it was possible to conclude that the main difference in the binding strength comes from the HBs between the NH_3 group and I^- ions. With increasing n, the bond order of H···I bonds increases (with the rest being almost constant), which geometrically is demonstrated by shorter H···I bond length.[56]

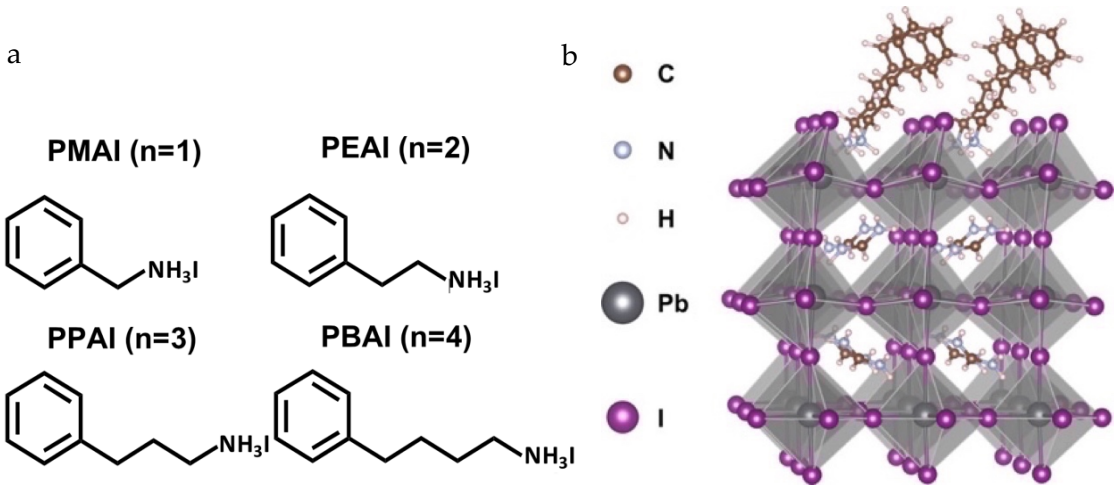

Figure 36. (a) Schematic structure of the passivating molecules. (b) Schematic diagram of a molecular passivated perovskite surface. [56]

2.4.2 Covalent Bond (CB)

A covalent bond, involving the sharing of electron pairs between the atoms, is always affected by the electronegativity of the corresponding atoms, and it refers to the polarity of the bond. A bond formed by mutual attractions holds the resultant atoms together. The stronger the mutual attraction, the larger is the bond energy. In general, the bond energy of a CB is larger than that of a HB. Therefore, the CB may play a more significant role in the device stability.

Proppe *et al.* succeeded in exploiting this strong interaction for improvement of cell parameters and better stability in air. The cross-linkable 4-vinylbenzylammonium (VBA) ligand was selected to build high efficiency 2D/3D solar cells. They used VBA to form well-ordered $n = 1$ and $n = 2$ low dimensional perovskites atop a 3D active layer in a 2D/3D heterostructure, whereafter exposure of the top layer to UV photoexcitation activates the vinyl groups of VBA to form new covalent bonds among the 2D layers (Figure 37).[57]

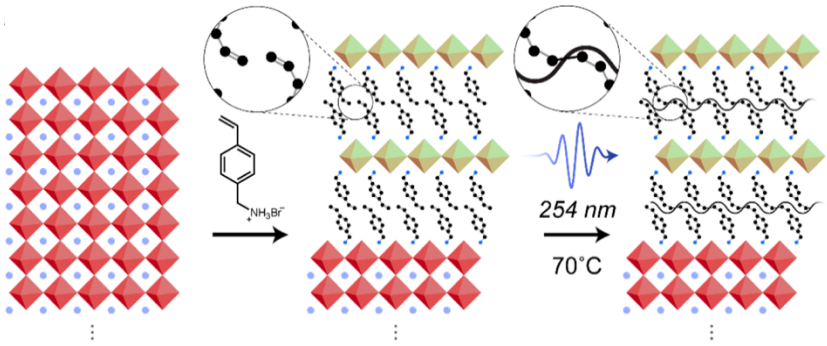

Figure 37. *Schematic illustrating the process by which formation of cross-linked 2D perovskites atop a 3D majority layer is achieved using the ligand VBABr.*[57]

L. Zhang *et al.* used polyvinyl pyrrolidone (PVP) for passivation of both Cs and Pb undercoordinated surface defects of $CsPbI_2Br$ perovskite. Both O-Cs and O-Pb were potential covalent bonds that can lead to a reduction of surface traps due to the positive

charge of these defects which could be coordinated with a lone electrons pair of acylamino in PVP. However, from density charge calculations only O-Pb revealed to be a strong covalently-like bonding, while the low distributions of electrons between Cs and O suggested the presence of a weaker ionic interaction. In compensation, the passivation of Pb species by PVP led also to the improvement of crystallinity, resulting in the reduction of internal defects inside the grain. The covalent bond in this case can be classified in a more specific way as a dative bond, which other examples are provided about as follows.[58]

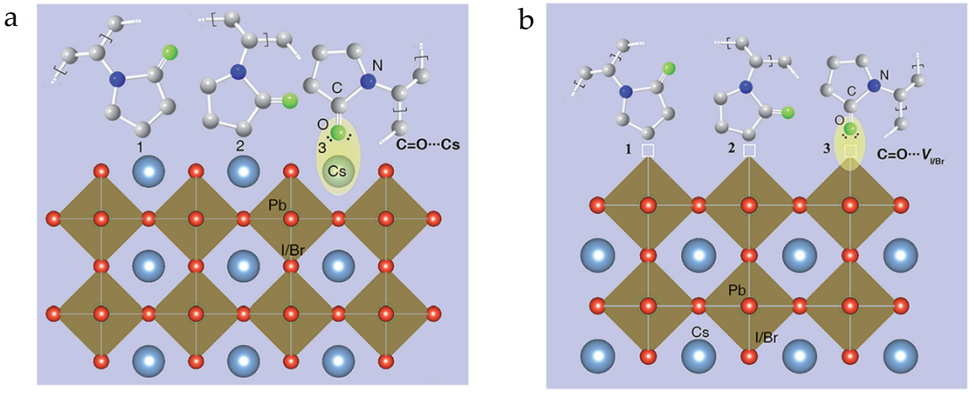

Figure 38. *Three proposed PVP passivation configurations of (a) excess Cs ions and (b) undercoordinated Pb ions.*[58]

2.4.3 Dative Bond (DB)

Passivation have also been realized by exploiting Lewis bases or Lewis acids, depending on the perovskite surface charges that wanted to be neutralized.
Undercoordinated Pb^{2+} having incomplete octets in the outer orbitals are Lewis acids as they tend to accept electrons to satisfy the octet rule. These undercoordinated Pb^{2+} defects, therefore, can be passivated by Lewis bases that donate lone pairs of electrons. Noel *et al.* proposed a strategy consisting of using the Lewis bases of thiophene (S donor) and pyridine (N donor) to neutralize the net positive charges residing on Pb

atoms caused by the loss of I^-. Figure 39a shows how the loss of iodine at the surface of the perovskite leads to vacancy sites and to a resulting net positive charge residing on the Pb atom. Consequently, photogenerated electrons could fall into this Coulomb trap site, thus neutralizing the charge and rendering the crystal more stable. In Figure 39b thiophene or pyridine molecules are proposed as donors of electron density to Pb species, forming a coordinate or dative covalent bond and effectively neutralizing the excess positive charge in the crystal. They demonstrated that treatment of lead chloride perovskite films with thiophene and pyridine can result in a significant decrease in the rate of nonradiative recombination in perovskite films.[59]

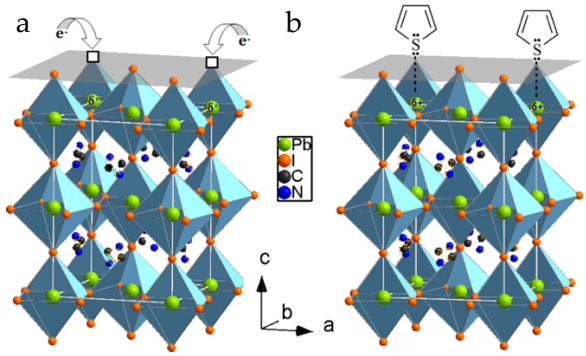

Figure 39. (a) Possible nature of trap sites and (b) proposed passivation mechanism.[59]

L. Liu *et al.* provided a thorough understanding of the mechanism by which Lewis base passivation reduces charge losses (Figure 40). They understood that pyridine and thiophene achieve similar effects but through different mechanisms. Thiophene acts by removing electron density from the surface. In contrast, pyridine attracts electrons into an unoccupied orbital that appears near the bottom of the perovskite conduction band (CB) and that is localized around the strong coordinative bond formed by the pyridine nitrogen and surface lead atoms. It is essential that no trap states are created, and the electron can easily escape into the CB. The coordinate (dative) bonding between the N atom of pyridine and an under-coordinated Pb atom of the Cl-doped $MAPbI_3$ (001) surface is quite strong. In contrast, the interaction of the S atom of thiophene with the Pb atom of the surface is weaker. The calculated binding energies

are −0.892 and −0.541 eV for pyridine and thiophene, respectively. In combination with the larger electronegativity of N relative to S, the difference in the bonding strength is responsible for the different effects pyridine and thiophene have on the CB edge of the perovskite surface.[60]

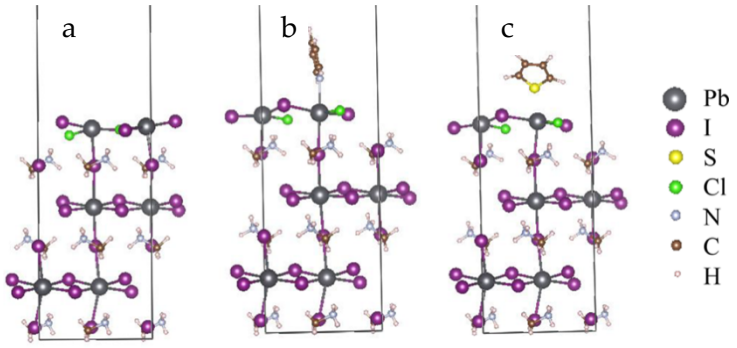

Figure 40. Simulation cells showing optimized geometries of (a) the Cl-doped $MAPbI_3$ (001) surface and the same surface with adsorbed (b) pyridine and (c) thiophene molecules.[60]

Polymers containing thiophene and pyridine and other Lewis bases, such as O donors, are particularly attractive for passivation of undercoordinated Pb^{2+} defects, owing to their rich structural modularity and relatively flexible adaptable configuration.[61–64] One example among the various employed macromolecules is IR-P (Figure 41), including a large number of S, N, and O atoms, which provides Lewis basic sites beneficial for defect passivation in the perovskite films. Long-chain polymers can not only serve to passivate GBs, but also to improve morphology, crystallinity, or grain sizes of the perovskite films. Other advantages are that hydrophobic segments in the polymers can protect perovskite films from degradation by moisture, and inter-grain cross-linking can be stabilized by immobilization of long chain polymers in perovskite films, as previously seen for other polymers.[61]

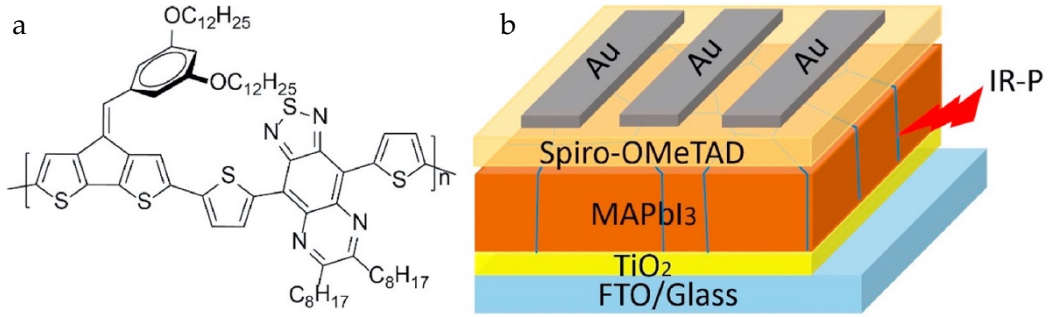

Figure 41. (a) The molecular structure of IR-P. (b) Device configuration of PSCs with IR-P.[61]

2,3,5,6-Tetrafluoro-7,7,8,8-tetracyanoquinodimethane (F4TCNQ) possessing strong electron-accepting ability has been used as a Lewis acid to passivate negative trap states (undercoordinated I^-, I^- interstitials, Pb vacancies and PbI^{3+} antisites) via coordination. The trap states at the perovskite surface are efficiently suppressed, leading to a homogenous surface potential of perovskite, which avoids the surface carrier recombination.[65] Fullerene has also been proposed as passivator. Indeed, Xu *et al.* demonstrated that PCBM can both bind iodide-rich defect sites on grain boundaries and bind up excess iodide from the solution, leading to significantly reduced hysteresis and recombination loss (Figure 42).[66]

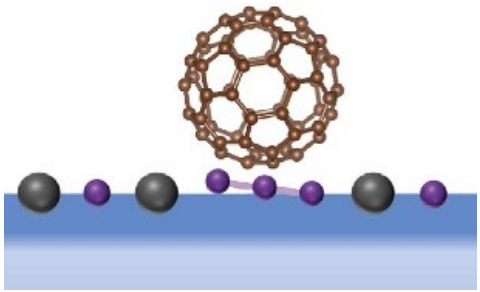

Figure 42. A schematic of halide-induced deep trap passivation: PCBM adsorbs on Pb-I antisite defective grain boundary during perovskite self-assembly. Grey = Pb, violet = I.[66]

2.4.4 π-π Stacking

π-π stacking refers to attractive, noncovalent interactions between aromatic rings, since they contain π bonds. Although π-π interactions are usually weak, the system characteristics may be considerably affected by a large number of these simultaneous contacts. This type of interactions can establish among perovskite surface modulators, enhancing the interfacial charge transfer properties, or among organic aromatic cations in low dimensional perovskites, providing higher structural stability.

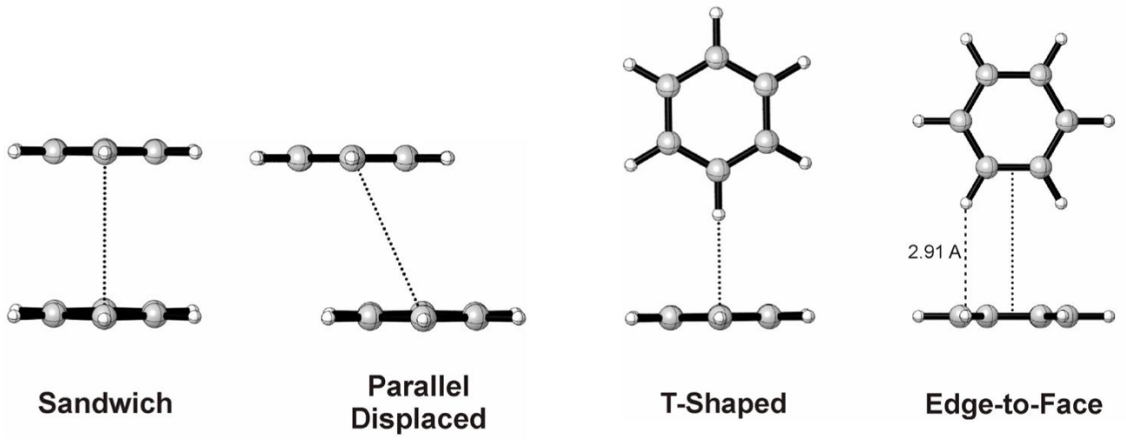

Figure 43. *Four representative conformations of the benzene dimer.*[67]

Y. Lin et *al.* introduced a π-conjugated Lewis base (IDIC in Figure 44) for passivation of Lewis acid traps on perovskite surface. In comparison with PCBM, the additional interactions between aromatic rings present in IDIC promote electron extraction and electron transport, providing smaller V_{oc} loss and consequently higher efficiency.[68]

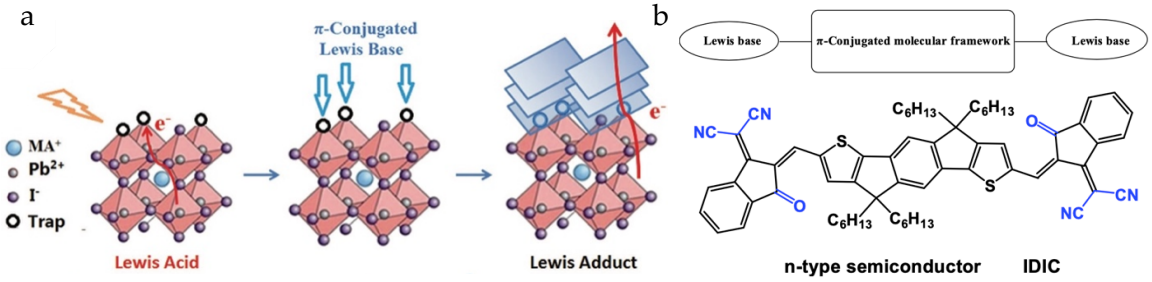

Figure 44. *(a) Schematic of the interaction of the π-conjugated Lewis base and Pb; (b) The molecular structure of IDIC.*[68]

J. Hu *et al.* demonstrated how to tune the chemical structure of the organic cations to simultaneously improve the device performance and stability of 2D perovskite solar cells. They found out that introducing a perfluorinated phenethylammonium, F5-PEA, into the PEA-based 2D perovskite layer can improve the efficiency of such solar cells with significantly meliorated stability, thanks not only to the modifications in the crystal structure but also to the improvement in film texture.[69]

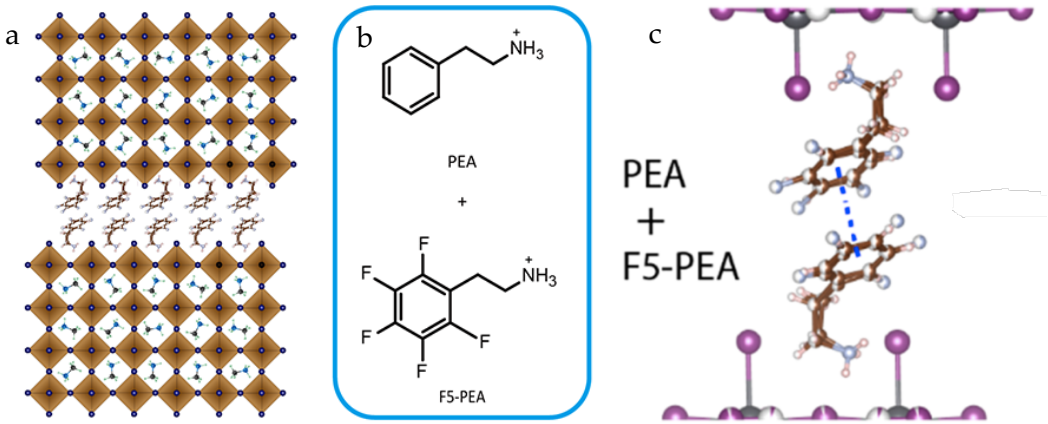

Figure 45. *2D hybrid perovskites and characterization of their photovoltaic devices: (a) crystal sketch of PEA/F5-PEA quasi-2D hybrid perovskites (n = 4); (b) molecular structures of PEA and F5-PEA; (c) π-π stacking in evidence.*[69]

Aryl···aryl interactions can change, for example, by tuning the *para*-substituent of phenylethylammonium cation (PEA). An increasing cation-cation interaction occurs with Y halogen enlargement in the $(Y\text{-}PEA)_2PbI_4$ derivatives (Y = H, F, Cl, Br): the distance from centroid of one aryl to the plane of its neighbor increases, but, as shown, the overlap increases.[70] (Figure 46)

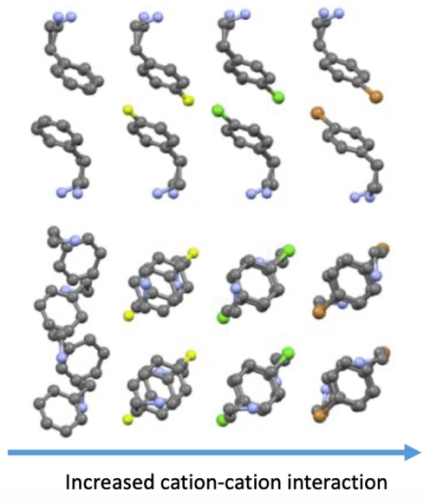

Figure 46. *Representation of cation-cation interactions in $(Y\text{-}PEA)_2PbI_4$, with Y = H, F, Cl and Br from left to right, showing an increasing distance between the ring planes, but also a stronger overlapping.*[32]

3. Halogen Bond (XB)

Halogen bond (XB) is a recently discovered powerful tool which can play a fundamental role in the design of advanced functional materials. After the crystallographic studies on the $Br_2\cdots O(CH_2CH_2)_2O$ adduct reported by O. Hassel in 1954[71], it has quickly become one of the most interesting interactions adopted for the construction[72,73] and functionalization[74,75] of supramolecular structures, thanks to its unique properties that provide a wide range of applications in numerous fields.[76] As schematically represented is Figure 47, the interaction R-X···Y establishes between an electrophilic region X of a molecular entity - where X represents a halogen atom, considered as site of high electron density because of its high electronegativity – and a nucleophilic region Y in another, or the same, molecular entity. R-X represents the XB donor and Y the XB acceptor. The interaction strength increases by increasing the electron density on Y (anions are better XB acceptors than neutral species) and decreasing the electron density on X, therefore the presence of electron-withdrawing substituents about X contribute to create stronger interactions.

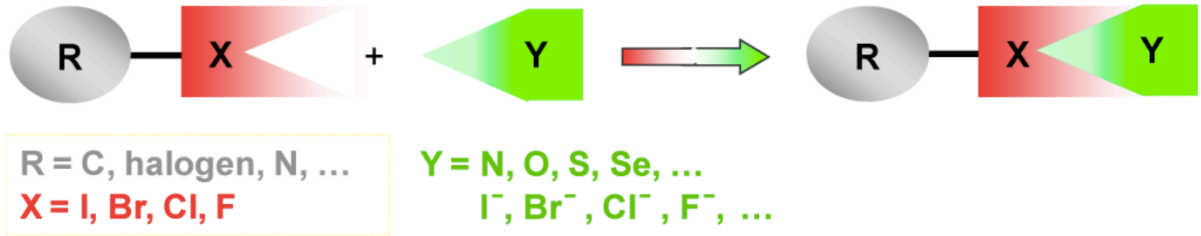

Figure 47. *Schematic representation of halogen bond.* [76]

Halogen bond can be assimilated to well-known hydrogen bond (HB), but what make XB such special interaction are its differences and not its similarities with HB.

3.1 Directionality of XB

First of all, XB is a highly directional interaction. It can be explained by introducing the concept of σ-hole. The σ-hole is a region of depleted electron density which localizes on the elongation of the covalent bond(s) the halogen atom is involved in. The electron density around X results to be anisotropic in covalently bound halogen atoms, with a length reduction along R-X bond axis with respect to its perpendicular direction (Figure 48). Thus, the nucleophile Y tends interact with the halogen atom σ-hole which is narrowly constrained along R-X axis, providing the high directionality of the interaction, with a consequent R-X···Y angle approaching linearity (180°).

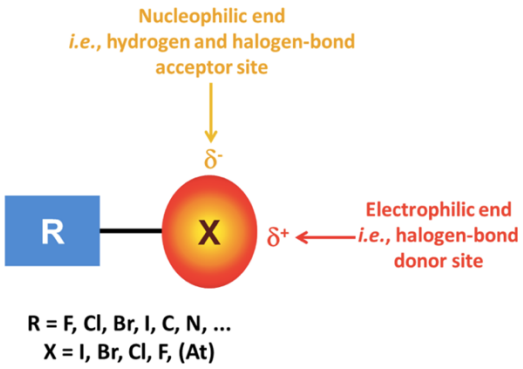

Figure 48. *Schematic representation of the anisotropic distribution of X electron density and its effective radius.*[76]

When heteroatom Y possessing n-pairs are involved in XB, the interaction can undergo a mild deviation from linearity, lying preferentially along the axis of the donated n-pair on Y.

3.2 Tunability of XB

Another important property of XB is the easy modulation of its strength through halogen atom tunability. In particular, the XB strength scales with the polarizability of the XB donor atom, that is, F < Cl < Br < I. Indeed, F is the least prone to be involved in XB, being the less polarizable halogen atom, and can act as an XB donor only when attached to particularly strong electron-withdrawing groups. Cl, Br and I are able to form halogen bonds with increasing strength.[76]

The nature of R group covalently bound to halogen atom can also influence the strength of the bond, since it is involved in the formation of the σ-hole. For example, the combination of fluorine atoms in proximity of the halogen contributes to generate a stronger XB donor, since high electronegative F atoms are able to withdraw electrons from the ring creating a more positive σ-hole along C-X axis. In Figure 49, the different distribution of electron density on aromatic XB donors are represented, highlighting the effects of tuning the halogen atom (vertical) and of fluorinating the benzene (horizontal).[76]

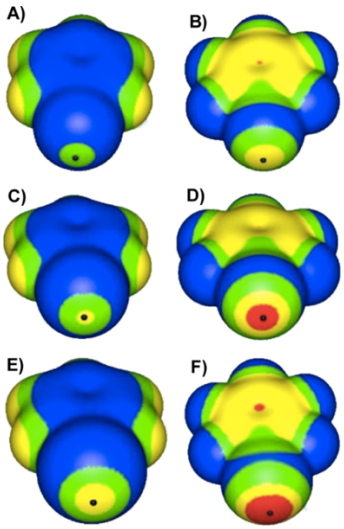

Figure 49. *Representation of electrostatic potential calculated with DFT on (a) chlorobenzene, (b) pentafluorochlorobenzene, (c) bromobenzene, (d) pentafluorobromobenzene, (e) iodobenzene, and (f) pentafluoroiodobenzene. Color range (kcal/mol): red, greater than 20; yellow, between 20 and 10; green, between 10 and 0; blue, negative.*[76]

3.3 Hydrophobicity of XB

Halogen atoms are typically considered as hydrophobic residues. Indeed, a typical XB donor site (*e.g.*, I or Br atom) is remarkably less hydrophilic than a typical HB donor site (*e.g.*, an OH or an NH group).[76] In addition, the frequent presence of fluorinated segments in the XB-donor, which, as already mentioned, boosts interaction strength, increases the hydrophobicity of the final supramolecular adducts, giving protection against humidity and improving material stability.[77]

This peculiarity, together with directionality and tunable strength, makes XB a particularly attractive tool for photovoltaic materials, like perovskites, which need to be isolated and protected from environmental factors and improved in internal stability. First, an overview of how interactions are in general used for implementation of material and device properties will be presented. Then, a focus on halogen bond in this field will introduce the experimental work.

3.4 Halogen Bond for Device Improvement

Now that all the necessary tools have been introduced, some of the most exemplifying cases will show how the unique features of halogen bond can be advantageous for perovskite-based photovoltaic devices.

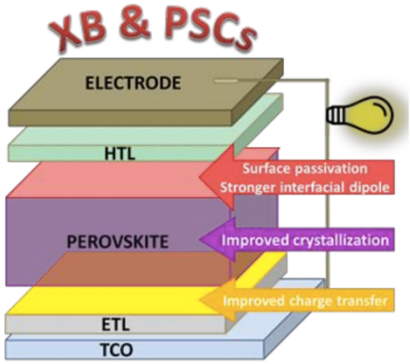

Figure 50. *Schematic of perovskite solar cell highlighting the improvements introduced by halogen bond.*[77]

3.4.1 XB-Donors for Perovskite Passivation

As mentioned in the introduction, uncoordinated/undercoordinated species in perovskite lattice are detrimental both for the stability of the material and for the efficiency of the device. In the configuration of a perovskite-sensitized solar cell, where MA-based perovskite acts as capping layer for Al_2O_3 mesoporous insulating scaffold, perovskite lattice is particularly rich of undercoordinated species because of the irregular geometry of its substrate. For the particular case of $CH_3NH_3PbX_3$ crystals, both undercoordinated metal cations and undercoordinated organic cations at the crystal surface would be unstable to oxygen and water and bind with water molecules when exposed to air, causing hydration of the crystal surface. Conversely, halide anions in crystalline materials are relatively stable to air exposure. Therefore, it is more likely that an excess of undercoordinated X^- ions is present at the crystal surface. Thus, A. Abate *et al.* exploited one of the strongest halogen bond donors, iodo-pentafluorobenzene (IPFB), for the passivation (Figure 51b) of exposed halogen anions.[78] In Figure 51a the nature of the interaction between IPFB (XB donor) and I^- from lead iodide octahedron (XB acceptor) is represented: the high electronegativity of fluorine atoms on the aromatic ring leads to the formation of a strong σ-hole along C-I axis and to the anisotropic distribution of charges, favoring the interaction with any electron-rich sites, especially with halogen anions.

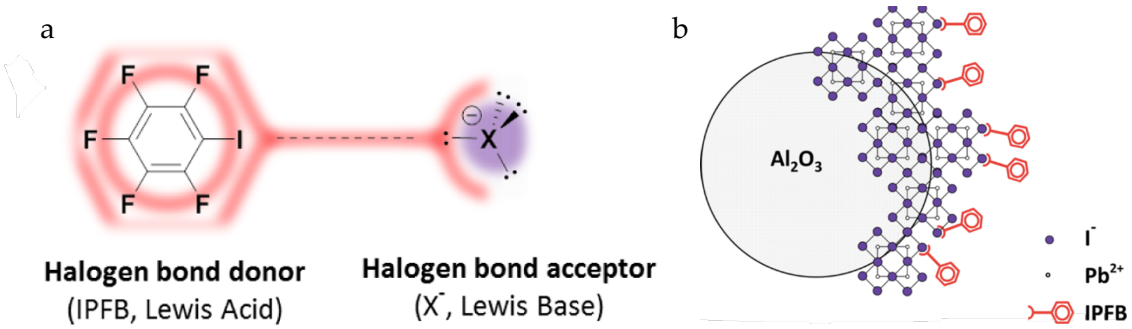

Figure 51. *(a) Schematic view of the halogen bond interaction between IPFB and a generic halogen anion with sp^3-hybridized valence electrons. (b) IPFB molecules as passivators of perovskite undercoordinated species.*[78]

Self-assembly of IPFB on 3D perovskite irregular surface has beneficial effects on the efficiency of the device with an increase of PCE of about 2% with respect to non-treated material. The passivation of undercoordinated halide anions favors charge extraction under working conditions suppressing potential hole traps, especially located at the perovskite/HTL heterojunction.[78]

3.4.2 XB-Donors as Crystallization Modulators

Hole traps passivation has an important role for the improvement of device performance. A. Ruiz-Preciado *et al.* realized that adding a bifunctional halogen bond donor to perovskite layer, instead of a monofunctional one (as IPFB), would have introduced an additional mechanism of undercoordinated species passivation. 1,2,4,5-tetrafluoro-3,6-diiodobenzene (TFDIB) has the potentiality to form two different halogen bonds at the same time. Thus, if introduced in the perovskite lattice, it can not only passivate surface halide species (asymmetric mode), but also crosslinking two inorganic octahedra in the bulk perovskite (symmetric mode), acting as crystallization modulator. The two proposed mechanisms are represented in Figure 52b. The presence of unreacted TFDIB, demonstrated by solid-state NMR, strongly indicates that it does not form stoichiometric compounds with the perovskite but rather binds to the limited number of exposed sites. In addition, DFT calculations (Figure 52a) suggests that the XB modulator in the bulk is more likely to connect two octahedra instead of occupying an A-site of the lattice, due to the strong σ-hole which favors the highly directional interaction with X^- species. Passivation of undercoordinated halide species of $FAPbI_3$ both at the surface and along bulk defects, typically at the grain boundaries or vacancies, through the introduction of TFDIB in the precursor solution, causes, as expected, superior performances of the perovskite solar cell.

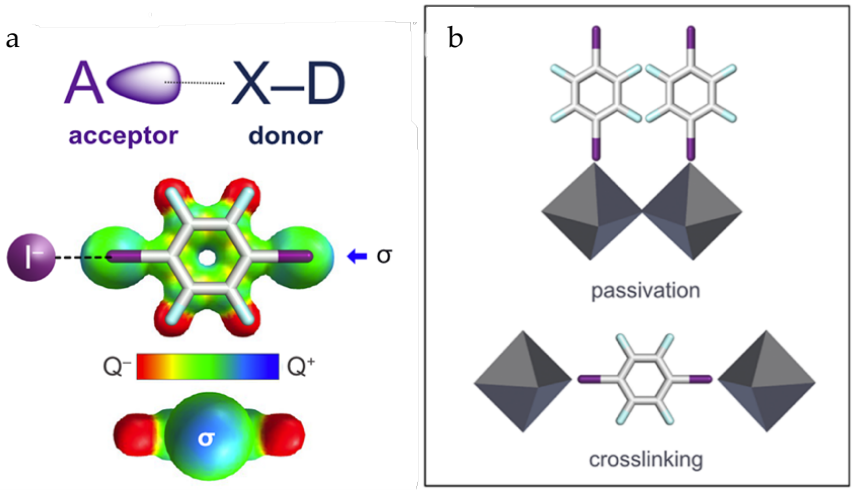

Figure 52. *(a) Schematic representation of XB between an XB acceptor (A) and donor (X). Structure and optimized geometry (DFT calculations) of TFDIB, with the corresponding top and side views of the electrostatic potential surface highlighting the σ-hole. (b) Envisaged modes of interaction of TFDIB with the hybrid perovskite: surface passivation and crosslinking of the perovskite grains.*[79]

Another example of bifunctional XB donor as crystallization modulator is 1,4-diiodooctafluorobutane ($C_4F_8I_2$).[80] SEM images show that the introduction of this additive modifies the perovskite crystallization leading to improved morphology. Halogen bonding interactions formed between the modulators and undercoordinated species provides strong connections for a more compact and pin-hole free morphology (Figure 53b), both with respect to pristine material and modulated material with non-fluorinated additive, which form weaker halogen bonds (Figure 53a). The higher density of grains in perovskite film has not only positive effects on charge transport with lower energy losses in the photovoltaic device, but also a higher environmental stability benefitting from a minimized diffusion of water and/or oxygen molecules, favored by the hydrophobicity provided by fluorinated species.

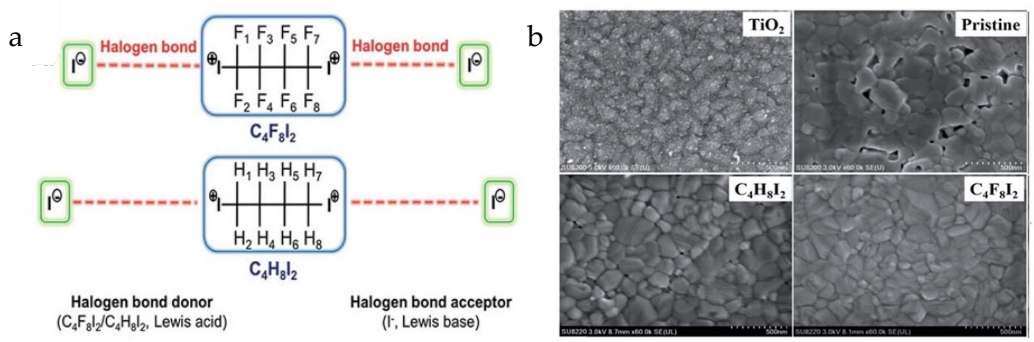

Figure 53. *(a) Schematic representation of $C_4F_8I_2$ and $C_4H_8I_2$, highlighting the different strength of interaction with iodide anions in the two cases. (b) Top-view SEM images of neat TiO_2 and various $CH_3NH_3PbI_3$ films after thermal annealing. All images share the same scale bar (200 nm).*[80]

3.4.3 XB-Donors as Perovskite/ETL Interface Modulators

A similar strategy was applied by M. Wolff *et al.* on a perovskite solar cell with the architecture shown in Figure 54.[81] Perfluorinated aliphatic carbon chains terminated with an iodine- or bromine-anchoring group (X-PFC_n) are absorbed at the perovskite surface by a simple solution process. The regularity of the perovskite active layer leads the XB donors to form an ordered self-assembled monolayer (SAM) at the perovskite/fullerene-based ETL interface. Figure 54b represents the charge distribution at the anchoring point through density functional theory (DFT) simulation, predicting the halogen bonding interaction. The binding of organohalides to a perovskite surface decreases the density of surface traps, as seen for the precious examples. Yet, in this case, surface traps passivation is ruled out as main reason for device performance increase, since PL, tr-PL electroluminescence, and SPV measurements demonstrated that functionalization has no effects on recombination properties. Instead, the main proposed mechanism for the explanation of V_{OC} enhancement is the improvement of charge separation and suppression of nonradiative recombination at the perovskite/C_{60} interface, since the effect due to the SAM is only seen if C_{60} is also present.

Different effects appear by tuning both the halogen anchoring group and the perfluorinated chain length.

As revealed by FT-IR spectra, Br-terminated perfluorocarbons assemble in a higher molecular order than I-terminated ones, probably due to the smaller strength of XB formed by Br with respect to I, rendering Br-terminated molecules more mobile. The strong halogen bond between I and perovskite surface halide species leads to a distortion in the SAM arrangement both with respect to deposited Br-PFC$_n$ and pristine I-PFC$_n$. Thickness and density of the layer are consequently altered, as demonstrated also by contact angle measurements.

Perfluorocarbons length has opposing effects since increasing the length of perfluorinated chains leads to higher hydrophobicity of the perovskite layer (Figure 55), which is beneficial for the device stability and contrast the tendency of interaction with environmental factors. Unfortunately, enhancing the chain length, not only promotes environment isolation, but also favors the electrical insulation of the perovskite layer, hindering charge transport and a good device performance.

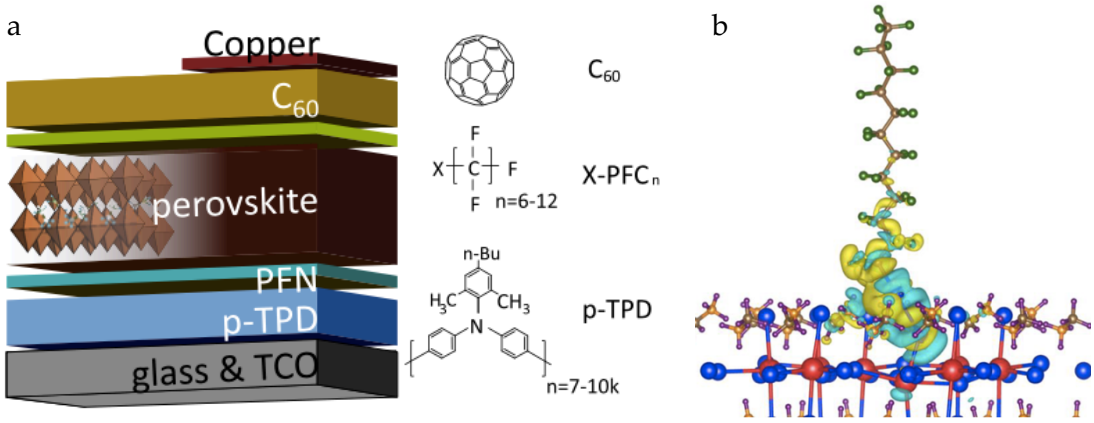

Figure 54. *(a) Schematics of the p–i–n-type device architecture showing the position of the individual layers, as well as the chemical structure of the molecules used for the SAM preparation and the transport layers. (b) DFT simulations of the coupling between an I-PFC$_{12}$ molecule and a perovskite (I-terminated) surface together with the positive (yellow) and negative (turquoise) charge redistribution responsible for the halogen-type bonding.*[81]

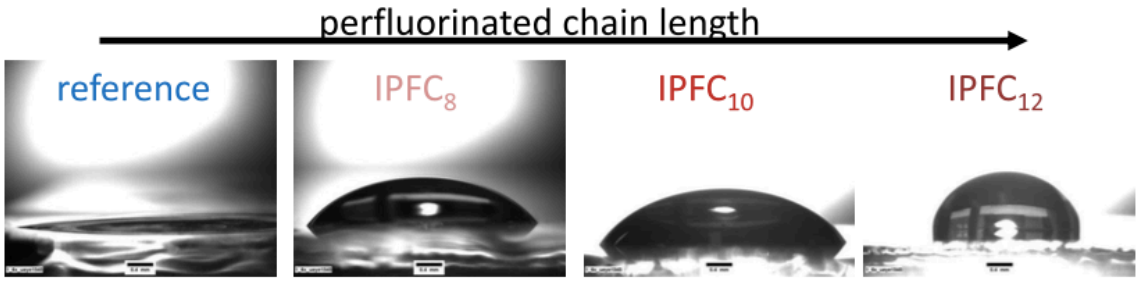

Figure 55. *Contact angle measurements of 2-propanol on perovskite|SAM samples with different lengths.*[81]

In order to increase the stability at perovskite/ETL interface but also to improve charge transport properties, L. Zhang *et al.* employed a bifunctional modifier which could strongly interact with both layers.[82]

The interface formed by ETL and the halide perovskite layer governs the interfacial charge injection properties and the overall device stability. The tri-layer system shown in Figure 56 has been demonstrated to improve the efficiency of the device with respect to a simple bilayer system, because the organic interlayer helps in avoiding the lattice mismatch and weak coordination that can establish between perovskite layer and TiO_2 substrate. The interfacial organic modifier consists in a bromoacetate molecule which has carboxylic group on one side and Br atom on the other side as terminal groups. Therefore, it is able to simultaneously anchor on TiO_2 substrate via covalent bonds and on perovskite material via halogen bond.

In addition, the variation of halogen bond strength gives access to the tunability of device performance and properties: it has been demonstrated by tuning the halogen atom in the XB-donor. As expected, iodoacetate can provide the shortest halogen bond (3.696 Å), while chloroacetate gives the longest one (3.956 Å), with bromoacetate providing an intermediate halogen bond length value of 3.861 Å. The effects of the molecular engineering approach from bromoacetate to iodoacetate and chloroacetate are revealed in the spatial distributions of the molecular orbitals, electron density difference plots, energy gap values, adsorption energies and Hirshfeld charge changes.

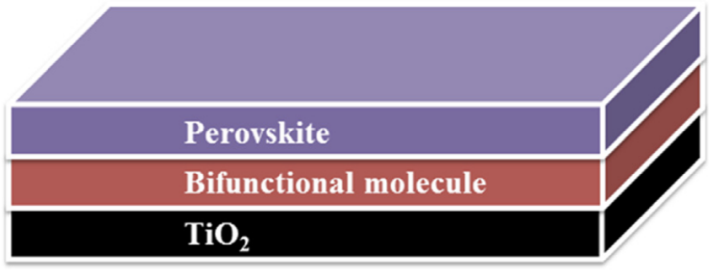

Figure 56. *The employment of a bifunctional molecule between TiO2 and the halide perovskite layer to enhance the perovskite solar cell performance.*[82]

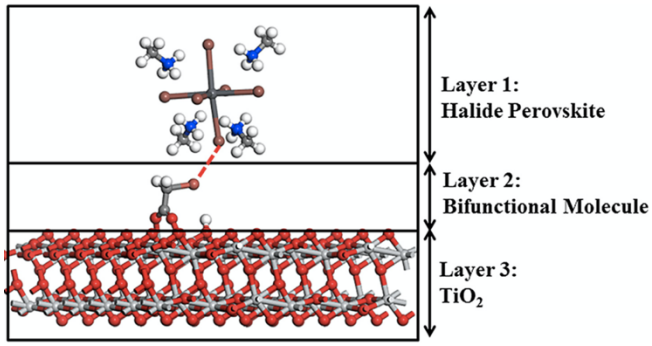

Figure 57. *Structure of the perovskite/bromoacetate/TiO2 tri-layer, highlighting halogen bond between bromoacetate and perovskite.*[82]

3.4.4 XB-Donors as Templating Cations

The alternative use of XB-donors as templating cations in perovskite material has also been investigated. This approach opens up to low-dimensional perovskites world, leading the researchers to move their focus from the device architecture to the organic cation design. M. Tremblay *et al.*, starting from RP-2D perovskite obtained with benzylammonium,[83] used para-substituted derivatives of benzylammonium to study the modification in crystallographic structure and optical properties of the layered material.[32] In particular, halogenated cations – Y-phenylmethylammonium (Y-PMA, Y

= F, Cl ,Br, I) - were chosen in order to be able to form tunable halogen bond with the inorganic sublattice of 2D perovskite. As shown in Figure 58, the atom in Y position has the possibility to interact with the undercoordinated halide species of lead iodide octahedrons. The interaction strength is theoretically expected to change in the order F << Cl < Br < I because of the decreasing electronegativity of halogen atom, and this trend has been verified also by the crystallographic data. The comparison between Y···I^- interatomic distance and sum of Van der Waals radii, together with C-Y···I^- bond angle measurements, confirm the establishment of halogen bonding only for bromine- and iodine-substituted cations.

Following these considerations, stability of (Br-PMA)$_2$PbI$_4$ and (I-PMA)$_2$PbI$_4$ has been verified, as expected, to be higher under ambient conditions (ca. 50% humidity, ca. 20 °C) in darkness. For what concerns the inorganic sheets offset, despite the evidence for halogen bonding in some of these structures, (Br-PMA)$_2$PbI$_4$ and (I-PMA)$_2$PbI$_4$ exhibit very different structures, notably exhibiting nDJ and nRP offsets, respectively (Figure 59). In contrast, (Cl-PMA)$_2$PbI$_4$ and (Br-PMA)$_2$PbI$_4$ adopt similar packing and nDJ translations, despite their different halogen-bonding strengths. Thus, although halogen bonding allows the Y-PMA monocations to act as interlayer bridges, potentially affecting the stacking of the inorganic layers, the conformational flexibility of the cations, combined with the other cation−cation interactions present, steric hindrance, and the various distortions of the lead iodide octahedra, underlines that halogen bonding is not the only factor. Optical properties are relatively little affected in this series, with the main influencing factor being represented by PbI$_4$ octahedra distortions.

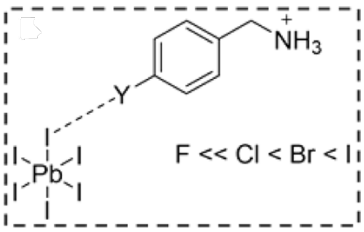

Figure 58. *Schematic representation of the halogen bonding between the iodine of the inorganic sheet and the cation.*[32]

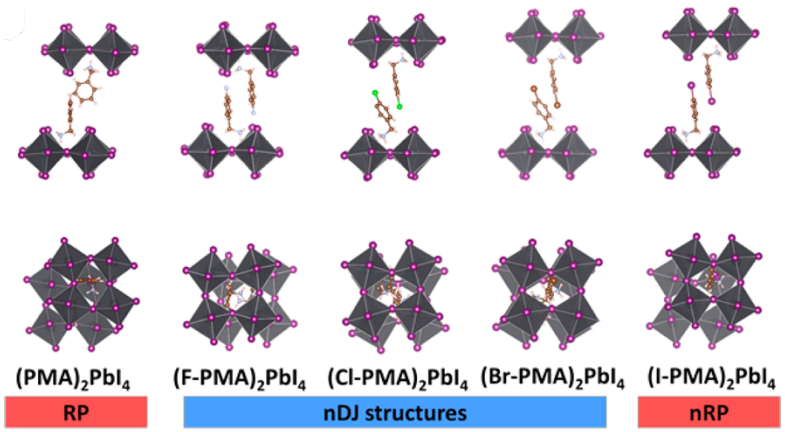

Figure 59. *Crystal structures of (Y-PMA)$_2$PbI$_4$: (top) side view parallel to the inorganic layers (along the short axis) and (bottom) view along an axis perpendicular to the inorganic planes.*[32]

X. Fu et *al.* exploited the same strategy of introducing XB interactions in 2D perovskite lattice through the design of stronger XB donors as templating cations, and they were able to apply the material for the improvement of photovoltaic device performance.[27] As previously mentioned in the Introduction, 2D perovskites are not suitable for constituting the entire active layer in a solar cell, because, besides the higher stability, 3D perovskites have anyway better charge transport properties. However, the combination of the two structures can optimize the device performance, keeping the advantages of both 2D and 3D ones. Typically, 2D perovskite thin layers are used to passivate the 3D perovskite surface, thus forming an interlayer between 3D perovskite layer and HTL in order to suppress potential holes traps at their interface. Alternatively, X. Fu et *al.* created a mixed 2D/3D perovskite where 2D domains are specifically located at 3D grain boundaries (GBs) thanks to a controlled crystallization. The well-designed XB donors, possessing a strong σ-hole thanks to the fluorination of the aromatic ring, not only act as templating cations for the 2D perovskite but also as strong bridges between 2D and 3D domains, suppressing ion migration at the phase interface by increasing the corresponding activation energy, thus avoiding the problem of phase segregation.

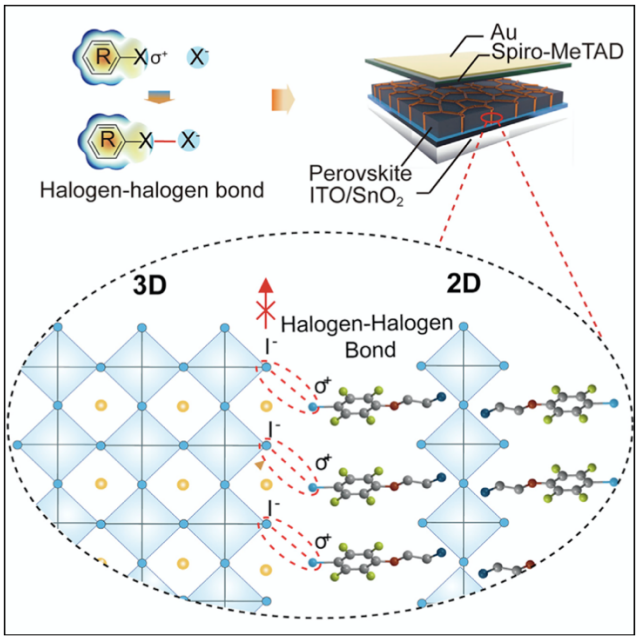

Figure 60. *Solar cell architecture with focus on XB donors from 2D perovskite suppressing ion migration at 3D perovskite GBs.*[27]

4. Results and Discussion

Several XB-donor cations with tunable XB-donor ability have been selected taking into account that the main feature enabling the formation of XB is the presence of the σ-hole. The magnitude of the σ-hole defines the XB interaction strength and intensifies increasing the polarizability of the halogen and/or introducing electron-withdrawing substituents in the molecular scaffold. Based on this, 4-iodoanilinium (IA^+) and (4-X-2,3,5,6-tetrafluoroaniline)-ethan-1-ammonium (X-FEA^+, X = Cl, Br and I) have been applied. The first is expected to be the weakest XB-donor, while X-FEA^+, due to ring fluorination, are stronger XB-donor. We also prepared, as a model compound, a perovskite containing benzylammonium (BA^+, Figure 61), to assure its reproducibility.

$(BA)_2PbI_4$ was tentatively synthesized following the procedure by M. Tremblay *et al.*,[32] and some adjustments were applied to the process to optimize the reaction. As reported, PbI_2 dissolution into HI (water-based solution 57% wt.) was favored by heating and stirring and using large excess of HI. The use of fresh HI is quite important otherwise it would easily tend to degrade and form polyiodides when mixed with the other reagents. Differently from M. Tremblay *et al.*, the amine was injected directly into PbI_2 and HI solution, without dissolving into methanol before, since BA is liquid at room temperature (RT) and methanol can interfere with perovskite structure formation. In addition, the reaction was carried out under inert atmosphere (N_2) to avoid environmental factors to alter the structure arrangement and to further protect from degradation. Finally, although the orange powder evidently appeared immediately after the injection of the amine, the bath was maintained at reflux for about 45', in order to maximize the yield of reaction, and cooled to RT with very low cooling speedy in order to get crystalline powder. A fundamental step was washing the powder with diethyl ether at RT, first in the reaction flask and then many times on

the filter, till the powder was completely orange without any trace of dark polyiodides, which unavoidably formed during the reaction. The procedure concluded with drying step (under vacuum) in order to completely remove any solvent residue. The 2D perovskite structure formation was confirmed by the XRPD spectra comparison between the experimental one and the simulation from SC-XRD analysis reported in literature[32] (Figure 62).

The procedure for single-crystal perovskite synthesis[32] was also tested, and then similarly replicated for all the other compounds. In order to obtain single crystals, a very slow reaction was necessary, thus slow diffusion crystallization method was adopted. The solutions were stratified into a vial, with an extra interlayer of methanol separating lead iodide solution and amine, to make the amine slowly diffusing into underneath solution and to avoid the immediate contact between the reactants. The crystals precipitated after few days. Again, in order to be sure that the structure of the solid product corresponded to the expected one ($(BA)_2PbI_4$), and since from SC-XRD only inorganic layers were detected due to the typical structural disorder of organic phase in presence of aromatic rings, its XRPD simulated spectrum was compared with the one previously obtained and the simulation from literature[32] (Figure 62).

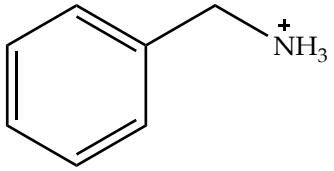

Figure 61. *Schematic representation of benzylammonium cation, BA.*

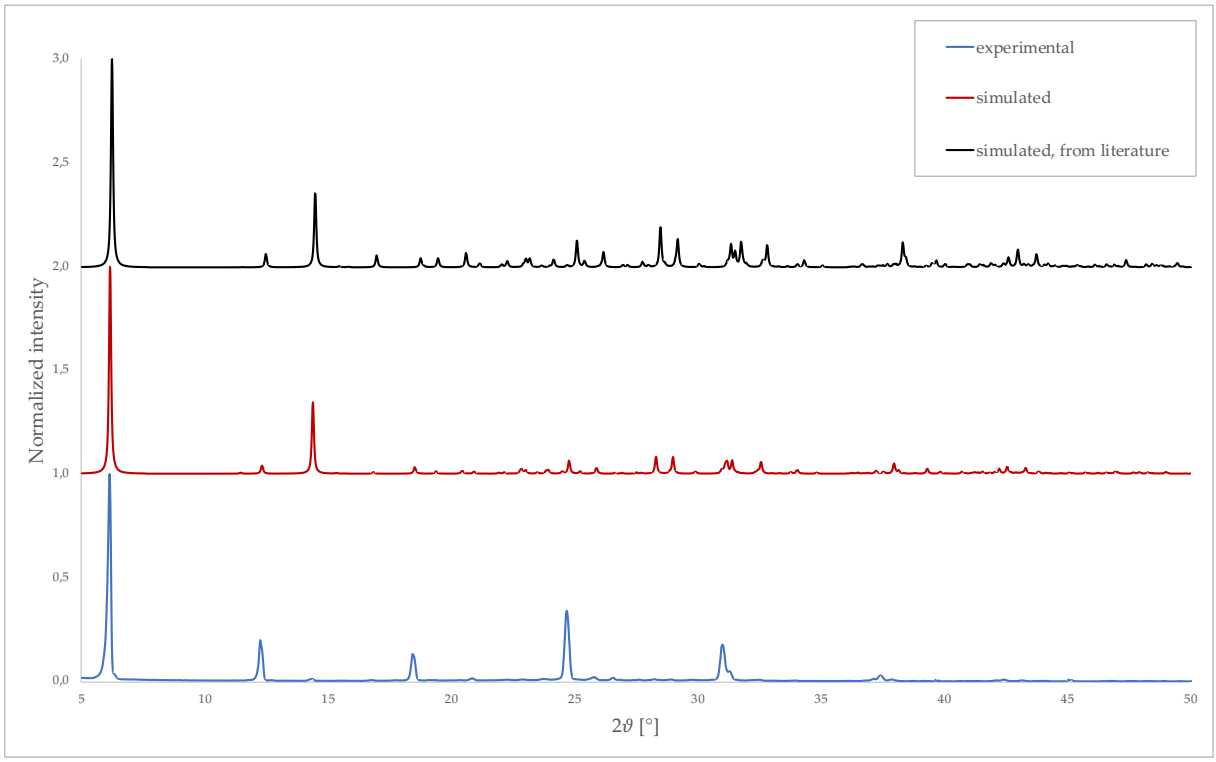

Figure 62. *XRPD spectra comparison: in black the pattern simulated after SC-XRD analysis reported in literature;*[32] *in red the pattern simulated after SC-XRD analysis on single crystals; in blue the experimental pattern after XRPD analysis conducted on crystalline powder.*

Once validated the synthesis procedure, new perovskites were produced. In order to begin to investigate halogen bonding, 4-iodoanilinium (IA, Figure 63) was selected as aromatic cation. Iodine atom was expected to form weak XB with halide undercoordinated species from lead iodide octahedra (I^-).

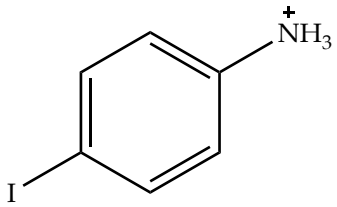

Figure 63. *Schematic representation of 4-iodoanilinium cation (IA).*

First, single crystals of $(IA)_2PbI_4$ were synthesized and analyzed by SC-XRD, completely solving the structure (Figure 64).

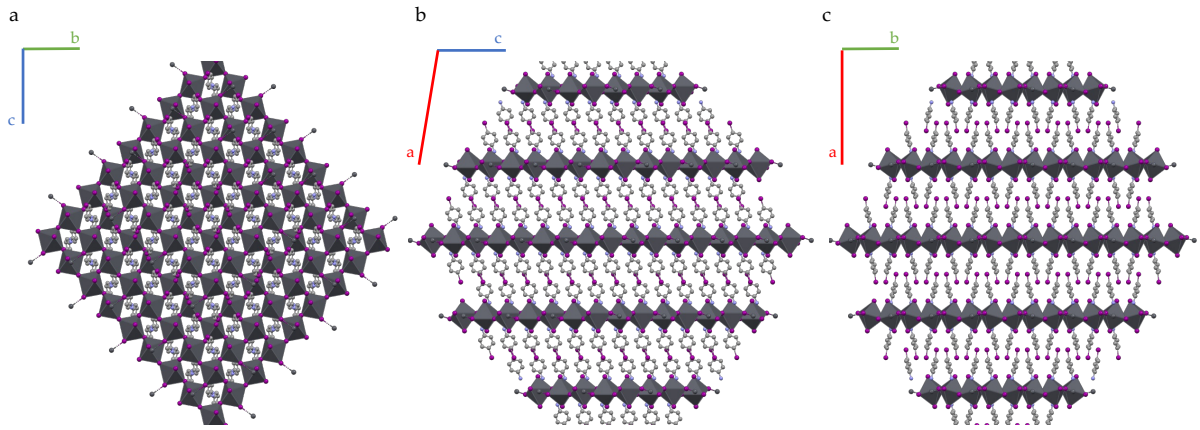

Figure 64. *Crystallographic structure of $(IA)_2PbI_4$ along (a) a cell axis, (b) b cell axis and (c) c cell axis. H atoms are omitted for clarity.*

The presence of halogen bond was confirmed simply by measuring I···I^- distance and comparing its value with the sum of Van der Waals radii. The distance was measured, as shown in Figure 65, between one I on the aromatic ring and the nearest exposed I^- from the inorganic layer, resulting to be 3.904 Å. Van der Waal radius of iodine atom was reported as 1.98 Å,[84] while Pauling radius (ionic radius) of iodide anion was estimated as 2.06 Å.[85] Thus, I···I^- measured distance emerged to be shorter than 4.04 Å, confirming the existence of XB. However, the percentage reduction length was not so significant (3.4% with respect to sum of VdW radii). C-I···I^- bond angle presented an amplitude of 163.38° (Figure 65), still quite far from linearity, further corroborating the weakness of the interaction.

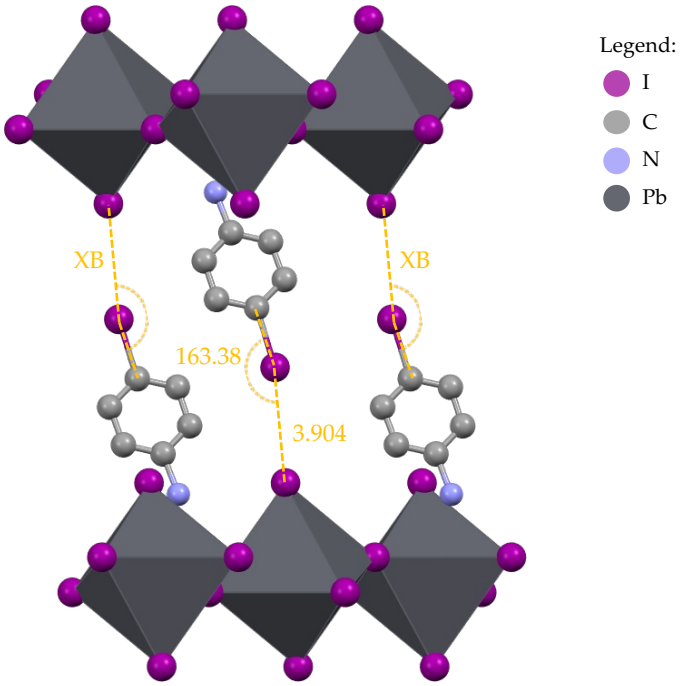

Figure 65. *View from b axis of a portion of $(IA)_2PbI_4$ structure highlighting XB between organic cations and inorganic sheets. In yellow, XB bond length (Å) and XB bond angle (°). H atoms are omitted for clarity.*

Since the analogous halogen-substituted perovskite single-crystal structures were reported in literature,[86,87] the comparison among $(IA)_2PbI_4$ and $(XA)_2PbI_4$ (X = Br, Cl) was worth it, since it could have brought out some property trends related to XB strength. As expected, the X···I^- distance increased in the order I < Br < Cl since IA is a better XB donor than BrA, which in turn is better than ClA. In Table 3, measured distances and angles have been reported, together with theoretical radii, for all three structures. XB exists also for $(BrA)_2PbI_4$ and $(ClA)_2PbI_4$, but, if it was already weak in $(IA)_2PbI_4$, the percentage reduction length is 1.2% and 0.9%, respectively, in its analogues. C-Br···I^- bond angle is unexpectedly higher than the other structures, approaching linearity, but it does not relevantly influence XB strength. The distance between two adjacent inorganic sheets was also measured, getting slightly increasing values in the order Cl < Br < I. It suggested that the layers move apart with the enlargement of the spacer cation, being XB too weak to influence the arrangement. The

interlayer distance trend reflected also in XRPD simulated spectra shift (Figure 66). In particular, the first main isolated peak, which is typically associated to (00l) planes,[47,88] undergoes a shift toward lower values of 2ϑ, confirming the sheets distancing for heavier X atom.

Table 3. *$(XA)_2PbI_4$ measured and calculated parameters for XB estimation and measure of interlayer distance. (v.w. = very weak; w. = weak)*

$(XA)_2PbI_4$	$(ClA)_2PbI_4$	$(BrA)_2PbI_4$	$(IA)_2PbI_4$
X···I^- distance [Å]	3.783	3.862	3.904
$R_{vdW}(X)$[84] + $R_{ionic}(I^-)$[85] [Å]	1.75 + 2.06 = 3.81	1.85 + 2.06 = 3.91	1.98 + 2.06 = 4.04
C-X···I^- bond angle [°]	161.95	172.88	163.38
Halogen bond	v.w. (0.9% red.)	v.w. (1.2% red.)	w. (3.4% red.)
Interlayer distance [Å]	15.087	15.335	15.498

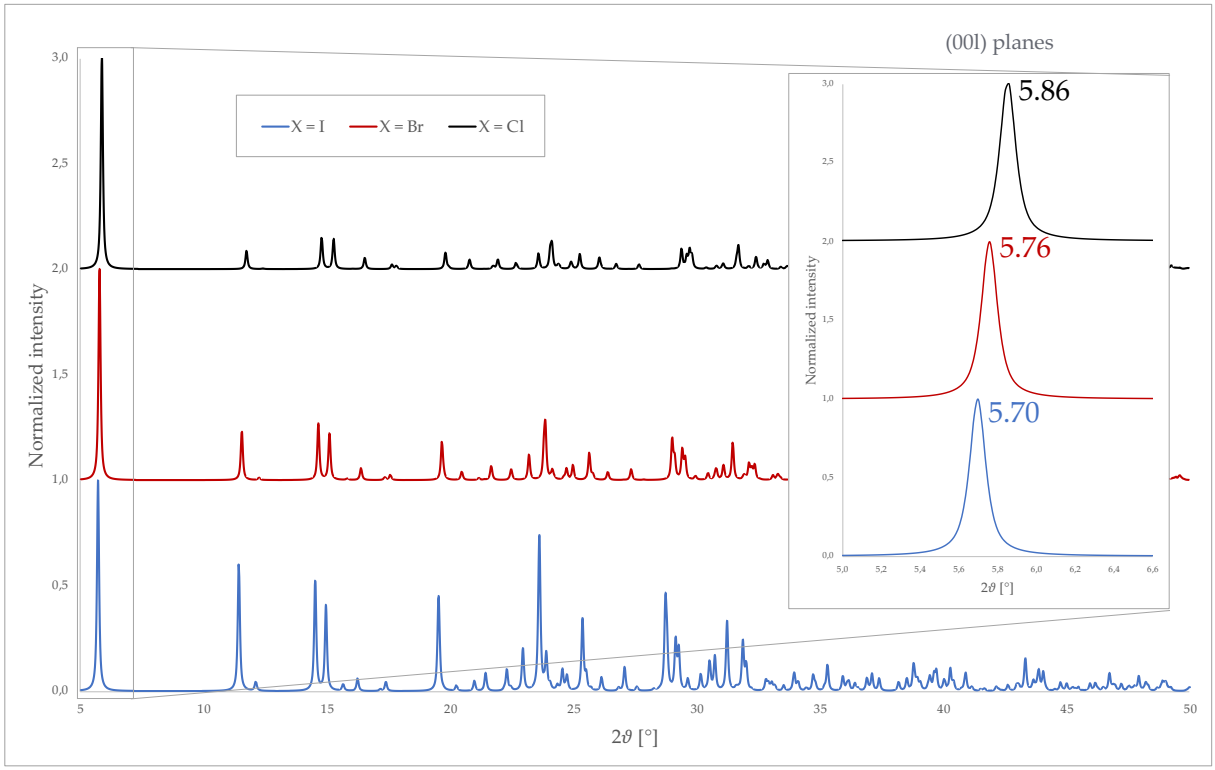

Figure 66. *XRPD spectra comparison for $(XA)_2PbI_4$ structure with X = Cl (black), Br (red), I (blue). The patterns present the same but shifted peaks. The insert highlights the (00l) planes peak shift, with labels indicating the correspondent 2ϑ values [°].*

In order to classify $(XA)_2PbI_4$ perovskites, some other parameters were extrapolated from crystal structures. First, tolerance factors were calculated according to the equation (1), using 1.19 Å and 2.06 Å as ionic radii of Pb^{2+} and I^-,[84] respectively, and obtaining the values shown in Table 4. The calculations were based onto approximated estimations of cations steric hindrance, whose maximum radii (R_A) were conventionally measured as the halved distance between the X atom and the plane containing H atoms of ammonium group. Tolerance factors resulted to be higher than 1.11 for all three structures, as expected for low dimensional perovskites. The structures can evidently be considered as ⟨100⟩-oriented 2D perovskites because of the spatial alternation of monolayers of corner-sharing lead iodide octahedra and bilayers of organic monocations. Taking into account the offset between two adjacent inorganic sheets, that is ~(1/3,1/3) (Figure 67a), it is possible to furtherly label the structures as near-RP 2D perovskites, based on the reiterative graph shown in Figure 67b and referring also to Figure 16b for ideal cases.[32]

Table 4. *$(XA)_2PbI_4$ measured and calculated parameters for structures classification.*

$(XA)_2PbI_4$	$(ClA)_2PbI_4$	$(BrA)_2PbI_4$	$(IA)_2PbI_4$
R_A [Å]	3.118	3.182	3.278
t	1.127	1.141	1.161
Inorganic sheets offset	(1/3,1/3)	(1/3,1/3)	(1/3,1/3)
Structure	⟨100⟩-or. 2D nRP	⟨100⟩-or. 2D nRP	⟨100⟩-or. 2D nRP

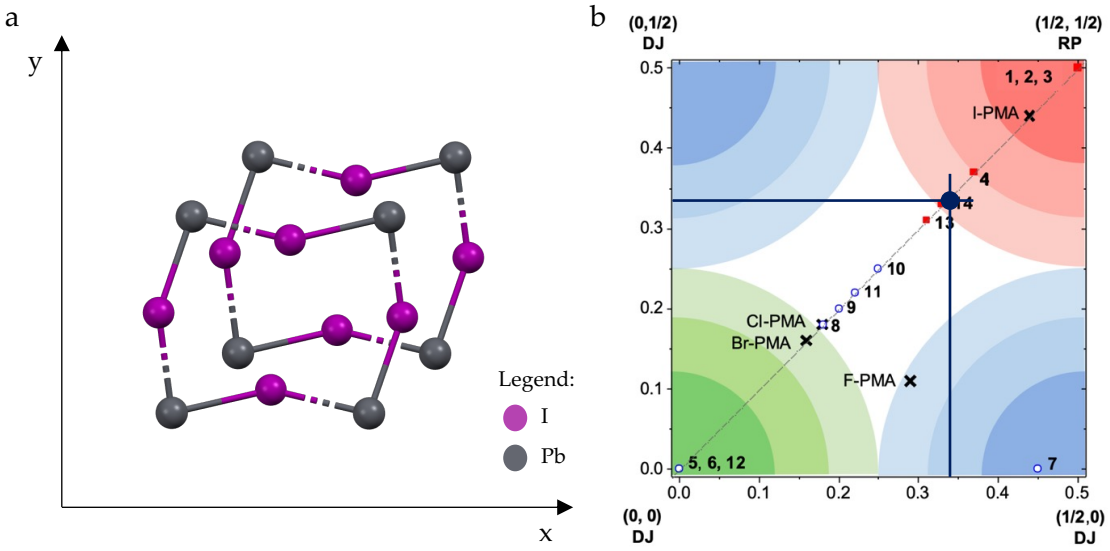

Figure 67. *(a) View along axis perpendicular to (00l) planes of a portion of two adjacent inorganic layers for $(IA)_2PbI_4$, showing the two cells being shifted of 1/3, both along x and y axes. (b) Map matching all possible offsets along x and y axes and classification of 2D perovskites, with the inclusion of $(IA)_2PbI_4$.*[32]

Furthermore, crystal structures provided the possibility to measure distortion parameters, presented in Figure 22.[47] In order to find a trend for $(XA)_2PbI_4$ series, penetration depth (Figure 68), Pb-I-Pb bond angle (Figure 69) and out-of-plane distortion were measured for the three structures and reported in Table 5, too, where V_{oct} represents the volume of the distorted octahedron, L and d_0 stand respectively for the edge and vertex-center distance (Pb-I bond length) of a regular isovolumetric polyhedron. To better visualize the meaning of the calculated parameters, σ^2 was represented in function of $\langle\lambda\rangle$ in Figure 70. The deeper penetration of IA cation with respect to BrA and ClA into halides plane, even in combination of stronger XB interactions, does not lead to more compact structure (interlayer distance is anyway higher due to enlargement of the cation), which is also the reason why the inorganic framework is less distorted.

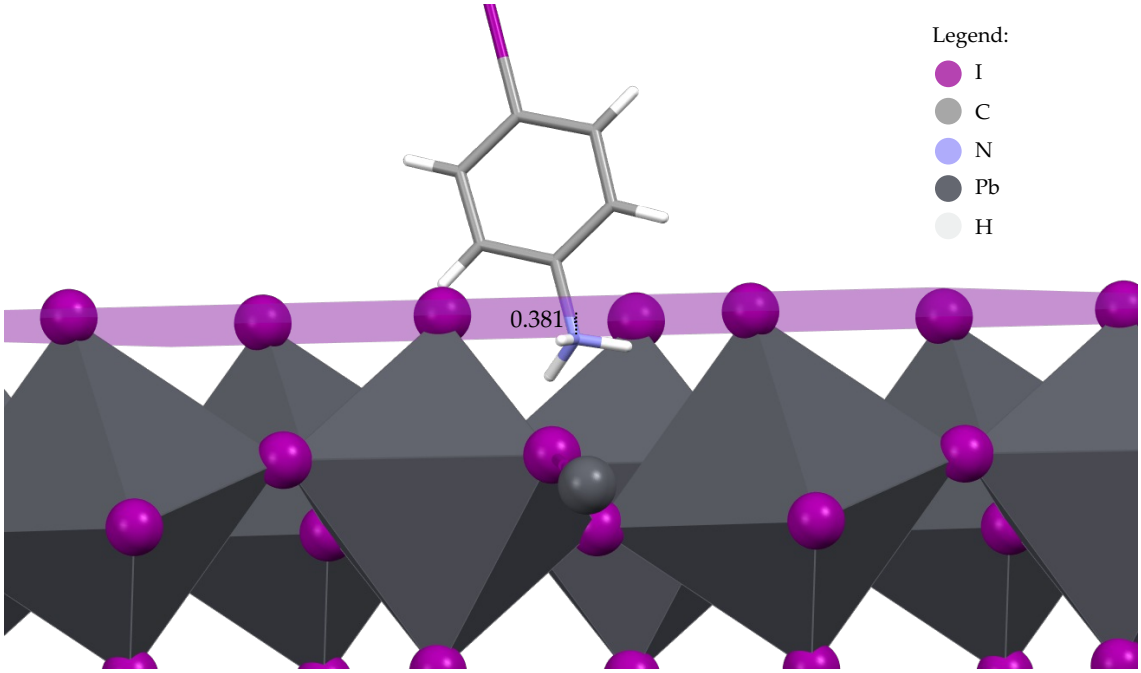

Figure 68. *$(IA)_2PbI_4$ crystal structure highlighting the plane containing octahedra exposed halides (purple) and penetration depth (black dotted line) with the value in Å.*

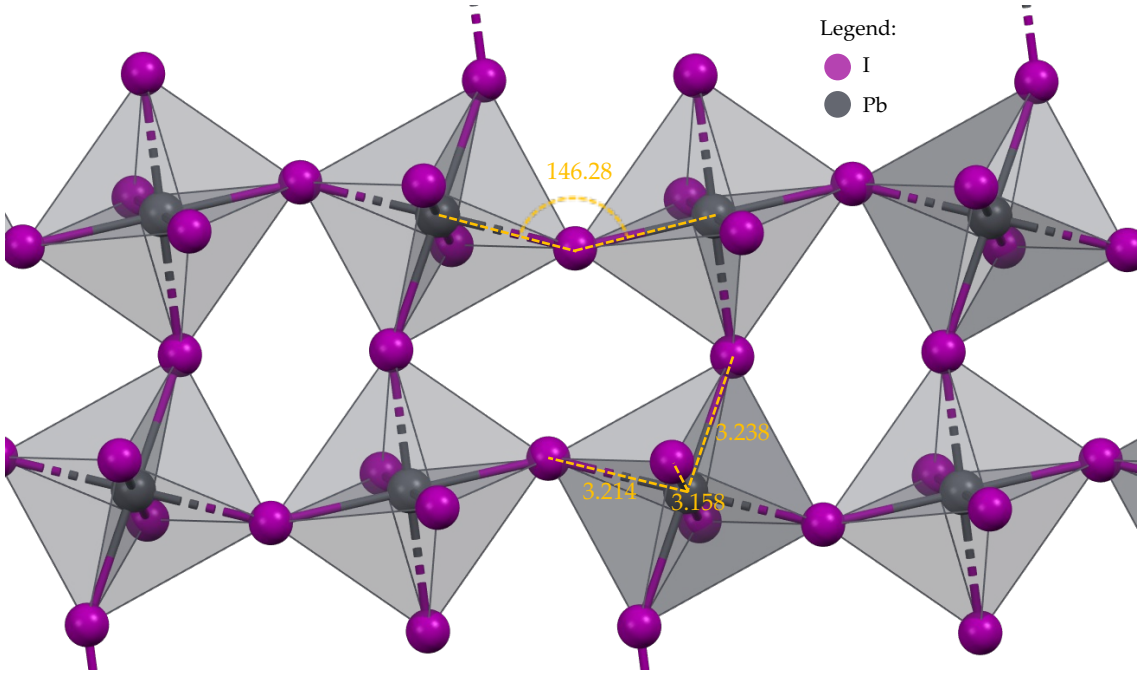

Figure 69. *View along axis perpendicular to (00l) planes of a single inorganic sheet of $(IA)_2PbI_4$ highlighting some octahedra distortions in yellow: Pb-I-Pb bond angle (°) and Pb-I bond length (Å).*

Table 5. *$(XA)_2PbI_4$ measured distortion parameters.*

$(XA)_2PbI_4$	$(ClA)_2PbI_4$	$(BrA)_2PbI_4$	$(IA)_2PbI_4$
Penetration depth [Å]	0.344	0.344	0.381
Pb-I-Pb bond angle [°]	143.01	144.35	146.28
Pb-I bond length (d_i) [Å]	3.211	3.225	3.238
	3.188	3.206	3.214
	3.167	3.169	3.158
Out-of-plane distortion [°]	11.64	12.31	13.36
V_{oct} [Å^3]	43.014	43.553	43.712
L [Å]	4.502	4.523	4.526
d_0 [Å]	3.183	3.197	3.201
$\langle\lambda\rangle$	1.00334	1.00217	1.00186
σ^2	11.29767	8.78756	6.17869

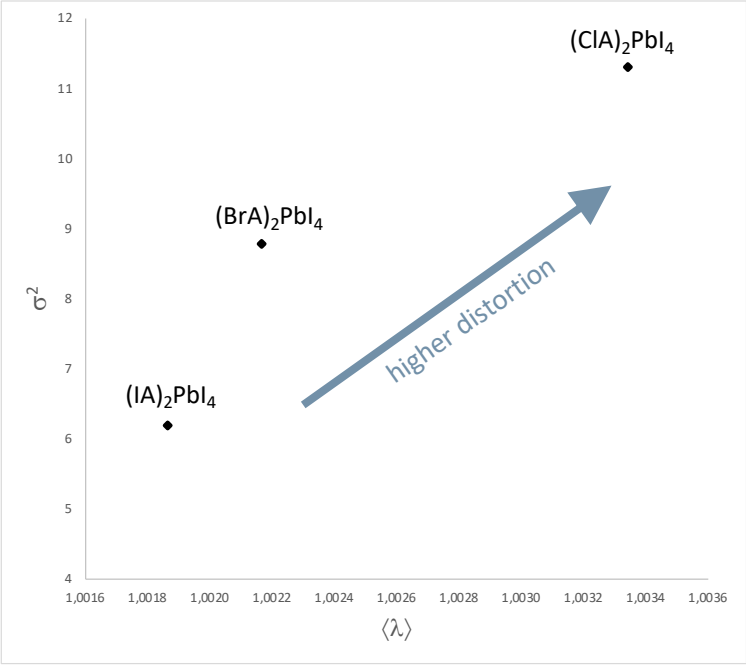

Figure 70. *Graph representing distortion of lead iodide octahedra in $(XA)_2PbI_4$ structures.*

Powder $(IA)_2PbI_4$ was also synthesized following the same procedure validated with $(BA)_2PbI_4$, and a dark yellow powder was obtained. Its structure was verified by comparing its XRPD spectrum with the simulated one (Figure 71).

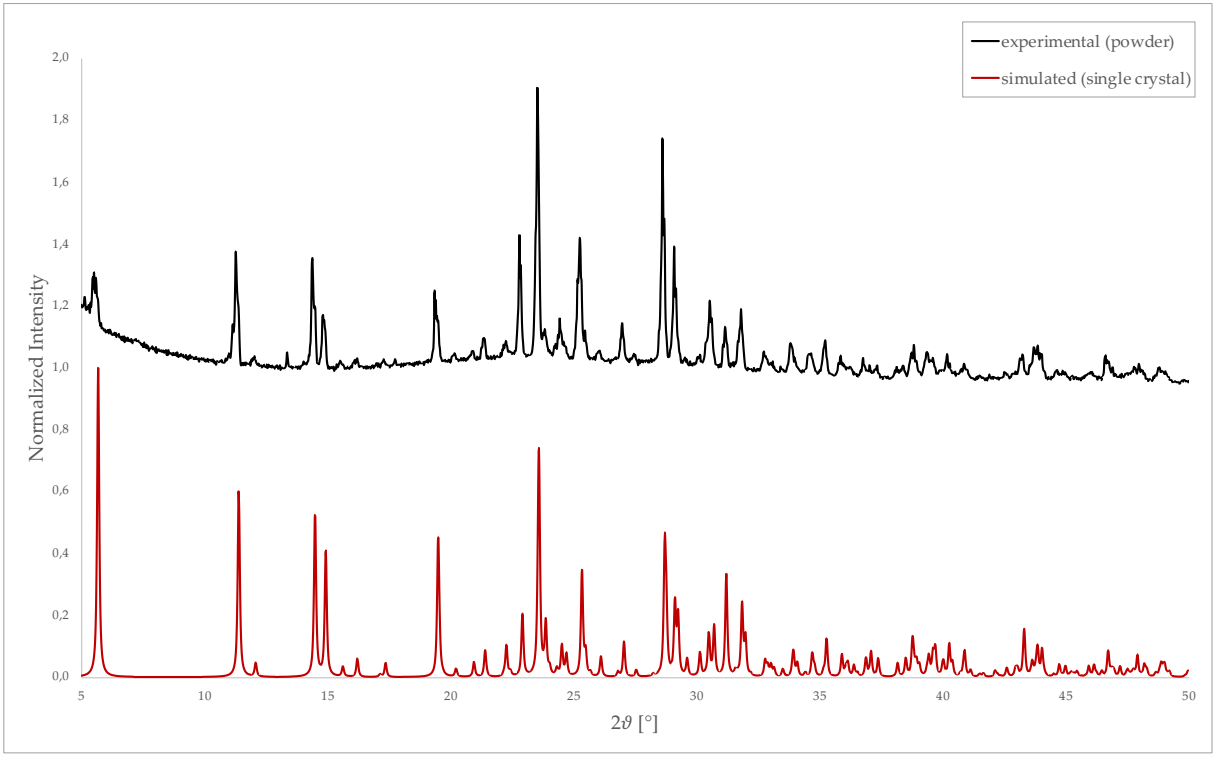

Figure 71. *$(IA)_2PbI_4$ XRPD comparison between experimental spectrum from powder analysis (red) and theoretical spectrum simulated with Mercury (black).*

Evidently, the two spectra presented coincident peaks, thus confirming the same $(IA)_2PbI_4$ structure also for the powder compound. Thermal properties were studied through TGA and DSC analyses, while FT-IR and Raman spectroscopies were conducted to eventually correlate the presence of XB to vibrational modes.

From TGA (Figure 72), $(IA)_2PbI_4$ resulted to lose 5% of its weight at 139°C. Supposing that degradation of perovskite occurred first by loss of the organic phase (more volatile) and then of the inorganic phase, at much higher temperature, percentage calculations of compound composition (reported underneath) were done, finding a match between the percentage amount of cations in perovskite and the percentage of

weight lost in the first step. Maximum temperature of the experiment (500°C) was too low to see the complete degradation of the compound. $(IA)_2PbI_4$ theoretical decomposition occurs as follow:

$$(IA)_2PbI_4 = (I\text{-}C_6H_4NH_3)_2PbI_4 \rightarrow 1154.9 \text{ g/mol} \rightarrow 100\%$$

$$=$$

$$2\ IA = 2\ I\text{-}C_6H_4NH_2 \rightarrow 438.1 \text{ g/mol} \rightarrow 38\%$$

$$+$$

$$2\ HI \rightarrow 255.8 \text{ g/mol} \rightarrow 22\%$$

$$+$$

$$PbI_2 \rightarrow 461 \text{ g/mol} \rightarrow 40\%$$

DSC confirmed degradation temperature at 143°C (Figure 73), and showed that the compound does not undergo any phase transition in the range -50°C – 200°C.

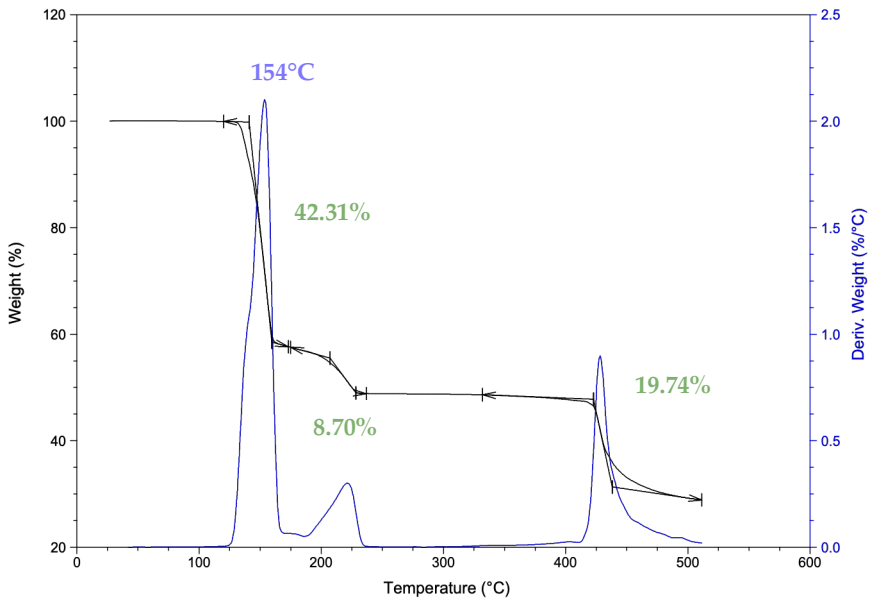

Figure 72. *TGA of $(IA)_2PbI_4$ compound.*

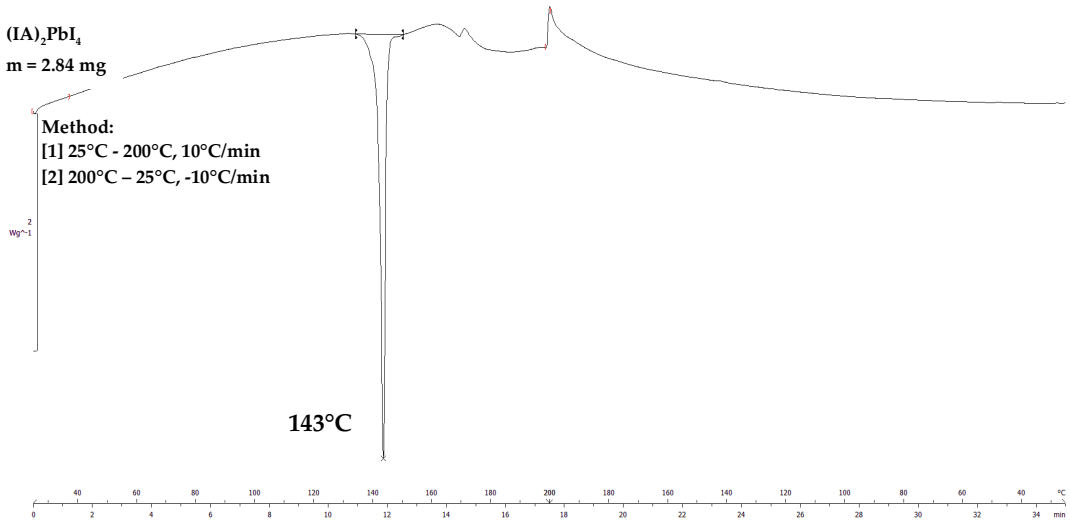

Figure 73. *DSC of $(IA)_2PbI_4$ compound.*

Vibrational modes were also investigated by FT-IR and Raman spectroscopy. $(IA)_2PbI_4$ spectra were compared with correspondent amine (4-iodoaniline, IA) and ammonium salt (4-iodoanilinium iodide, IAI), trying to find a correlation between the different strength of XB interaction and organic modes signals shifts, with a particular focus onto C-I stretching mode. If iodine atom on the aromatic ring was involved into XB interaction, its covalent bond with carbon atom would have been weakened.[89] This fact was confirmed by measuring XB and C-I bond lengths for the three crystal structures (Table 6). IA crystallographic data were taken from literature,[90] while IAI single crystals were synthesized and analyzed by SC-XRD. In IA, iodine from one molecule could have potentially been involved in XB with N atom of another molecule, but the measure of I···N distance did not validate this possibility. While, IAI was proved to contain a stronger XB than perovskite, as expected, because of the higher capability of donating electrons for isolated I^- anions than for I^- from octahedra.

Usually, the smaller the bond dissociation energy (BDE) is, the longer the bond equilibrium (r_0) and the lower the vibrational frequency are.[89] C-I stretching mode was first studied through Raman spectroscopy. The band associated to C-I str. was identified at 247 cm^{-1}, referring to previous studies about IA,[91] which associated main

component of C-I str. to wavenumbers of 241 cm^{-1} (theoretical calculations) and 245 cm^{-1} (experimental value). Nevertheless, the band does not significantly shift in IAI and $(IA)_2PbI_4$ (Figure 75a), even if iodine is involved in XB interactions, due to the fact that C-I bond length is subjected to very slight change, as measured, too small to influence bond vibrational frequency. FT-IR spectroscopy, as expected, was not able to notably detect C-I stretching mode, even if a possible assignment was proposed in Figure 75b, based on the spectroscopic study by N. L. John *et al.*, in which C-I stretching mode was identified with 583 cm^{-1} band.[91] By hypothetically assuming that the same mode can be associated to 582 cm^{-1} in perovskite and 579 cm^{-1} in ammonium salt, the increasing strength of XB interaction reflects into red-shift of C-I str. vibration, as theoretically expected. However, the signals are very weak in the surrounding region, thus they could be blended with background noise. Instead, what emerged from strongest signals is that bands found in the region associated to C-H in-plane bending in IA[91] undergo a blue-shift going to $(IA)_2PbI_4$ and then to IAI, suggesting the coupling between C-I mode and C-H in ring vibrations.

Table 6. *Crystallographic data comparison among IA derivatives for XB strength evaluation.*

IA derivatives	IA	$(IA)_2PbI_4$	IAI
I···A distance [Å]	3.983	3.904	3.754
Sum of VdW radii [Å]	1.98 + 1.55 = 3.53	1.98 + 2.06 = 4.04	1.98 + 2.06 = 4.04
C-I···A bond angle [°]	107.29	163.38	166.20
Halogen bond	no	3.4% red.	7.1% red.
C-I bond length [Å]	2.093	2.096	2.108

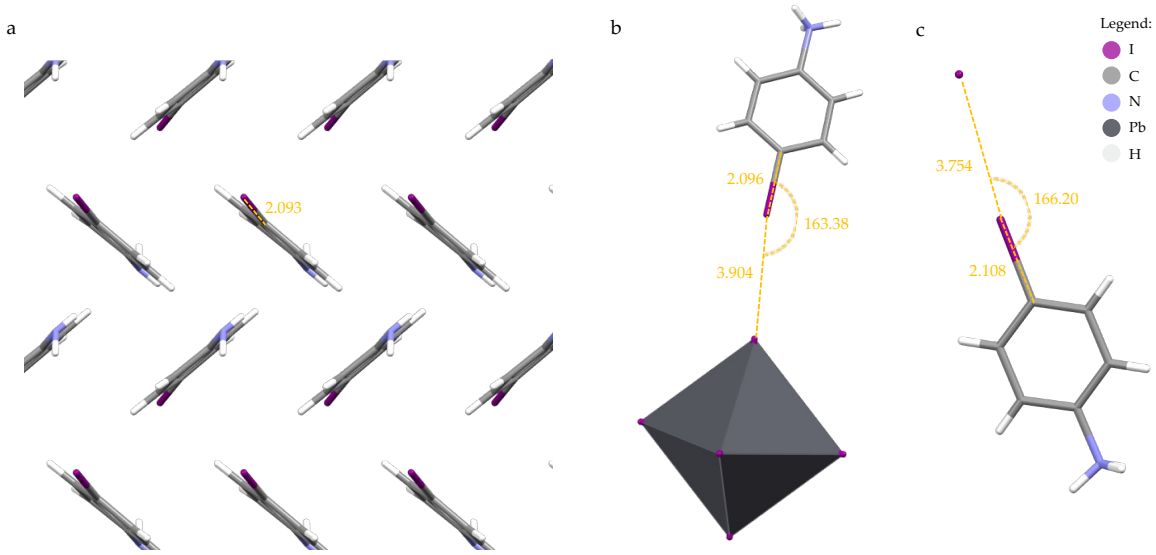

Figure 74. *Crystal structures of (a) IA, (b) $(IA)_2PbI_4$ and (c) IAI, highlighting XB length and angle and C-I bond length in yellow.*

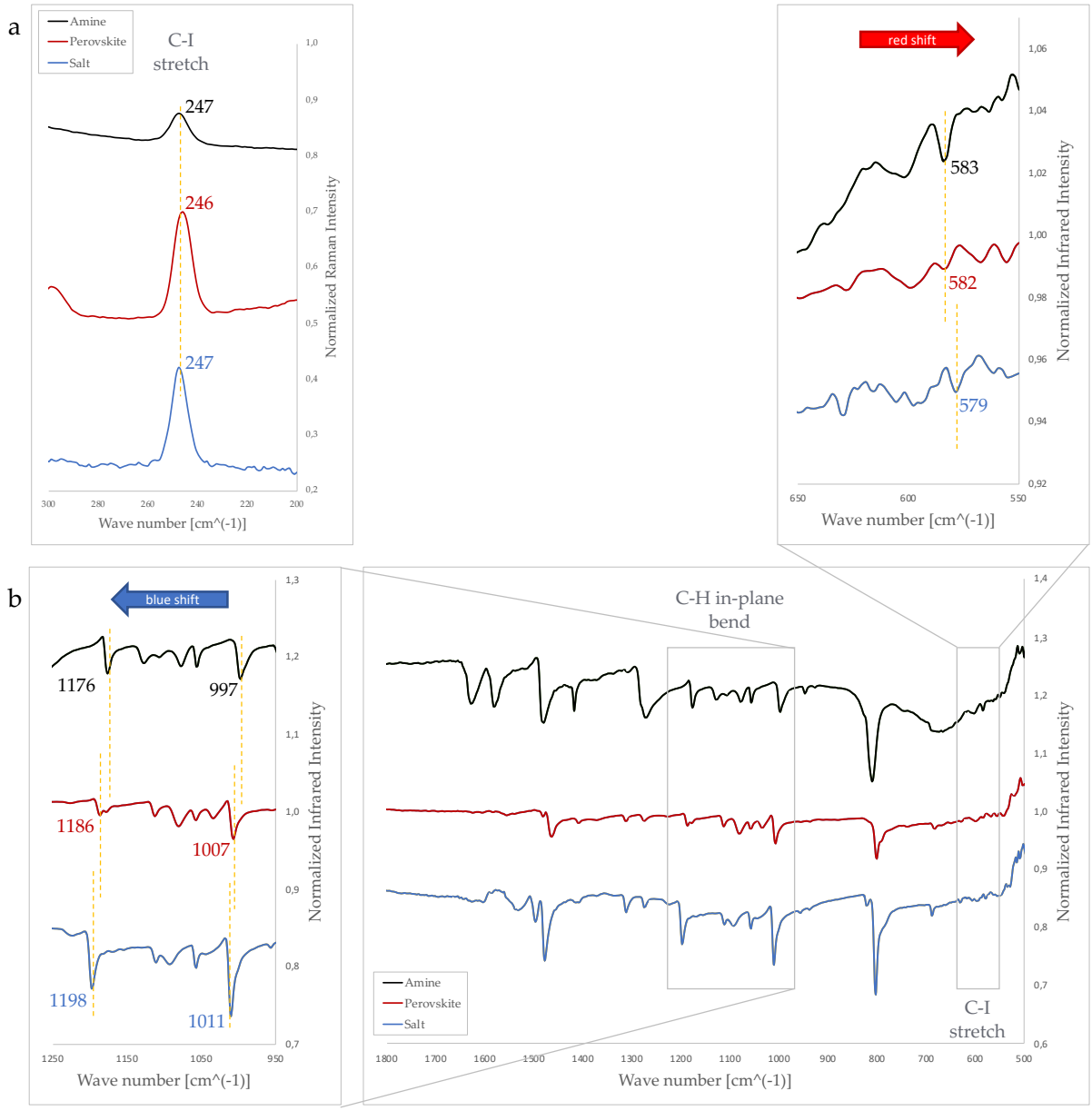

Figure 75. *(a) Raman spectra comparison of IA derivatives in wave number range of 200-300 cm^{-1} to highlight C-I stretching mode. (b) Infrared spectra comparison of IA derivatives in wave number range of 500-1800 cm^{-1}, with inserts for zooming on C-H in-plane bending and C-I stretching regions.*

Aiming to study a much stronger XB interaction between organic species and inorganic framework, a new cation was introduced in the lattice: ((2,3,5,6-tetrafluoro-4-iodophenyl)-aminoethyl)ammonium, I-FEA. It was selected because of its

potentiality as strong XB donor, thanks to the fluorination of the aromatic ring, which favor the formation of a highly electropositive σ-hole onto I atom. Its halogen-substituted analogues - ((2,3,5,6-tetrafluoro-4-bromophenyl)-aminoethyl)ammonium (Br-FEA) and ((2,3,5,6-tetrafluoro-4-chlorophenyl)-aminoethyl)ammonium (Cl-FEA) - were additionally employed, in order to evaluate possible trends in function of XB strength (Figure 76). First, fluorinated amines - *N*-(4-bromo-2,3,5,6-tetrafluoro)-ethylenediamine (X-FEA, X = I, Br, Cl) – were synthesized, purified, and characterized by ^{1}H and ^{19}F NMR, MS and, if possible, SC-XRD. Synthesis procedure was simple,[92] consisting in stirring X-pentafluorobenzene (X-PFB) with an excess of ethylenediamine ($NH_2(CH2)_2NH_2$) at RT for about 24h. Products purification was more demanding and reduced a lot the yield of reaction, since it required, first, the removal of excess of $NH_2(CH2)_2NH_2$ by extractions with water and chloroform and, then, the isolation of pure amine from an extra aromatic compound resulting from TLC, most likely unreacted X-PFB, through chromatographic column. ^{1}H NMR in deuterated methanol (MeOD) revealed two triplets with main peaks at 3.50 ppm and 2.90 ppm for all three amines, associated to H nuclei from -CH_2 groups on the alkyl chain. Hydrogens from aminic groups were not detected because amines exchanged with the solvent. The quintuplet at 3.35 ppm and the single peak at 4.78 ppm observed in NMR spectrum of Figure 77 owned, respectively, to MeOH and H_2O impurities present in MeOD and were used as reference. ^{19}F NMR experiments were also conducted in MeOH, finding, as expected, two multiplets for each compound. The comparison among the three amines helped in associating each peak to a couple of equivalent F atoms. Evidently, the most shifted peak (-147 ppm for X = Cl, -140 ppm for X = Br, -127 ppm for X = I) referred to fluorine atoms adjacent to halogen atom (Figure 78). MS confirmed the chemical composition of the three compounds (Figure 79). Table 7 shows how mass-to-charge ratio (m/z) matched calculated values of molecular weight (MW). Weaker peaks appeared, especially in MS spectrum of Br-FEA, but the relative intensity was such low they could be considered negligible or instrument noise signals.

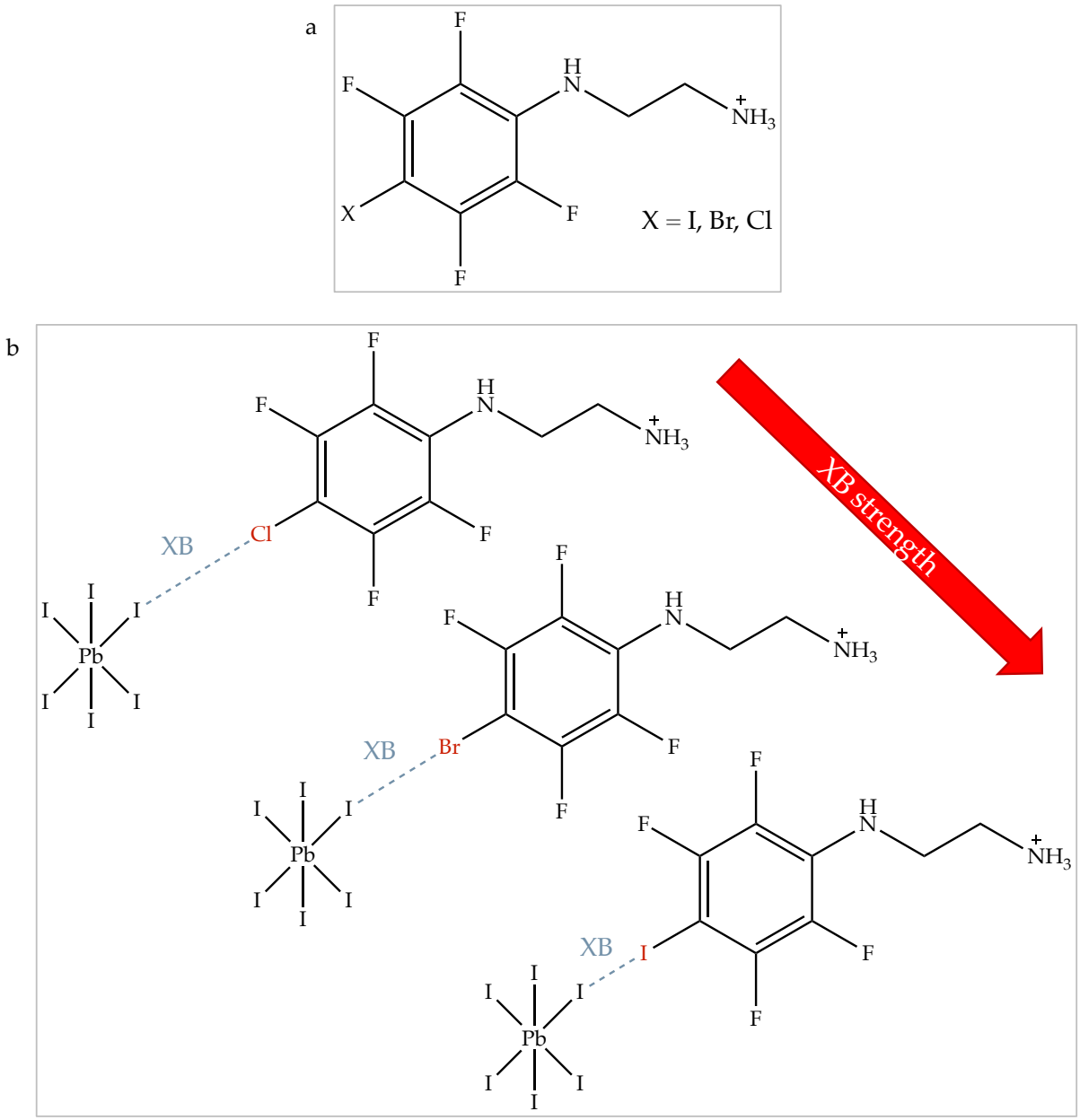

Figure 76. *Schematic representation of (a) (4-X-2,3,5,6-tetrafluoroaniline)-ethan-1-ammonium cation (X-FEA), with X = I, Br, Cl, (b) highlighting the expected variation of interaction strength in perovskite by tuning halogen atom.*

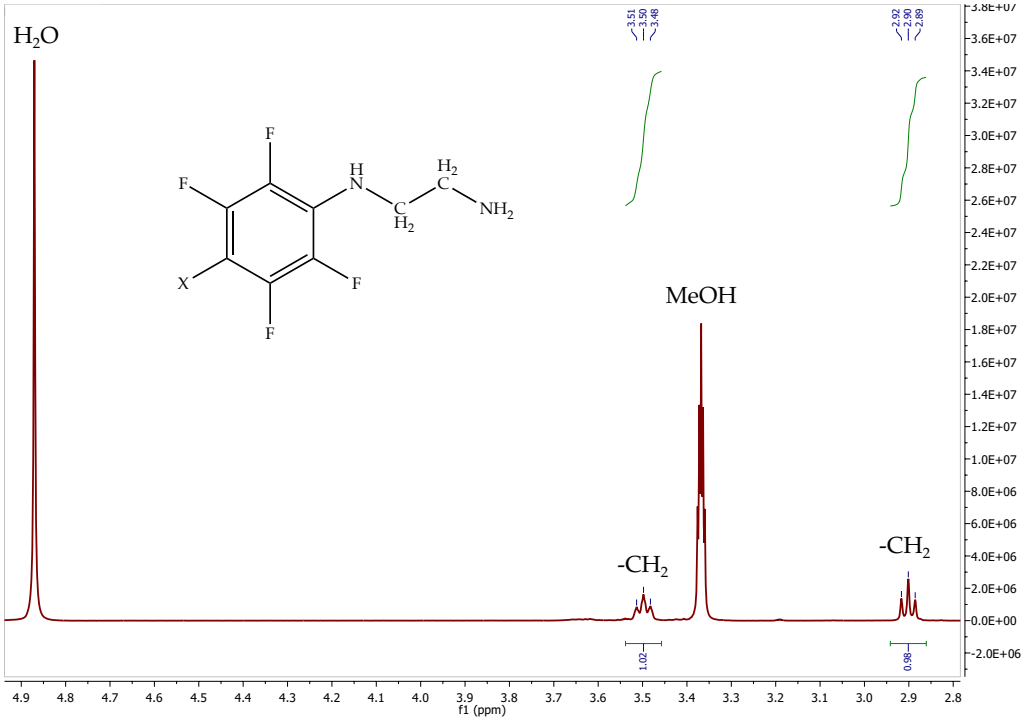

Figure 77. *[1]H NMR spectrum of Cl-FEA in MeOD, valid for all three amines.*

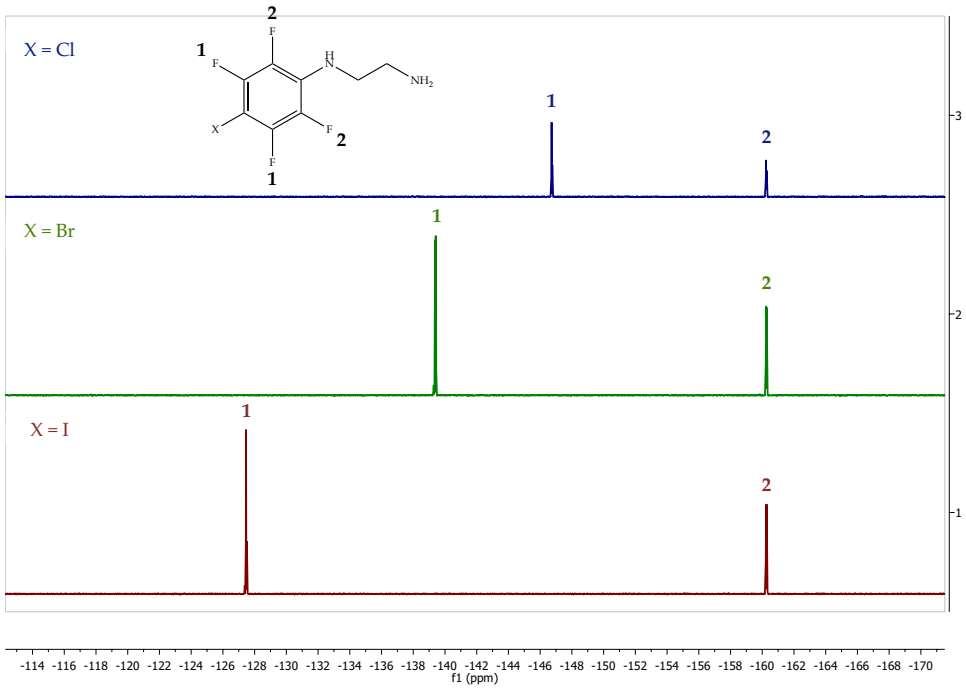

Figure 78. *[19]F NMR spectra comparison of X-FEA in MeOD, after aligning peaks* **2** *at -160 ppm.*

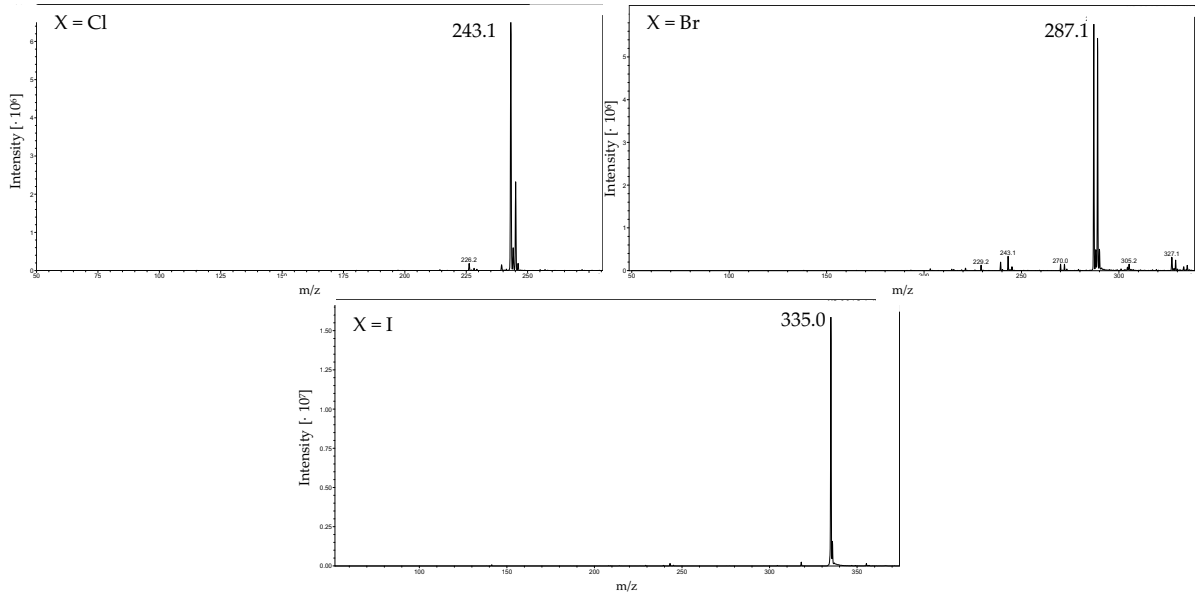

Figure 79. *MS spectra of X-FEA compounds in MeOH-based solution (1mg : 1mL).*

Table 7. *Comparison between expected molecular weight and experimental mass-to-charge ratio for X-FEA compounds.*

	Calculated MW [g/mol]	Experimental m/z
Cl-FEA	242.603	243.1
Br-FEA	287.054	287.1
I-FEA	334.054	335.0

Once the composition and pureness of the amines were ascertained, they were employed for the synthesis of ammonium salts (X-FEAI) and perovskites ((X-FEA)$_2$PbI$_4$). The procedures were the same followed for previous compounds. X-FEAI were characterized through ^{1}H and ^{19}F NMR in MeOD and MS, too. ^{1}H NMR spectra comparison between ammonia and amines allowed to associate the triplet peaked at 3.22 ppm to hydrogens from -CH$_2$ group nearest to primary amine, since peak **2** (Figure 80) was subjected to the strongest shift after protonation of the compound. The extra peak at 3.39 ppm in salt spectrum was associated to residual MeOH from reaction. ^{19}F NMR and MS confirmed the composition and pureness of the salts, without any significant shift with respect to amines results, as expected, due to the

high spatial distance of fluorine atoms from the protonated group. Negative part of MS spectra for eventual anions detection suggested that no polyiodides (I^{3-}, I^{5-}, I^{7-}) were formed.

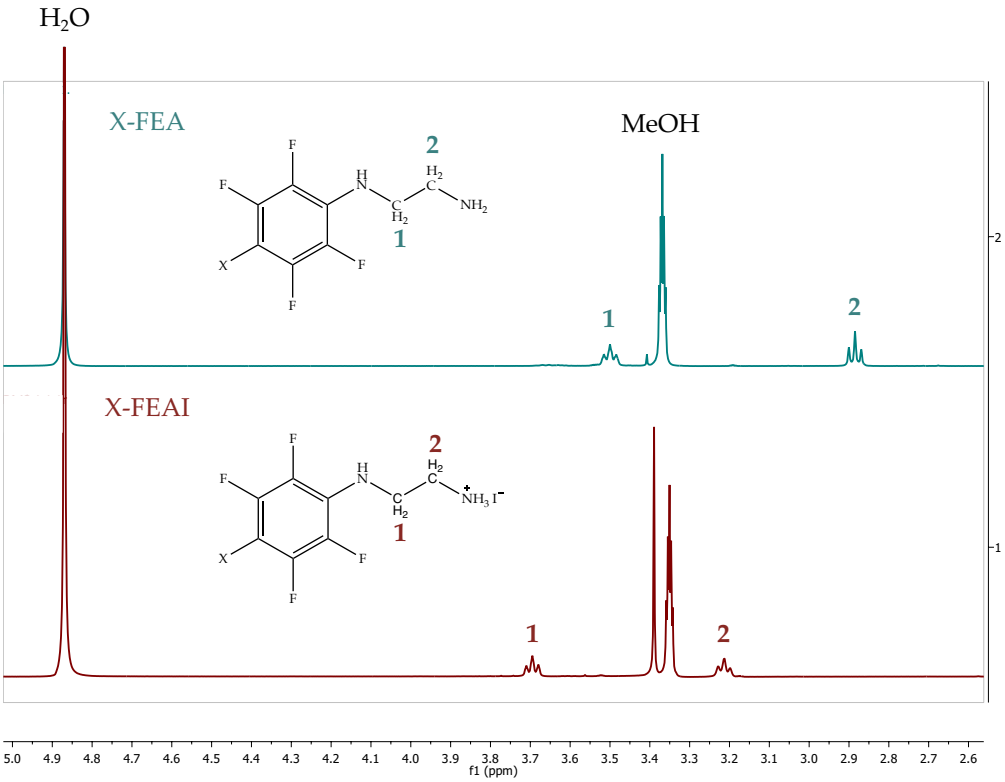

Figure 80. *^{1}H NMR spectra comparison between I-FEA and I-FEAI, valid also for X = Br, Cl.*

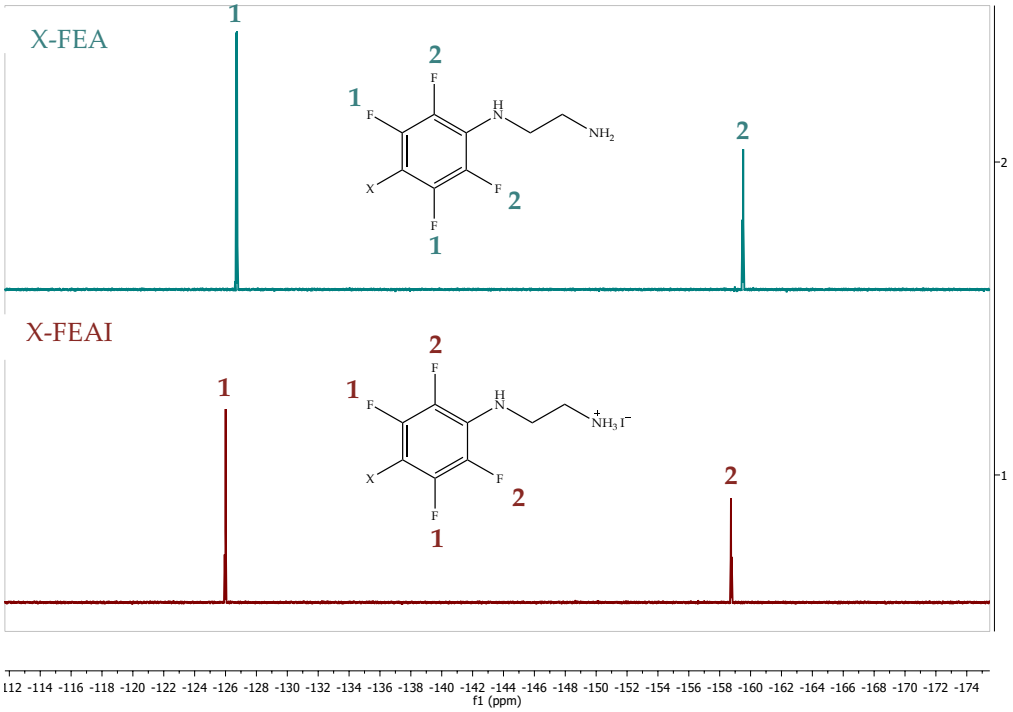

Figure 81. *^{19}F NMR spectra comparison between I-FEA and I-FEAI, valid also for X = Br, Cl.*

$(X\text{-}FEA)_2PbI_4$ perovskites were finally synthesized, starting from X-FEA amines, and extensively characterized. The bright-orange crystalline powders reported in Figure 82 were obtained. As shown in Figure 83, the morphology of $(I\text{-}FEA)_2PbI_4$ appeared rich of ledges and flat domains, probably templated by the crystalline 2D layered structure, which made the crystal grains grow in preferential directions. Unfortunately, due to the high disorder of the structure, SC-XRD analysis was not useful to reveal the crystalline arrangement: it was not possible the solve the structure even at low temperatures (100 K). Thus, other experiments were conducted to indirectly understand lattice coordination and dominating interactions. XRPD, together with theoretical considerations about tolerance factor and similarity with other aromatic perovskites,[27] enabled to confirm the formation of 2D perovskites, due to the typical first isolated peak, associated to (00l) planes. The comparison of XRPD spectra of $(X\text{-}FEA)_2PbI_4$ with PbI_2 peaks (Figure 84) allowed to exclude the hypothesis of simple formation of solid physical mixture of reagent powders, also suggested from

the bright orange color of the compounds. $(I\text{-}FEA)_2PbI_4$ had completely different peaks from lead iodide, while $(Br\text{-}FEA)_2PbI_4$ and $(Cl\text{-}FEA)_2PbI_4$ spectra presented few peaks in common with the precursor, probably implying the presence of small amount of unreacted PbI_2 in these two compounds. Anyway, obscuring these extra peaks, the main patterns correspond to the one of $(I\text{-}FEA)_2PbI_4$, but shifted, confirming the formation of perovskites. XRPD analysis permitted an additional important consideration about lattice arrangement. Graph in Figure 85 shows XRPD spectra of 2D perovskites in a limited range of 2ϑ (up to 7°), allowing to focus only onto the peaks corresponding to planes of inorganic sheets. It is evident that the peak shifts towards lower angles passing from $(BA)_2PbI_4$ to $(XA)_2PbI_4$ to $(X\text{-}FEA)_2PbI_4$, as expected, meaning inorganic layers tend to separate with the enlargement of the cation (Figure 86a). Instead, by focusing onto the three perovskites containing X-FEA cations, the peak shifts towards higher angle passing from Cl to Br to I in X site, contrary to what expected considering cation size effects. This trend could be explained by considering that in $(X\text{-}FEA)_2PbI_4$ organic-inorganic interactions are such relevant to affect interlayer distance more than cation size does (Figure 86b). Indeed, $(I\text{-}FEA)_2PbI_4$ has closer inorganic sheets than $(Br\text{-}FEA)_2PbI_4$, which in turn has lower interlayer distance than $(Cl\text{-}FEA)_2PbI_4$, even though X-FEA enlarges in the order Cl > Br > I, because I is able to form a stronger XB with lead iodide octahedra with respect to Br and Cl.

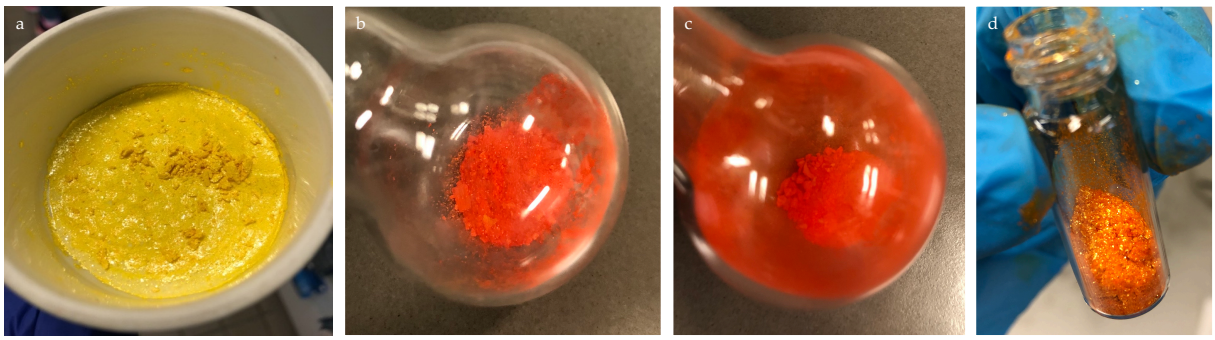

Figure 82. *Photos of (a) PbI_2 on Büchner filter after recrystallization in deionized water, (b) $(Cl\text{-}FEA)_2PbI_4$, (c) $(Br\text{-}FEA)_2PbI_4$, and (d) $(I\text{-}FEA)_2PbI_4$ after drying.*

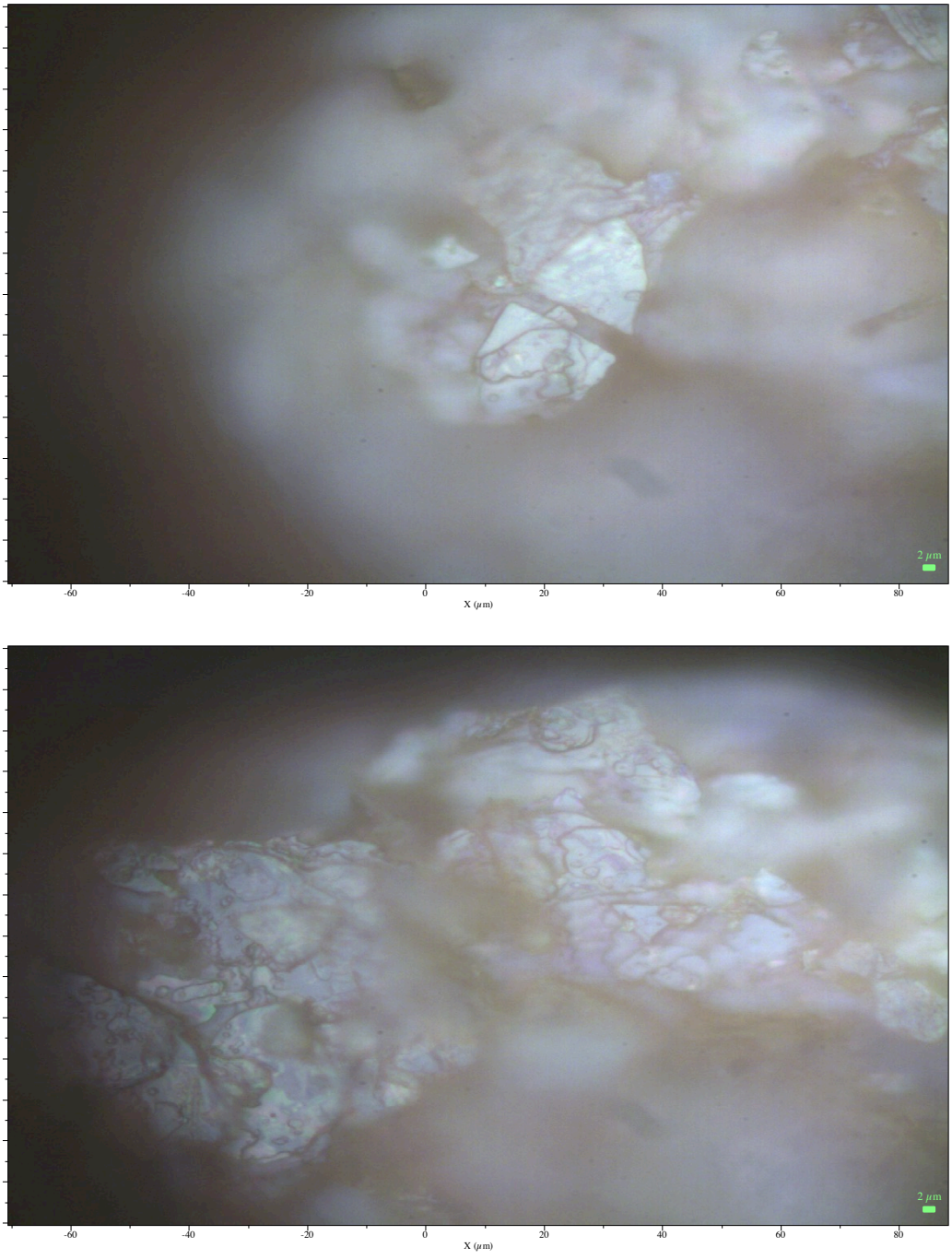

Figure 83. *(I-FEA)$_2$PbI$_4$ images from optical microscope, showing a layered morphology which reflects the 2D molecular structure.*

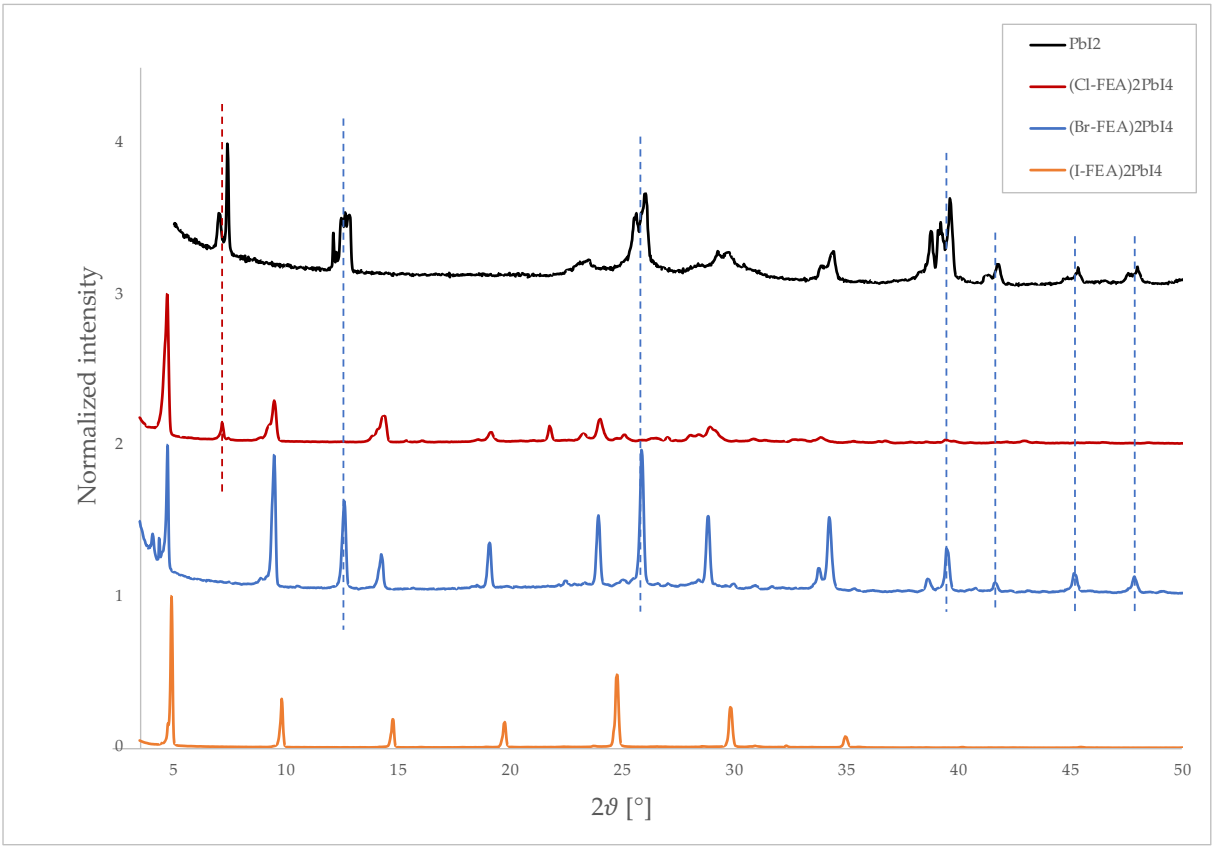

Figure 84. *XRPD spectra comparison among PbI_2 (black) and $(X\text{-}FEA)_2PbI_4$, with X = Cl (red), Br (blue), I (orange). The spotted lines highlight some possible PbI_2 residues in $(Cl\text{-}FEA)_2PbI_4$ and $(Br\text{-}FEA)_2PbI_4$.*

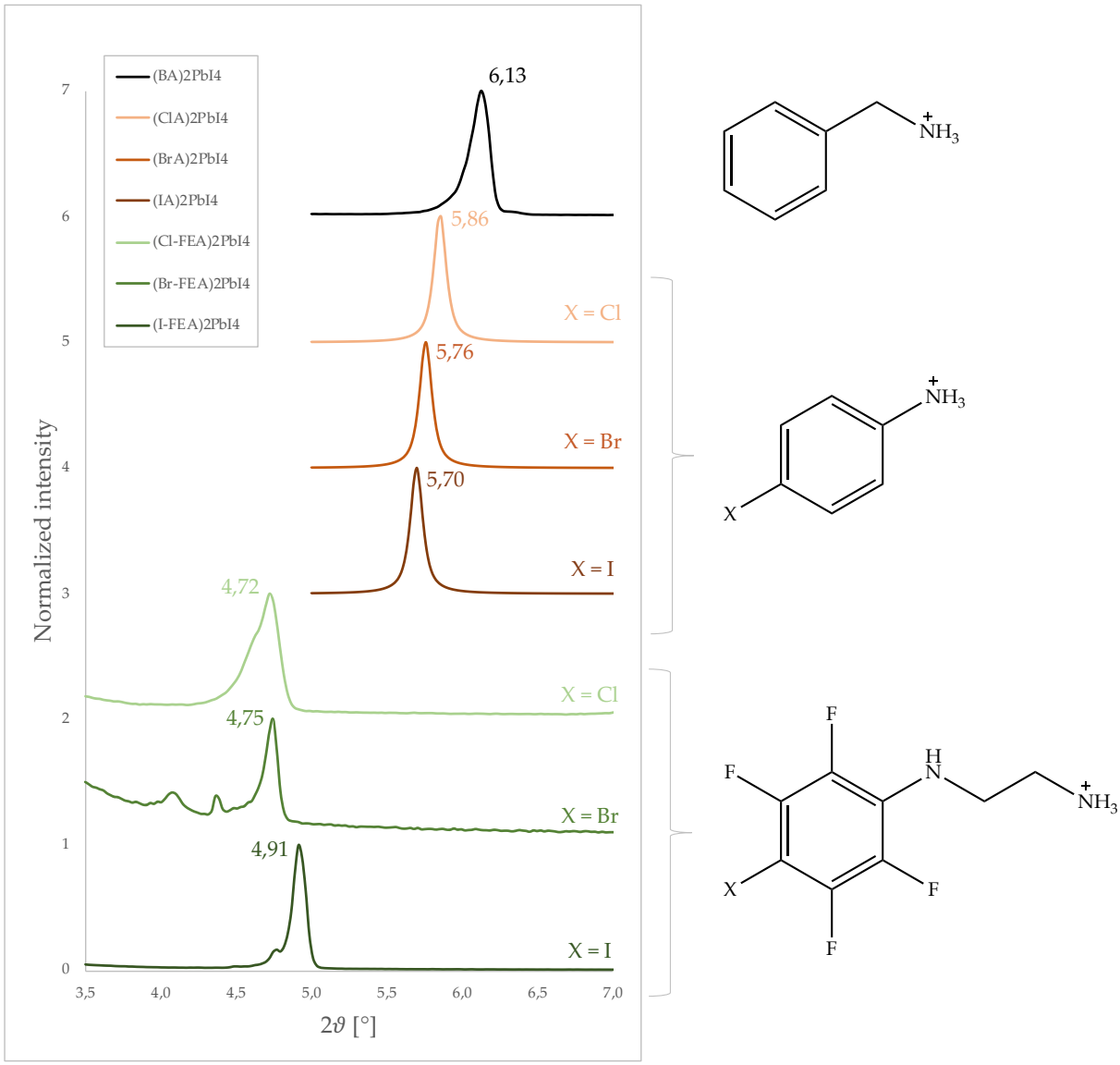

Figure 85. *XRPD spectra comparison among 2D perovskites in increasing order of cation size from top down, for 2ϑ up to 7.0°. Peaks are labeled with correspondent angle values and, on the right side, configurations of cations contained in each perovskite are shown for clarity.*

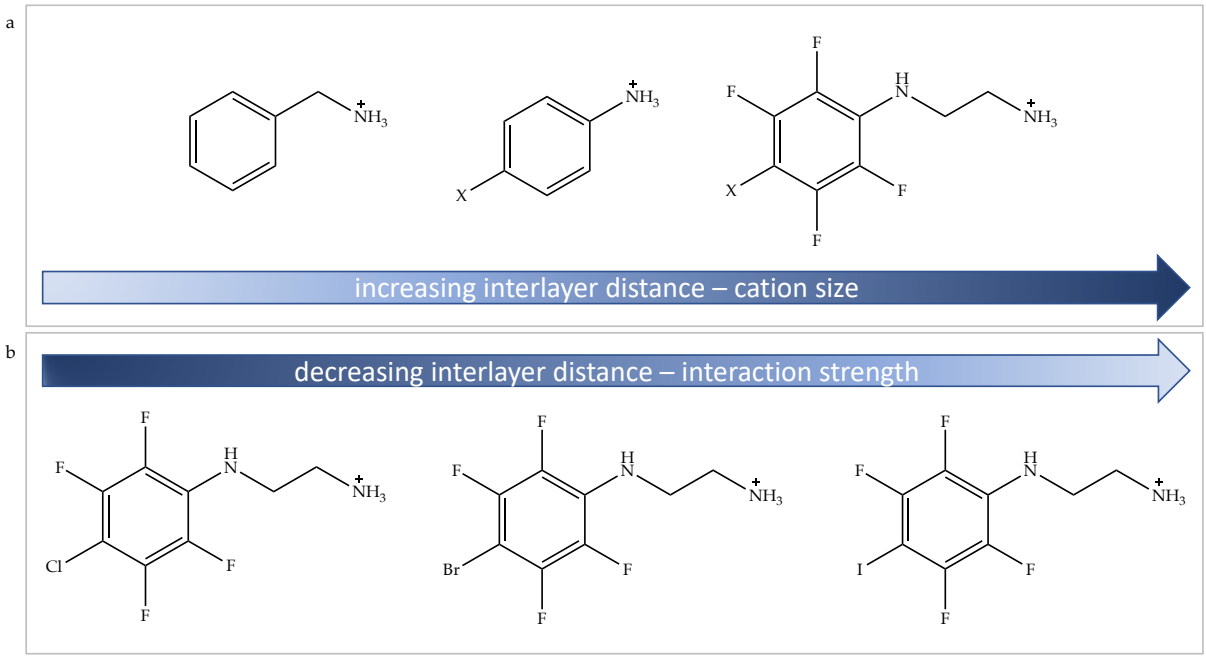

Figure 86. *Schematic diagram representing the trend of a structural property in function of different cations.*

In parallel, thermal properties were studied through TGA and DSC experiments. TGA curves, shown in Figure 87, are characterized by the typical two-step shape, where the first step corresponds to the weight loss of the organic phase (~40-50%), while the inorganic part decomposes at higher temperatures (over 400°C). The maximum temperature of the experiments (500°C) did not allow to observe the complete degradation of the compounds, since the final percentage weight of the perovskites results comprised between 20% and 40%. Anyway, theoretical calculations were sufficient to approximately confirm the assumed stoichiometries:

$$(\text{Cl-FEA})_2\text{PbI}_4 \rightarrow 1\ 202.038\ \text{g/mol} \rightarrow 100\%$$

$$=$$

$$2\ \text{Cl-FEA} = 2\ \text{Cl-F}_4\text{C}_6\text{NH(CH}_2)_2\text{NH}_2 \rightarrow 485.206\ \text{g/mol} \rightarrow \mathbf{40.37\%}$$

$$+$$

$$2\ \text{HI} \rightarrow 255.824\ \text{g/mol} \rightarrow 21.28\%$$

$$+$$

$$\text{PbI}_2 \rightarrow 461.008\ \text{g/mol} \rightarrow 38.35\%$$

$(Br\text{-}FEA)_2PbI_4$ → 1 290.940 g/mol → 100%

=

2 Br-FEA = 2 Br-$F_4C_6NH(CH_2)_2NH_2$ → 574.108 g/mol → **44.63%**

+

2 HI → 255.824 g/mol → 19.82%

+

PbI_2 → 461.008 g/mol → 35.71%

$(I\text{-}FEA)_2PbI_4$ → 1 384.940 g/mol → 100%

=

2 I-FEA = 2 I-$F_4C_6NH(CH_2)_2NH_2$ → 668.108 g/mol → **48.24%**

+

2 HI → 255.824 g/mol → 18.47%

+

PbI_2 → 461.008 g/mol → 33.29%

Notably, $(X\text{-}FEA)_2PbI_4$ perovskites degraded at higher temperatures with respect to $(XA)_2PbI_4$, as expected, because of the lower volatility of X-FEA cations. First flex of TGA curves (corresponding the first peak of derivative weight %) stands around 280-300°C, implying the high stability of the compounds. Through DSC curves presented in Figure 88, degradation temperatures could have been more precisely identified, finding peaks at almost 290°C for X = Br and Cl, and more than 300°C for X = I. The higher thermal stability characterizing $(I\text{-}FEA)_2PbI_4$ suggested a stronger cohesion due to more intense organic-inorganic interactions. No solid phase transitions were observed from DSC analysis in the temperature range -50°C – 300°.

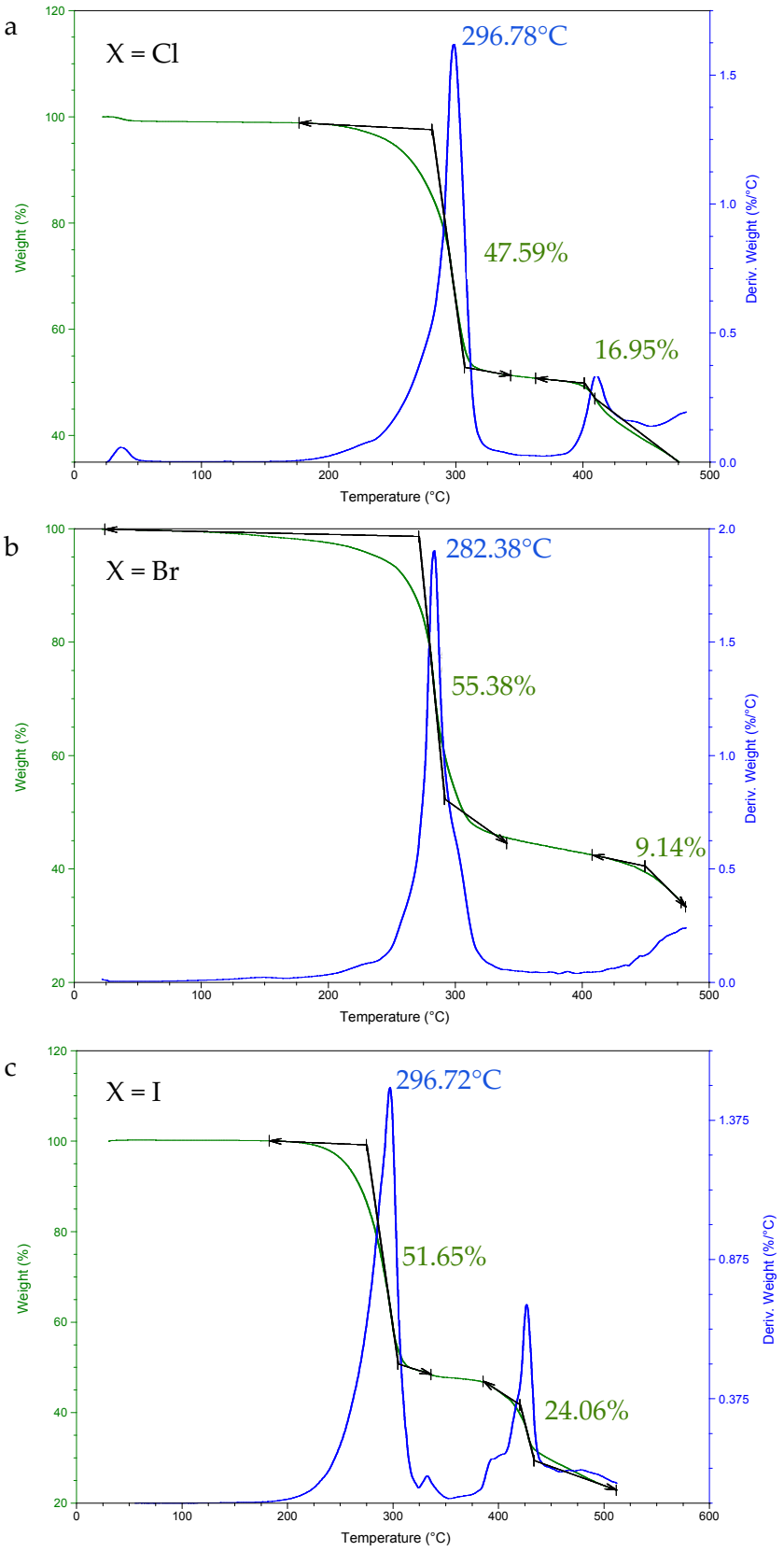

Figure 87. *TGA curves for (X-FEA)$_2$PbI$_4$ compounds, with X = (a) Cl, (b) Br and (c) I.*

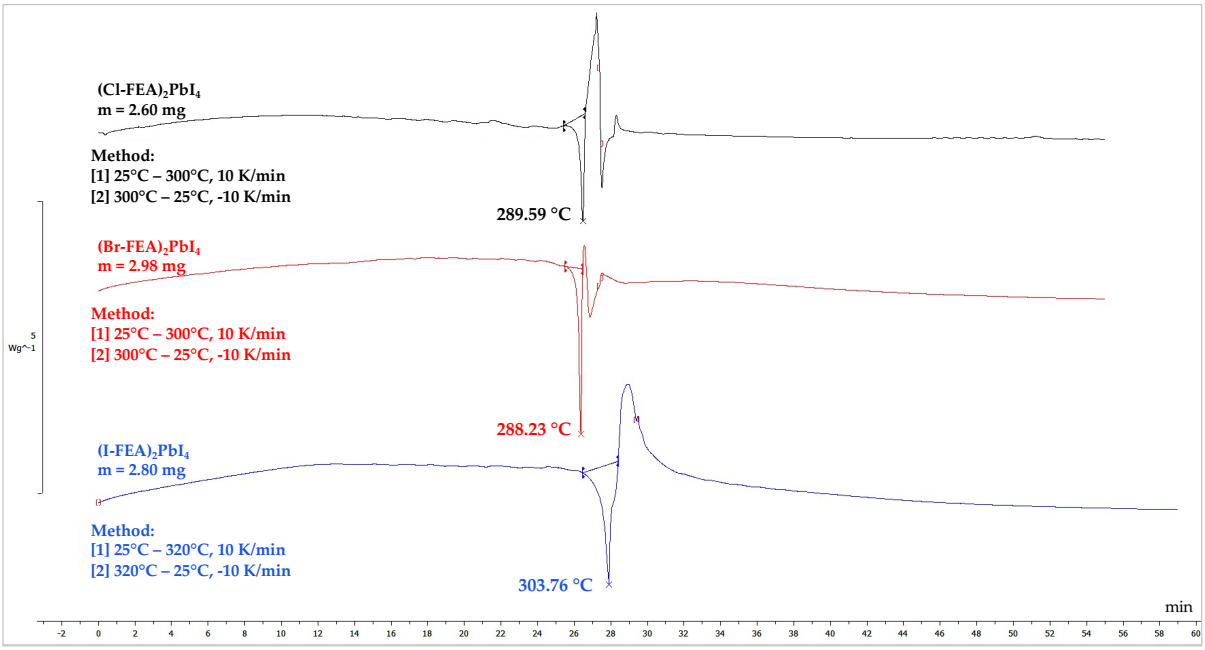

Figure 88. *DSC curves for (X-FEA)$_2$PbI$_4$ compounds, with X = (black) Cl, (red) Br and (blue) I.*

In order to better understand the nature and the strength of organic-inorganic interactions in these perovskites, without the possibility to directly measure I···I distance as for (IA)$_2$PbI$_4$, SC-XRD was successfully conducted onto I-FEA starting amine and some other experiments were selected for comparison with (I-FEA)$_2$PbI$_4$ and I-FEAI. A quite strong XB – percentage of length reduction of almost 20% – resulted to be present in I-FEA single-crystal sample, established between iodine atom and nitrogen atom of two adjacent molecules (Figure 89). The specific measured and calculated values of XB were reported in Table 8.

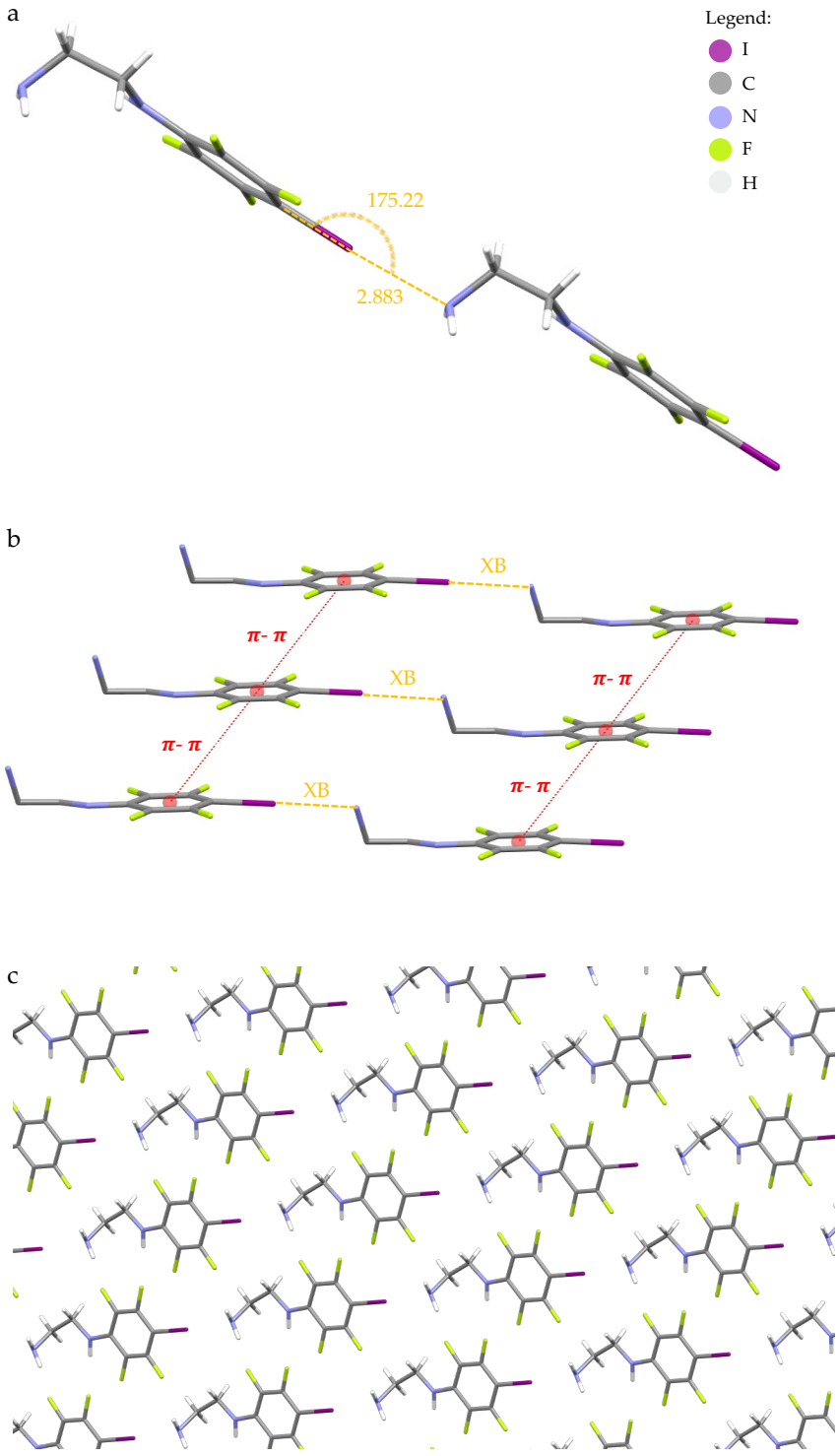

Figure 89. *Crystal structure of I-FEA highlighting (a) XB between two adjacent molecules, with XB length in Å and XB angle in °, (b) main intermolecular interactions and (c) general molecular arrangement. In (b) H atoms are omitted for clarity.*

Table 8. *Crystallographic data related to I-FEA for XB strength evaluation.*

	I-FEA
I···N bond length [Å]	2.883
Sum of VdW radii [Å]	1.98 + 1.55 = 3.53
C-I···N bond angle [°]	175.22
Halogen bond	strong (18.3% red.)

Therefore, XPS, FT-IR, Raman and ss-NMR experiments were conducted onto I-FEA, I-FEAI and $(I\text{-}FEA)_2PbI_4$.

XPS was conducted to compare binding energies relative to iodine atom. The XPS spectrum of perovskite showed a doublet at 620.1 eV/631.6 eV corresponding to binding energy for I 3d orbitals (Figure 90). This doublet accounts for the presence of different iodine species: I covalently bound to the aromatic ring, I^- from PbI_6 octahedra exposed to the organic layer and I connecting two PbI_6 octahedra, which are not all equivalent. By deconvolution and comparison of the different components with amine, ammonium salt and lead iodide, we were able to identify the iodine from organic cations at 622.1 and 633.6 eV (red dotted lines in Figure 90). The deconvoluted spectrum of I-FEAI shows that the same iodine is at 621.5 and 633.0 eV, while in the amine it is at 621.8 and 633.2 eV. These shifts can be correlated to the strength of the interactions involving such iodine and suggest the following trend for the binding energies: salt < amine < perovskite. ΔE_b are small but coherent with values reported in literature[27] (0.2-0.4 eV). In Table 9, Table 10, Table 11 and Table 12 all peaks assignments are specified. I-FEA peaks presented secondary weak shoulders, probably due to the partial acidification of the amine.

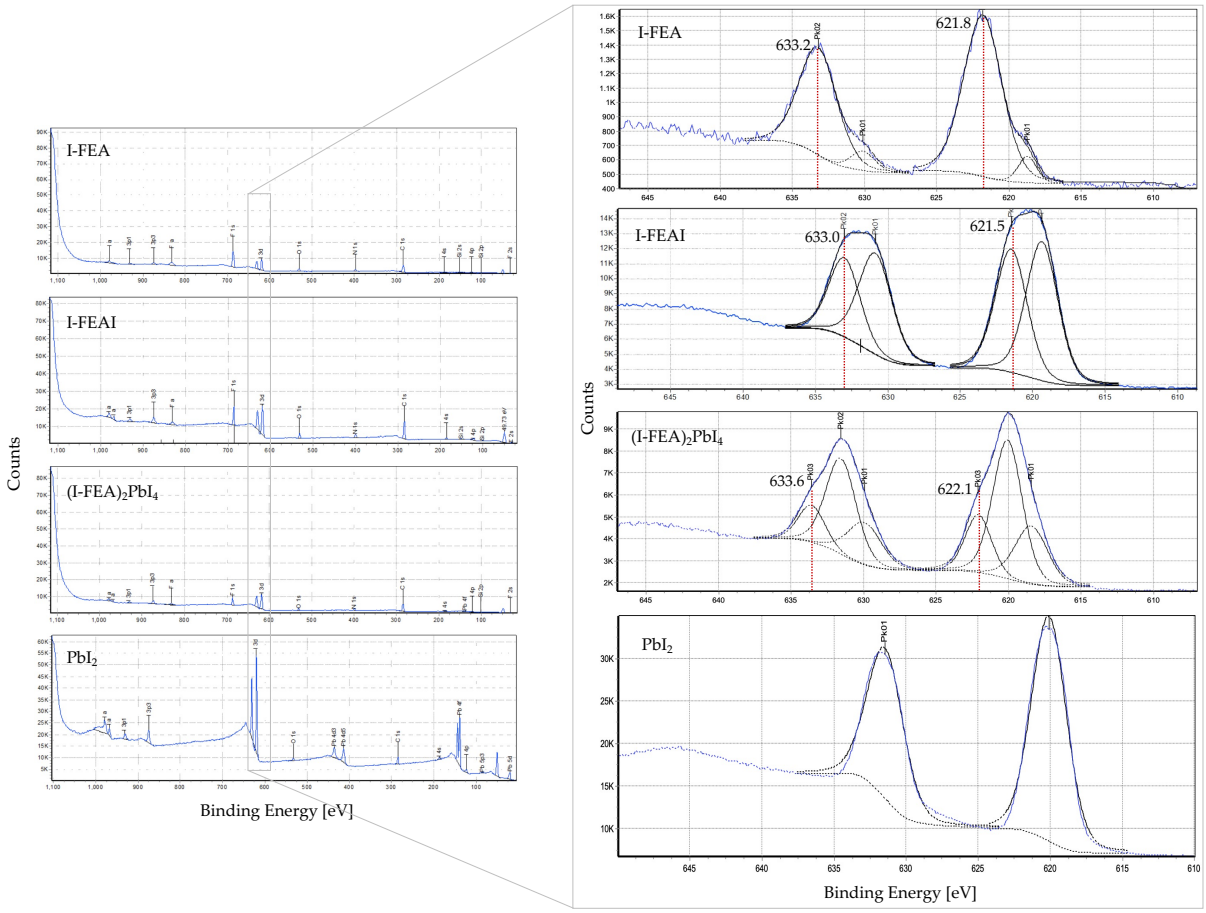

Figure 90. *XPS spectra for I-FEA derivatives and PbI_2, with focus onto iodine peaks region and labels onto peaks relative to iodine species on aromatic rings.*

Table 9. *Components details of deconvoluted iodine peaks from XPS of I-FEA.*

Peak ID	I species	Adj'ed Be	Area	FWHM	Group %
Pk01	impurity	618.7	4 789	1.5	7.4
Pk02	on ring	621.8	59 760	3.1	92.6
Pk01	impurity	630.1	4 557	2.0	10.4
Pk02	on ring	633.2	39 299	3.1	89.6

Table 10. *Components details of deconvoluted iodine peaks from XPS of I-FEAI.*

Peak ID	I species	Adj'ed Be	Area	FWHM	Group %
Pk01	anion	619.4	411 610	2.6	53.2
Pk02	on ring	621.5	362 604	2.6	46.8
Pk01	anion	630.9	307 655	2.7	57.9
Pk02	on ring	633.0	224 122	2.5	42.1

Table 11. *Components details of deconvoluted iodine peaks from XPS of $(I\text{-}FEA)_2PbI_4$.*

Peak ID	I species	Adj'ed Be	Area	FWHM	Group %
Pk01	undercoordinated	618.5	120 616	2.7	25.2
Pk02	connecting two octahedra	620.1	261 101	2.4	54.5
Pk03	on ring	622.1	96 936	2.1	20.3
Pk01	undercoordinated	630.0	90 801	2.7	26.8
Pk02	connecting two octahedra	631.6	185 913	2.5	54.8
Pk03	on ring	633.6	62 339	2.1	18.4

Table 12. *Components details of deconvoluted iodine peaks from XPS of PbI_2.*

Peak ID	Adj'ed Be	Area	FWHM	Group %
Pk01	620.1	1 275 812	2.8	100
Pk01	631.5	890 792	2.9	100

FT-IR and Raman spectroscopies were carried out for the three compounds in order to find a shift of the band relative to C-I stretching. A red-shift would have implied the weakening of C-I bond, due to the involvement of I atom into a stronger XB interaction. FT-IR did not give any useful information because C-I stretching band was not distinguishable (too weak signal to be recognized from the background noise in the FIR region – Far Infrared), while the band was easily allocated in Raman spectrum.[89] Since $(I\text{-}FEA)_2PbI_4$ Raman spectrum was characterized by a complex broad structure at low wave numbers, it was first compared with lead iodide and other 2D perovskites, to understand which contributions were to be attributed to vibrational modes of the inorganic framework. From Figure 91a, it is possible to notice that almost every contribution of the complex structure is found also in the other perovskites and in lead iodide, even if the main peak is quite broad and could be the result of the overlapping of more components. For wave numbers below 100 cm^{-1}, the spectra are not reliable because of the cut of the notch filter being part of the set up. Then, $(I\text{-}FEA)_2PbI_4$ Raman spectra was compared with I-PFB precursor, I-FEA amine and I-FEAI salt, in order to evaluate the eventual shift of the C-I stretching band. Previous Raman characterization of I-PFB[93] was exploited to assign C-I stretching mode to the band at 205 cm^{-1}. The same vibrational mode was intuitively allocated to the intense band at 182 cm^{-1} and 190 cm^{-1} for amine and ammonium, respectively. In the case of perovskite, it was more difficult to distinguish it due to the complex broad band present in the same region, but, thanks to the previous comparison with lead iodide and other perovskites, it was possible to exclude some peaks and suppose that C-I stretching mode was below 182 cm^{-1}, under the broad structure. In Figure 91b, it was shown that C-I stretching mode undergoes a red-shift in the order I-PFB < I-FEAI < I-FEA < $(I\text{-}FEA)_2PbI_4$, suggesting an increasing strength of XB in the same order (for the last three compounds) and confirming the results of XPS.

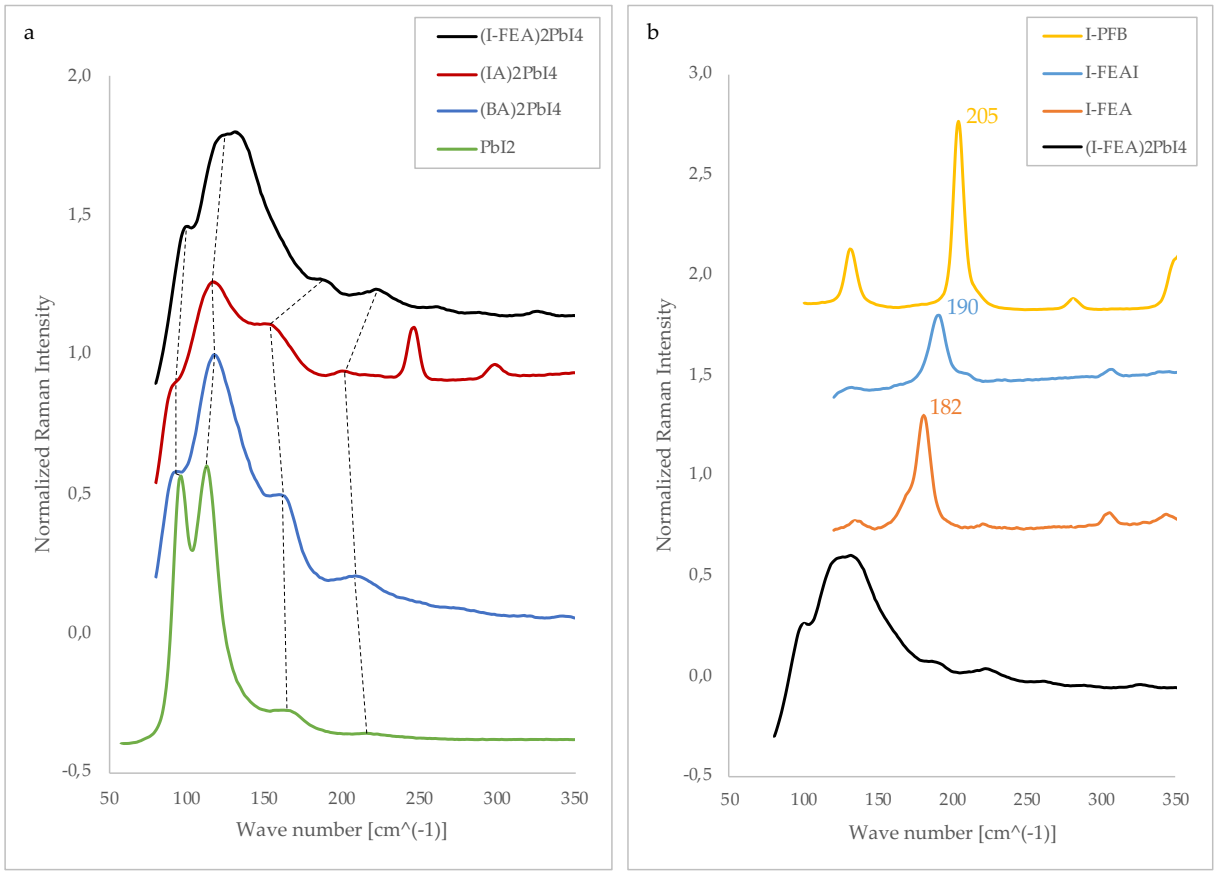

Figure 91. *Raman spectra comparison in the range 50-350 cm^{-1} among: (a) lead iodide and some 2D perovskites, matching the inorganic vibrational contributions, (b) I-PFB precursor and its derivatives, with labels onto C-I stretching bands.*

The samples were additionally characterized by solid-state NMR. ^{19}F MAS NMR, conducted onto (X-FEA)$_2$PbI$_4$, revealed two multiple peaks for each perovskite, as shown in Figure 92. The peak at less negative chemical shift was associated to the two equivalent fluorine atoms near the halogen, while the other signal was matched with the other two equivalent fluorine atoms close to the secondary amine (detailed numerical values in Table 13). Solid-state CP/MAS ^{13}C {^{1}H} NMR was also performed onto the three compounds. Peaks were all assigned (Figure 93). The fixed peaks were matched with the two carbon atoms in the alkyl chain (~45 ppm) and to the aromatic carbons **C2**, **C3** and **C4** (between 120 and 160 ppm), while aromatic **C1**, covalently bound to the halogen, was assigned to the signals subjected to a total up-field shift of

7 ppm passing from Cl (103 ppm) to Br (95 ppm) to I (96 ppm) in X-site (detailed numerical values in Table 13).

Still investigating the strength of XB interaction, solid-state CP/MAS ^{13}C $\{^{1}H\}$ NMR was conducted also onto amines and salts to compare them with the correspondent perovskites, in particular, to analyze the shift of signal related to **C1**. Solid-state ^{1}H MAS NMR experiments were also performed to completely characterize the samples. The spectra were reported for X = I in Figure 95. To help in peaks assignment, ^{13}C NMR of the three amines (X-FEA) were conducted in solution as well, giving the signals shown in Figure 96. **C1** was clearly identified in amines solution spectra, being subjected to an up-field shift, again, passing from Cl (98 ppm) to Br (84 ppm) to I (79 ppm), similarly to what found for perovskites in solid-state experiments. With this supporting information, **C1** in solid-state amine was supposed to match the signal at 62 ppm, meaning that it undergoes a down-field shift of +34 ppm passing from I-FEA amine to the correspondent perovskite and an up-field shift of -2 ppm passing from I-FEA amine to correspondent salt. The shift of **C1** (16 ppm) between I-FEA in solution and I-FEA in solid state can be explained by referring to SC-XRD analysis. The strong XB interaction formed between I and N in solid-state amine with respect to free amine in solution justifies the strong shift. Besides, **C5** and **C6** on the alkyl chain were associated to well separated peaks in the amine spectrum, while they overlap in case of salt and perovskite, probably due to the protonation of amine causing the up-field shift of **C5**. Another factor could be the conformation of the alkyl chain, which is subjected to different constraints, especially in perovskite structure.

The shift of **C1** in SS-NMR spectra could support all the other previous results (XRPD, XPS, Raman) about the presence of a strong XB interaction in $(I\text{-}FEA)_2PbI_4$ perovskite, observing the same trend (salt < amine < perovskite) of increasing XB strength. The expected trend of XB intensification by enhancing the polarizability of the halogen atom was confirmed, too. It emerged from the increasing $\Delta\delta$ between **C1** of amine and perovskites, that are 5 ppm for Cl, 11 ppm for Br and 17 ppm for I, considering solution spectra of amines, and 8 ppm for Cl, 15 ppm for Br and 34 ppm for I, considering solid-state spectra of amines.

Moreover, the exceptionally high intensity of aromatic C peaks (Figure 93), especially in $(I\text{-}FEA)_2PbI_4$, allowed to make some hypothesis about perovskite structure. Cations within the inorganic layers could behave as bidentate ligands, with the ammonium

moiety interacting with an inorganic sheet and the XB-donor group interacting through XB with the parallel inorganic sheet (Figure 94). Probably, cations are arranged in an antiparallel manner, such that one aromatic ring sees the alkyl chain of adjacent cations and receive magnetization from H. In this configuration the aromatic ring is "free" to rotate, and the system behaves as a supramolecular rotor. The enhanced rotational mobility is reflected on the intensification of NMR signals in (X-FEA)$_2$PbI$_4$ in the order Cl < Br < I, in accordance with the increasing ability of the XB-donor cations to anchor to the inorganic sublattice. If (X-FEA)$_2$PbI$_4$ was characterized by such a molecular dynamic, it would be the first study of rotors in perovskite field, opening up new research branch.

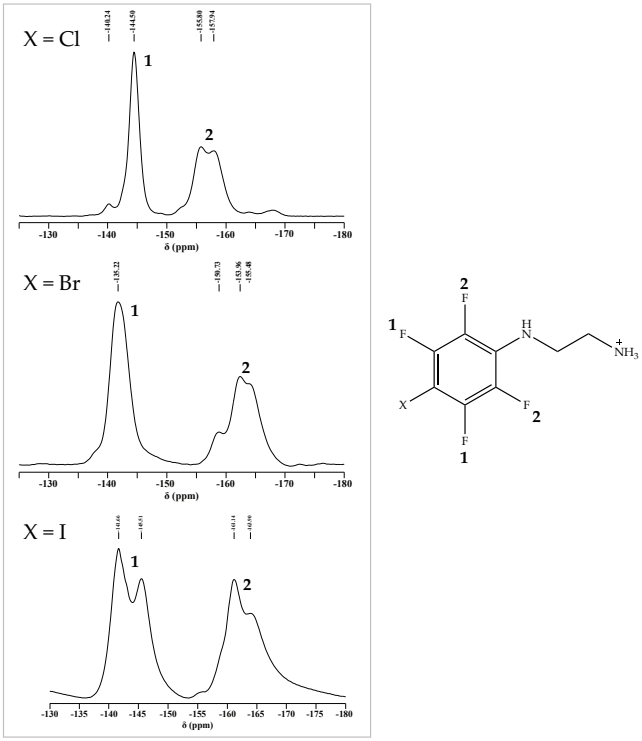

Figure 92. *Solid-state ^{19}F MAS NMR of (X-FEA)$_2$PbI$_4$, with X = Cl, Br, I.*

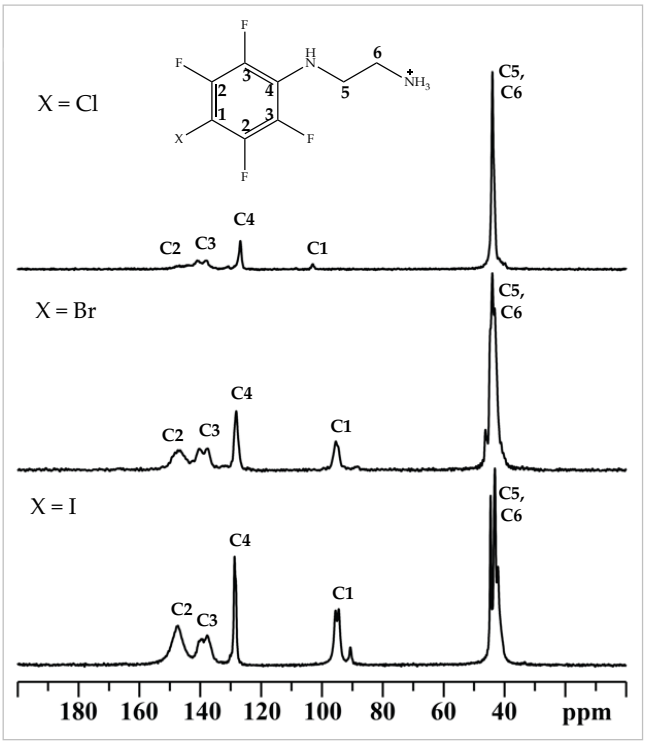

Figure 93. *Solid-state ^{13}C {^{1}H} CP/MAS NMR of (X-FEA)$_2$PbI$_4$, with X = Cl, Br, I, at contact time of 50 μs (blue) and 2ms (black) and spinning speed of 12.5 kHz.*

Table 13. *Chemical shifts in ppm for the three (X-FEA)$_2$PbI$_4$ perovskites.*

	(Cl-FEA)$_2$PbI$_4$	**(Br-FEA)$_2$PbI$_4$**	**(I-FEA)$_2$PbI$_4$**
C2	147.29, 143.96	147.20	147.35
C3	140.99, 137.99	140.35, 137.58	139.70, 137.57
C4	126.82	128.18	128.73
C1	103.03	95.45	95.54, 94.51
C5, C6	43.98	46.12, 44.73, 44.01, 43.26	44.59, 44.02, 43.18, 42.17
H1	6.92	6.53	6.61
H2	3.81	3.81	3.08
F1	-144.50	-135.22	-141.14, -145.51
F2	-155.80, -157.94	-150.73, -153.96, -155.48	-161.14, -163.90

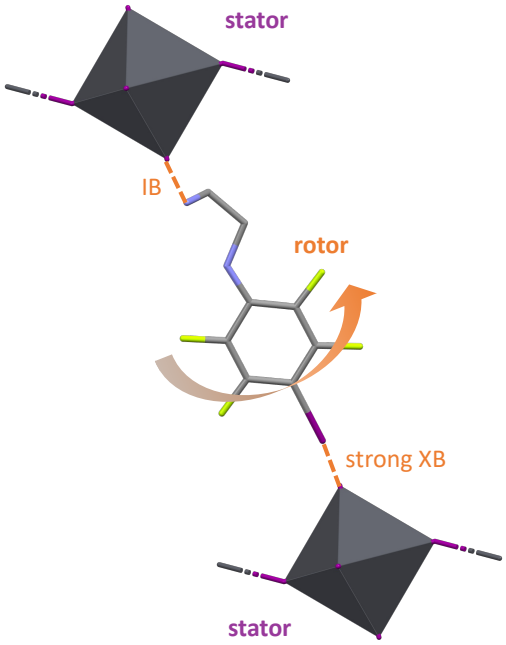

Figure 94. *Representative sketch of the hypothetical structure and molecular dynamics in (I-FEA)$_2$PbI$_4$ perovskite, that is I-FEA cations behaving as gyroscopes. H atoms are omitted for clarity.*

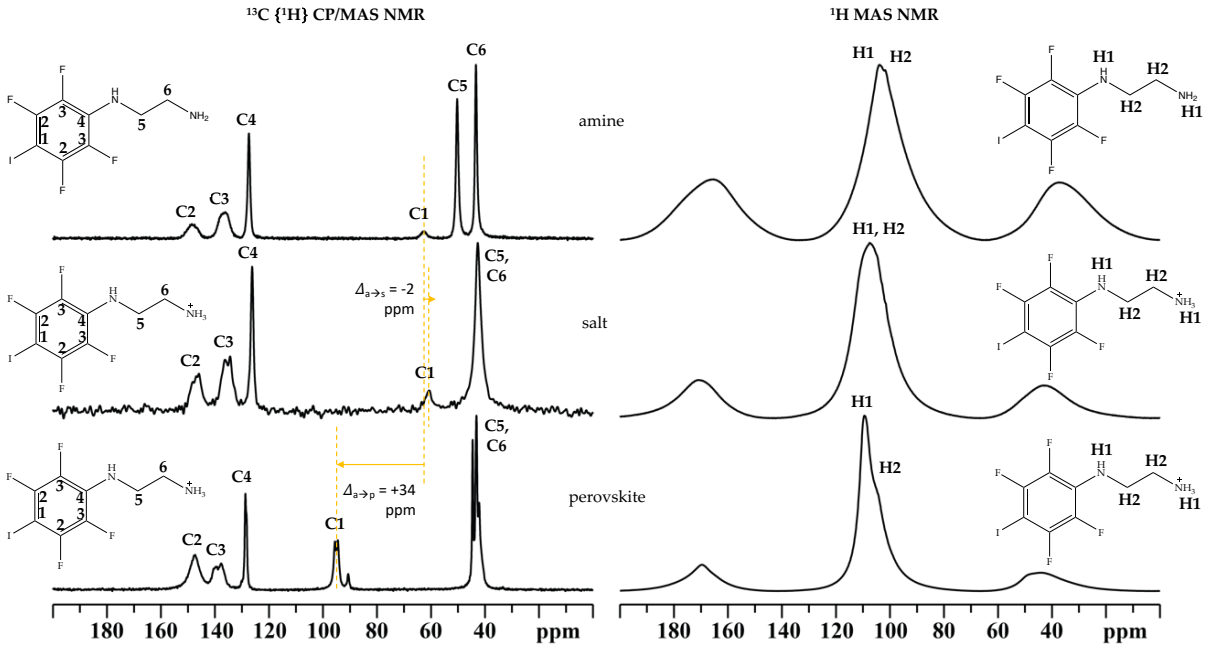

Figure 95. *Comparison among NMR spectra of amine, ammonium salt and perovskite from top down for X = I. ^{13}C {^{1}H} CP/MAS NMR spectra with ct = 2 ms on the left and ^{1}H MAS NMR spectra with ss = 12.5 kHz on the right. Chemical shifts of aromatic carbon bound to iodine atom are highlighted.*

Table 14. *Chemical shifts in ppm for the three X-FEA amines in solid state.*

	Cl-FEA	Br-FEA	I-FEA
C2	144.35	148.10, 145.39, 142.78	148.39
C3	137.95, 135.63	137.76, 135.80	136.70
C4	130.46, 128.22, 126.85	128.84	127.43
C1	94.48	80.44	62.51
C5	50.49, 48.83	49.52	50.30
C6	43.77, 42.87	43.14	43.36
H1	7.53, 5.11	4.63, 3.04	2.73
H2	3.07, 1.28	1.86	1.23

Table 15. *Chemical shifts in ppm for the three X-FEAI salts.*

	Cl-FEAI	Br-FEAI	I-FEAI
C2	146.17, 142.78	146.18	148.21, 146.96, 145.94
C3	139.96, 131.48	139.73, 136.85	136.33, 134.39
C4	128.86, 127.62	129.92, 128.64	126.23
C1	96.63	80.92	60.60
C5, C6	41.71, 39.88	40.92	42.68
H1, H2	6.18, 3.25	6.02, 3.11	5.12

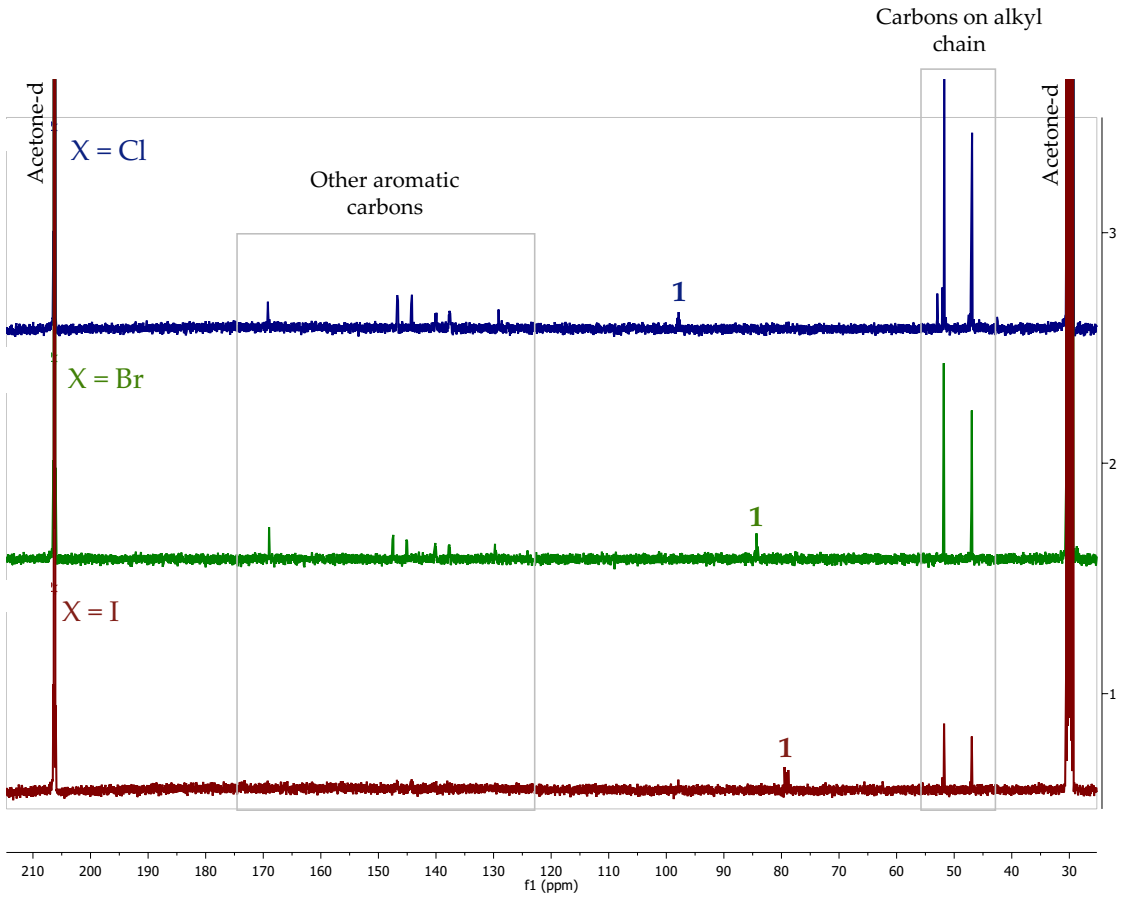

Figure 96. *^{13}C NMR spectra of X-FEA amines in acetone-d, with X = Cl, Br, I.* ***1*** *refers to carbon bound to halogen atom.*

Thinking about the possible application in optoelectronic field, optical properties were investigated, trying to correlate them with structural properties. All the synthesized 2D perovskites resulted to have a step-like absorption spectrum with a quite broad dual band emission at the edge of absorption in the range ~500-600 nm (left column of Figure 97). They represent the emission of lead iodide octahedra layers. All these dual PL bands exhibit the two components differing of ~25 nm and attributed to the different emission of surface and bulk phases.[94] Surface/subsurface regions have a wider bandgap with respect to bulk regions due to lattice distortion of lead iodide octahedra occurring in inorganic sheets in surface proximity. The two components are both present because all the experiments were operated on crystalline powder samples (thin exfoliated layers would have given only surface component)[94], with the intensity

relative to the bulk component being slightly higher than the surface one, in accordance to the fact that the incident excitation laser beam was tilted of ~60° with respect to the sample plane normal (at 90° bulk component would have strongly dominated, at 45° they would have been reversed)[94]. All the time-resolved PL spectra showed a decay measurable in the order of ps (right column of Figure 97). Energy gaps are all in the energy range 2.00-2.25 eV (Figure 98). Looking at the comparison between the different PL maximum intensities in Figure 99a, it is possible to note that, among the three perovskites with similar structure, differing only for the halogen atom, there is a trend. PL intensity increases a lot in the order Cl < Br < I, probably due to the different crystallinity of the samples or to the distortion of octahedra provided by XB interactions. Similarly, a trend in the positions of the PL peaks can be observed in the graph of Figure 99b with normalized intensities, identifying a red-shift in the order IA < I-FEA < BA < Cl-FEA < Br-FEA. The shift in PL spectrum was previously identified with the different offsets among the inorganic planes.[32] Applying the same idea to this series of 2D perovskites, and starting from the well-known $(BA)_2PbI_4$ and solved-structure $(IA)_2PbI_4$, it is possible to suppose that $(I\text{-}FEA)_2PbI_4$ has an intermediate value of offset with x = y, thus it will be comprised between (1/3,1/3) and ideal (1/2,1/2) offsets, classifying as nRP structure. Since $(Cl\text{-}FEA)_2PbI_4$ and $(Br\text{-}FEA)_2PbI_4$ are even more red-shifted than $(BA)_2PbI_4$, maybe they do not own to the diagonal of Figure 67b, but have different offsets along x and y axes.

Anomalously, steady-state PL of $(I\text{-}FEA)_2PbI_4$ presented a second band peaked at 410 nm, as shown in Figure 97i, suggesting unusual peculiarities for this sample. Considering the trinal and broad shape of the peak, and considering also that benzene has three aromatic $\pi \rightarrow \pi^*$ transitions typically presenting non-narrow bands due to the superimposition on the other molecular energy states,[95] the peak at 410 nm was hypothetically assigned to $\pi \rightarrow \pi^*$ transition within the aromatic rings in the cations. In order to confirm the nature of this component, PL of I-FEA amine was also measured and, from the comparison of the two (Figure 100), it was established that the more energetic band of $(I\text{-}FEA)_2PbI_4$ was to be attributed to the organic phase of perovskite, in particular to the electronic transition within the aromatic ring in the cations. It is anomalous that the organic phase emits at RT. It is reported in literature that PL of some 1D perovskites showed a secondary peak at higher energy, but its intensity became relevant only by cooling the temperature.[96,97] The thermochromic effect was investigated also for this 2D perovskite (Figure 101), with the confirmation that, by

cooling it down to 20K, the intensity of the two emission bands enhanced. In particular, the band at 541 nm increased by the 40% of its initial intensity, while the band at 410 nm increased by the 60% of its initial intensity. The relative intensity of the two bands at RT in graph of Figure 101 differed from previous measurements probably because of slight change in setting parameters for the experiments. The PL intensity was expected to increase upon cooling because at low temperature the vibrational relaxation of the excited state electrons to the ground state *via* non-radiative internal conversion, which is one of main fluorescence quenching mechanisms, is suppressed.[96] What happens here, only for $(I\text{-}FEA)_2PbI_4$, is that PL intensity of the band at 410 nm is already comparable with the other band at RT, suggesting that the cations are somehow constrained such that vibrational relaxation is inhibited and does not compete with radiative quenching mechanisms at RT, probably in relation to the strong organic-inorganic XB interaction. This anomalous behavior in steady-state PL matches the exceptional results from solid-state NMR for the same sample, further supporting the possibility of rotational dynamics for I-FEA cations in 2D perovskite structure.

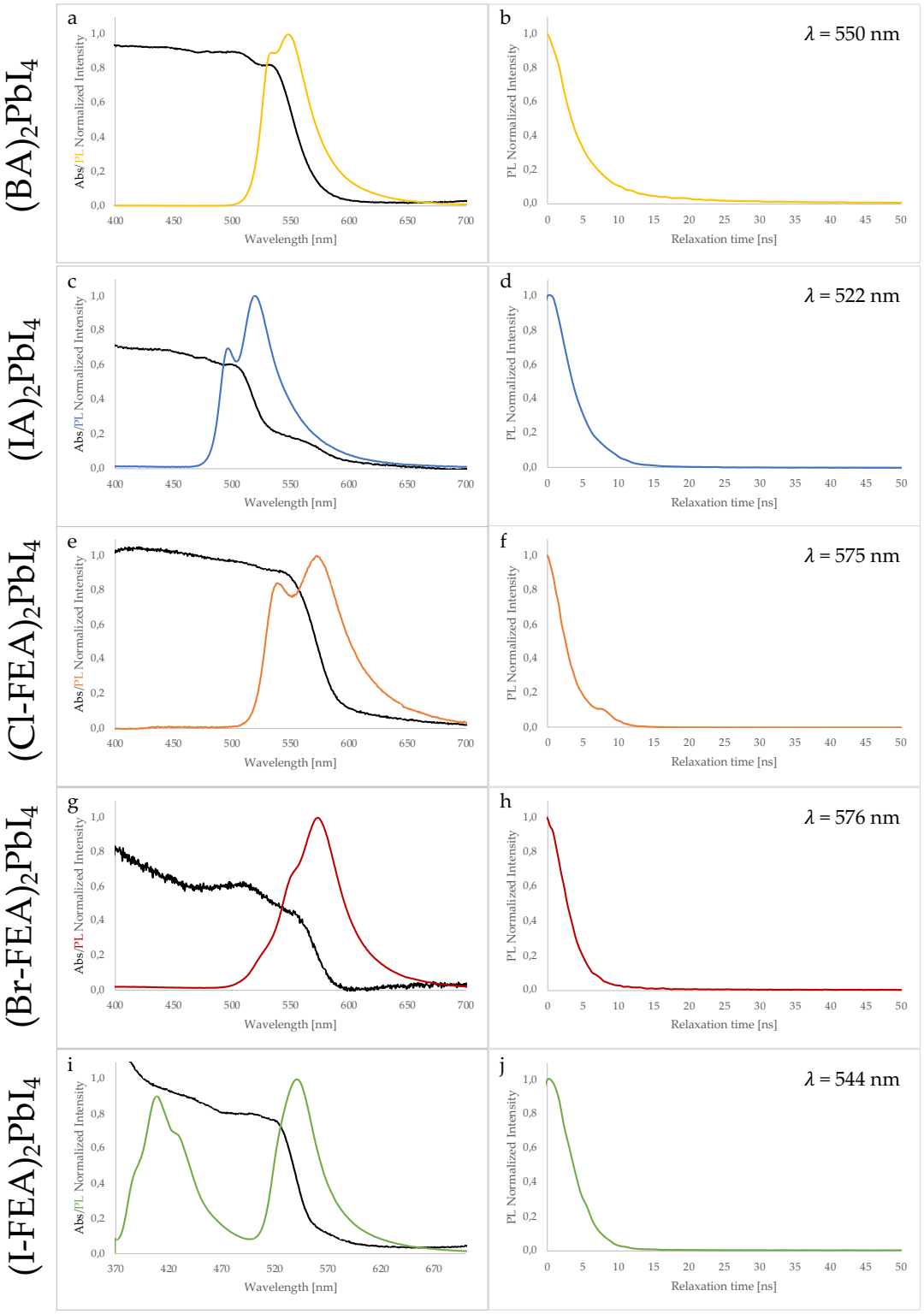

Figure 97. *Absorbance and steady-state PL measurements on the left column and time-resolved PL decay measurements at the indicated wavelength on the right column for all the synthesized 2D perovskites.*

Table 16. *Emission peaks for all the synthesized 2D perovskites at RT.*

	Wavelength [nm]				
	Dual band components		Trinal band components		
$(BA)_2PbI_4$	550	532	-	-	-
$(IA)_2PbI_4$	522	496	-	-	-
$(Cl\text{-}FEA)_2PbI_4$	575	539	-	-	-
$(Br\text{-}FEA)_2PbI_4$	576	552	-	-	-
$(I\text{-}FEA)_2PbI_4$	544	525	430	410	388

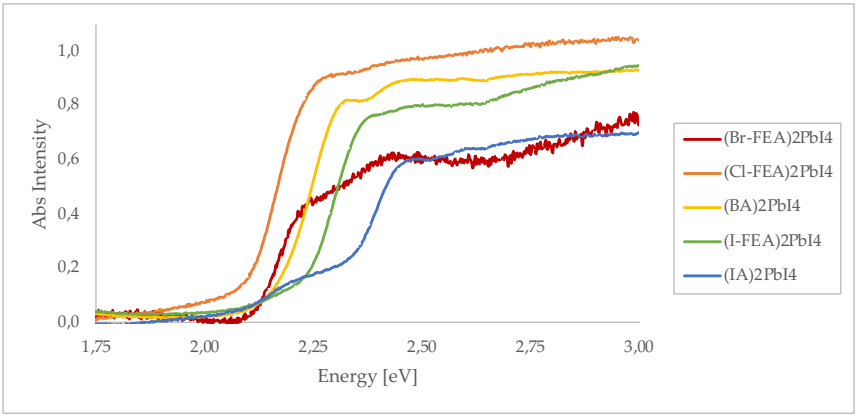

Figure 98. *Absorption spectra for all the synthesized 2D perovskites.*

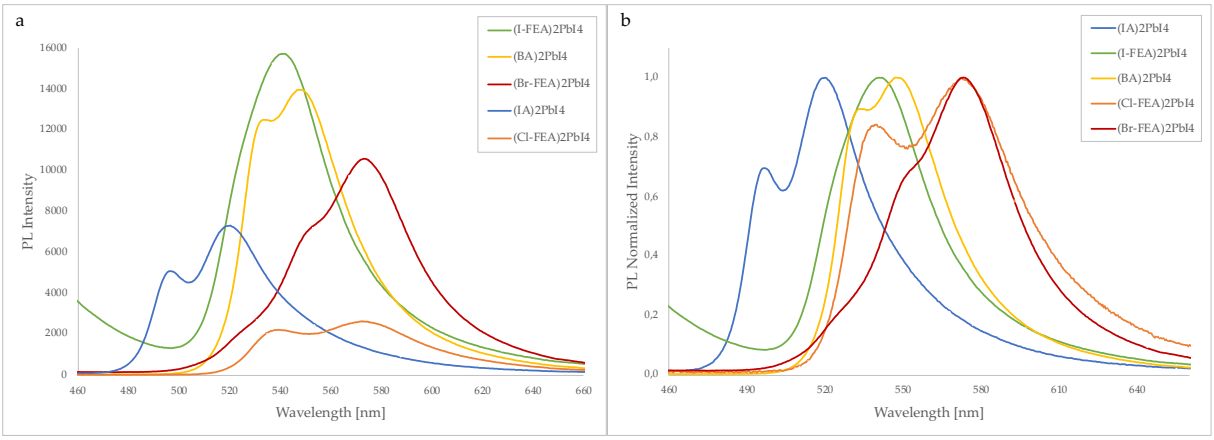

Figure 99. *(a) Steady-state PL measurements - with normalized intensity in (b) – in the wavelength range 460-660 nm for all the synthesized 2D perovskites.*

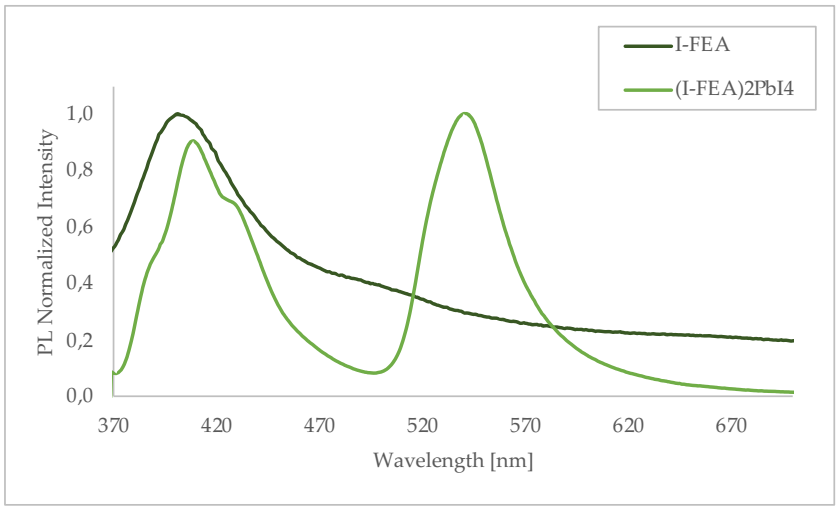

Figure 100. *Steady-state PL measurements of $(I\text{-}FEA)_2PbI_4$ perovskite and I-FEA amine at RT.*

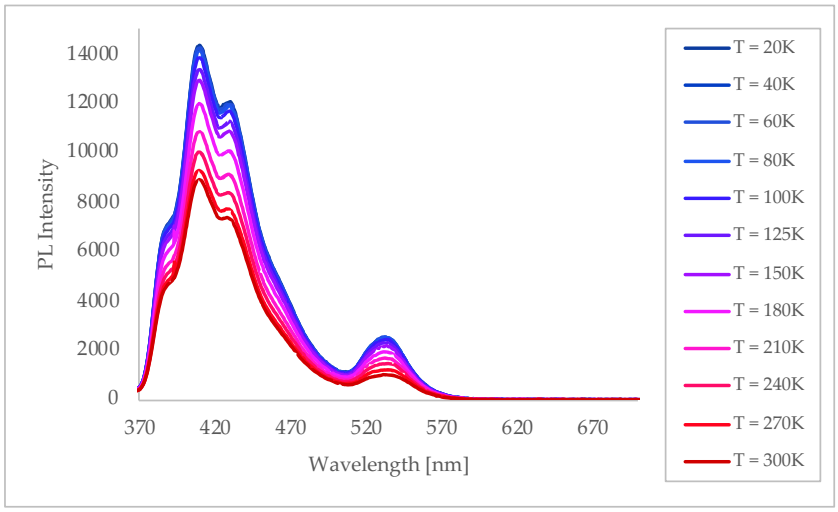

Figure 101. *Thermochromic effect measured on $(I\text{-}FEA)_2PbI_4$.*

5. Materials and Methods

5.1 Synthesis

5.1.1 Amines

***N*-(4-iodo-2,3,5,6-tetrafluoro)-ethylenediamine, I-FEA.** A mixture of 0.80 mL of ethylendiamine and 0.96 mL of iodo-pentafluorobenzene (I-PFB) was stirred at RT. After 24 hours a white sticky compound was obtained.

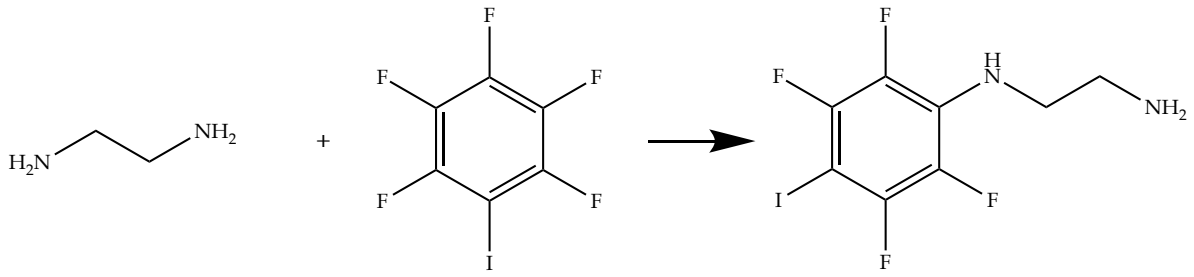

Figure 102. *Schematic representation of reaction for I-TFA synthesis.*

Table 17. *Recap of reaction details.*

	Reagents		**Product (theoretical)**
Formula	$NH_2(CH_2)_2NH_2$	C_6IF_5	$C_6IF_4NH(CH_2)_2NH_2$
PM [g/mol]	60.100	353.960	334.054
ρ [g/mL]	0.900	2.204	-
n [mmol]	11.974	5.987	5.987
eq	2.000	1.000	1.000
V [mL]	0.80	0.96	-
m [mg]	-	-	2 000.000

Purification. The product was separated from ethylendiamine in excess by extractions with water and chloroform. The organic solution was dehydrated with sodium sulfate, then filtered on Büchner and dried with rotovap. Chromatography column was used to purify from unreacted I-PFB detected by TLC. After total impurity elution by dichloromethane, the solvent polarity was increased (dichloromethane/methanol 3:2) and the isolated product was recovered. After drying with rotovap, ^{19}F NMR spectrum presented some impurity peaks. Thus, the sample was washed with hexane, filtered on Büchner and dried with rotovap. A white solid powder was obtained.

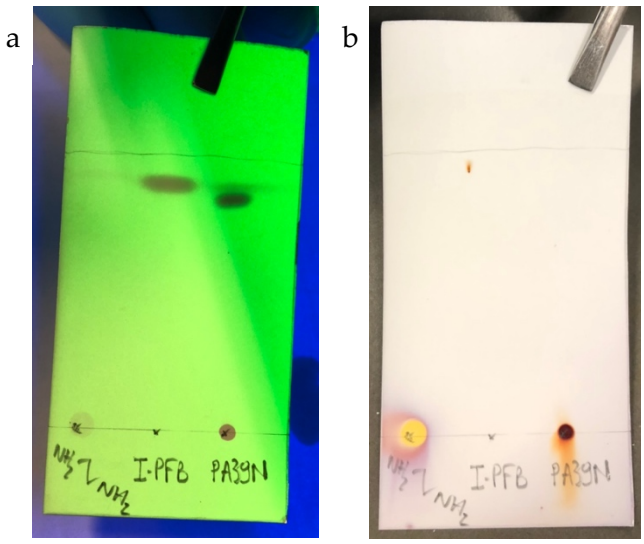

Figure 103. *TLC before chromatography column. From left to right the two reagent and the product are spotted. (a) Development under UV light exposure. (b) Development after dipping in ninhydrin and heating at 200°C.*

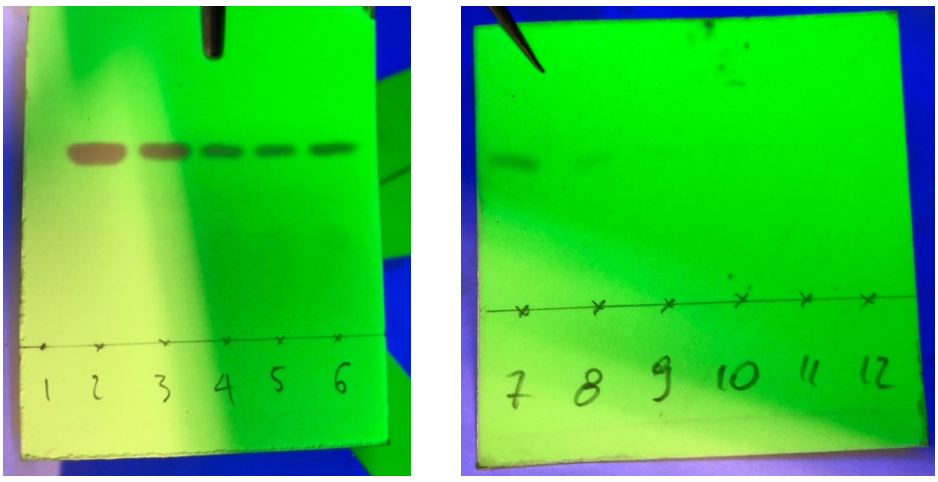

Figure 104. *TLC development under UV exposure after impurity elution in chromatography column with dichloromethane.*

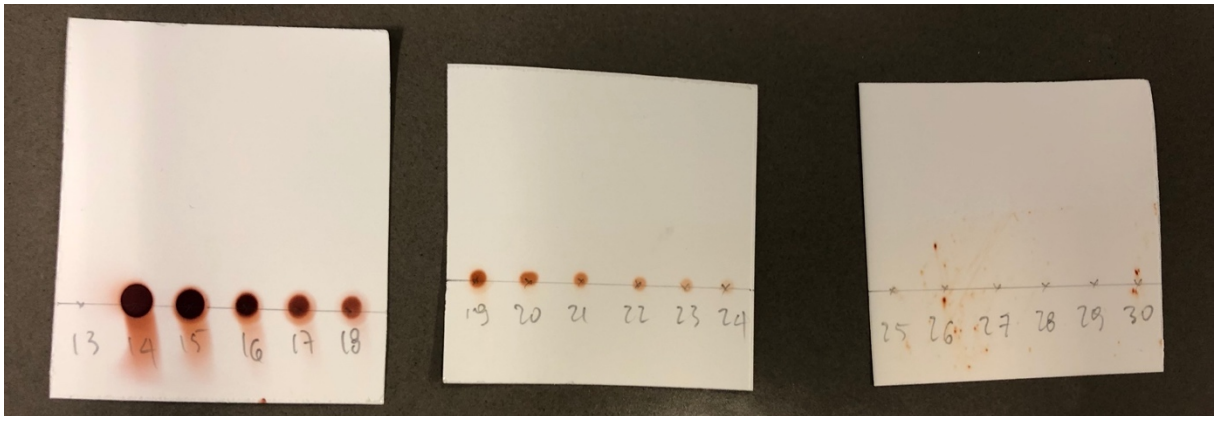

Figure 105. *TLC development in ninhydrin after amine elution in chromatography column with dichloromethane/methanol solution.*

Table 18. *Yield for Br-FEA calculated as expected/measured mass percentage ratio.*

Measured mass [mg]	Expected mass [mg]	Yield [%]
1 150.97	2 000.00	57.55

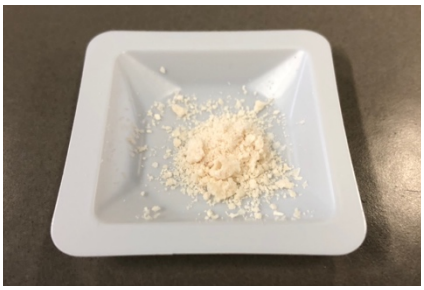

Figure 106. *Photo of I-FEA after purification.*

***N*-(4-bromo-2,3,5,6-tetrafluoro)-ethylenediamine, Br-FEA.** A mixture of 0.93 mL of ethylendiamine and 0.88 mL of bromo-pentafluorobenzene (Br-PFB) was stirred at RT. After 24 hours a white sticky compound was obtained.

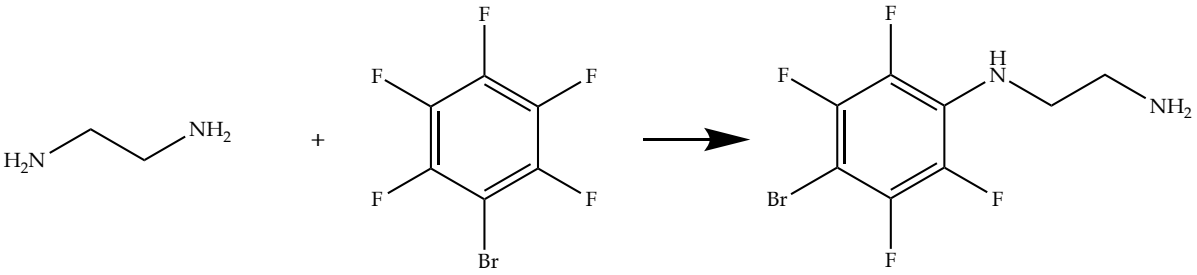

Figure 107. *Schematic representation of reaction for Br-TFA synthesis.*

Table 19. *Recap of reaction details.*

	Reagents		**Product (theoretical)**
Formula	$NH_2(CH_2)_2NH_2$	C_6BrF_5	$C_6BrF_4NH(CH_2)_2NH_2$
PM [g/mol]	60.100	246.960	287.054
ρ [g/mL]	0.900	1.950	-
n [mmol]	13.935	6.967	6.967
eq	2.000	1.000	1.000
V [mL]	0.93	0.88	-
m [mg]	-	-	2 000.000

Purification. The product was separated from ethylendiamine in excess by extractions with water and chloroform. The organic solution was dehydrated with sodium sulfate, then filtered on Büchner and dried with rotovap. Chromatography column was used to purify from unreacted Br-PFB detected by TLC. After total impurity elution by

dichloromethane, the solvent polarity was increased (dichloromethane/methanol 3:2) and the isolated product was recovered. After drying with rotovap, ^{19}F NMR spectrum presented some impurity peaks. Thus, the sample was washed with hexane, filtered on Büchner and dried with rotovap. A white solid powder was obtained as shown in Figure 108.

Table 20. *Yield for Br-FEA calculated as expected/measured mass percentage ratio.*

Measured mass [mg]	Expected mass [mg]	Yield [%]
1 292.39	2 000.00	64.61

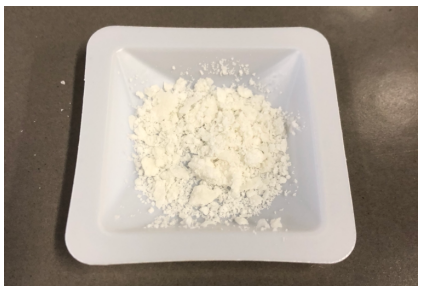

Figure 108. *Photo of Br-FEA after purification.*

***N*-(4-chloro-2,3,5,6-tetrafluoro)-ethylenediamine, Cl-FEA.** A mixture of 1.10 mL of ethylendiamine and 1.06 mL of chloro-pentafluorobenzene (Cl-PFB) was stirred at RT. After 24 hours a white sticky compound was obtained.

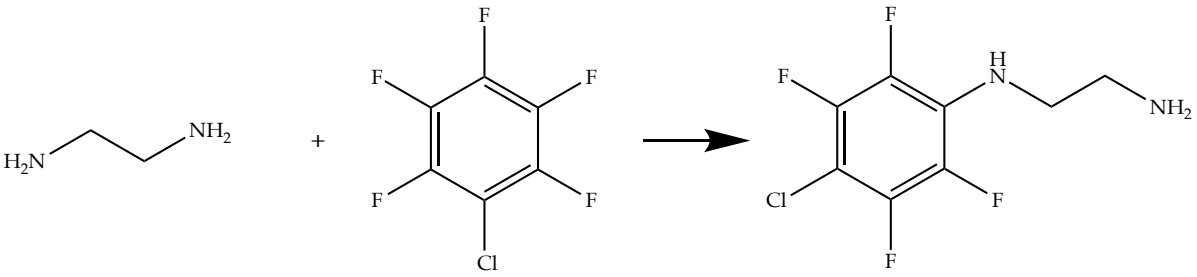

Figure 109. *Schematic representation of reaction for Cl-TFA synthesis.*

Table 21. *Recap of reaction details.*

	Reagents		**Product (theoretical)**
Formula	$NH_2(CH_2)_2NH_2$	C_6ClF_5	$C_6ClF_4NH(CH_2)_2NH_2$
PM [g/mol]	60.100	202.509	242.603
ρ [g/mL]	0.900	1.568	-
n [mmol]	16.488	8.244	8.244
eq	2.000	1.000	1.000
V [mL]	1.10	1.07	-
m [mg]	-	-	2 000.000

Purification. The product was separated from ethylendiamine in excess by extractions with water and chloroform. The organic solution was dehydrated with sodium sulfate, then filtered on Büchner and dried with rotovap. Chromatography column was used to purify from unreacted Cl-PFB detected by TLC. After total impurity elution by dichloromethane, the solvent polarity was increased (dichloromethane/methanol 3:2 V/V) and the isolated product was recovered. After drying with rotovap, ^{19}F NMR spectrum presented some impurity peaks. Thus, the sample was washed with hexane, filtered on Büchner and dried with rotovap. A white solid powder was obtained as shown in Figure 110.

Table 22. *Yield for purified Cl-FEA calculated as expected/measured mass percentage ratio.*

Measured mass [mg]	Expected mass [mg]	Yield [%]
1 324.33	2 000.00	66.22

Figure 110. *Photo of Cl-FEA after purification.*

5.1.2 Ammonium Salts

Benzylammonium Iodide, BAI. An excess of hydrogen iodide (HI) water-based solution (57% wt.) was added to 0.6 mL of benzylamine (BA) to favor the acid-base reaction. The precipitated solid product was washed with diethyl ether, filtered on Büchner (washed several times also on the filter) to eliminate the excess of acid and dried under vacuum. White crystalline flakes were obtained as shown in Figure 112.

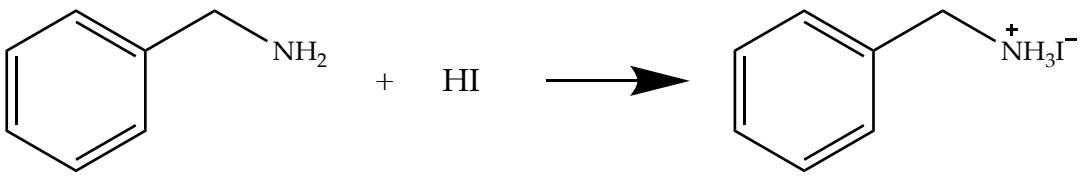

Figure 111. *Schematic representation of reaction for BAI synthesis.*

Table 23. *Recap of reaction details.*

	Reagents		Product (theoretical)
Formula	$C_6H_5CH_2NH_2$	HI	$(C_6H_5CH_2NH_3)I$
PM [g/mol]	107.156	127.912	235.068
ρ [g/mL]	0.981	1.701	-
n [mmol]	5.493	15.160	5.493
eq	1.000	2.760	1.000
V [mL]	0.60	2.00	-
m [mg]	-	-	1 291.229

Table 24. *Yield for washed BAI calculated as expected/measured mass percentage ratio.*

Measured mass [mg]	Expected mass [mg]	Yield [%]
494.44	1 291.23	38.29

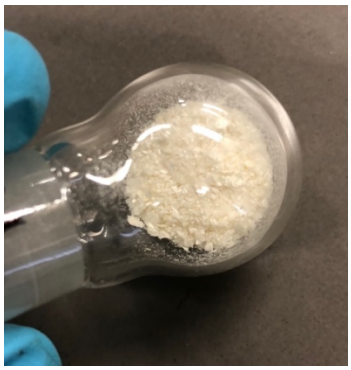

Figure 112. *Photo of BAI after cleaning.*

4-Iodoanilinium Iodide, IAI. 300 mg of IA were dissolved in a minimum of methanol (0.5 mL) and the stoichiometric amount of hydrogen iodide (HI) (water-based solution, 57% wt.) was added into the same flask. The precipitated solid product was washed with diethyl ether, filtered on Büchner (washed several times also on the filter) to

eliminate the excess of acid and dried under vacuum. Grey/violet crystalline powder was obtained as shown in Figure 114.

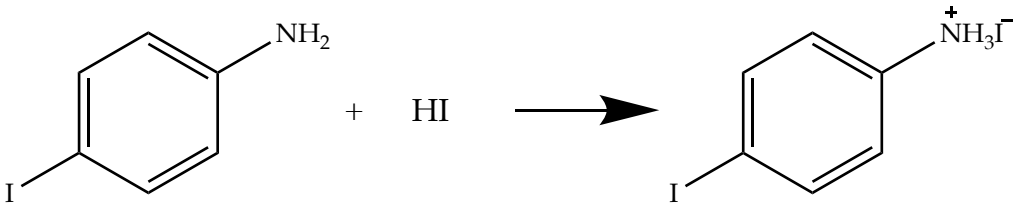

Figure 113. *Schematic representation of reaction for IAI synthesis.*

Table 25. *Recap of reaction details.*

	Reagents		**Product (theoretical)**
Formula	$IC_6H_4NH_2$	HI	$(IC_6H_4NH_3)I$
PM [g/mol]	219.025	127.912	346.937
ρ [g/mL]	-	1.701	-
n [mmol]	1.370	3.790	1.370
eq	1.000	2.766	1.000
V [mL]	-	0.50	-
m [mg]	300.04	-	475.304

Table 26. *Yield for washed IAI calculated as expected/measured mass percentage ratio.*

Measured mass [mg]	**Expected mass [mg]**	**Yield [%]**
263.92	475.30	55.53

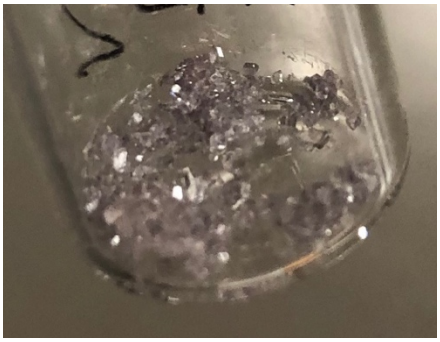

Figure 114. *Photo of IAI after cleaning.*

(4-Iodo-2,3,5,6-tetrafluoroaniline)-ethan-1-ammonium Iodide, I-FEAI. 219 mg of I-FEA were dissolved in a minimum of methanol (0.5 mL) and the stoichiometric amount of hydrogen iodide (HI) (water-based solution, 57% wt.) was added into the same flask, in order to protonate only the primary amine. The precipitated solid product was washed with diethyl ether, filtered on Büchner (washed several times also on the filter) to eliminate the excess of acid and dried under vacuum. A white powder was obtained.

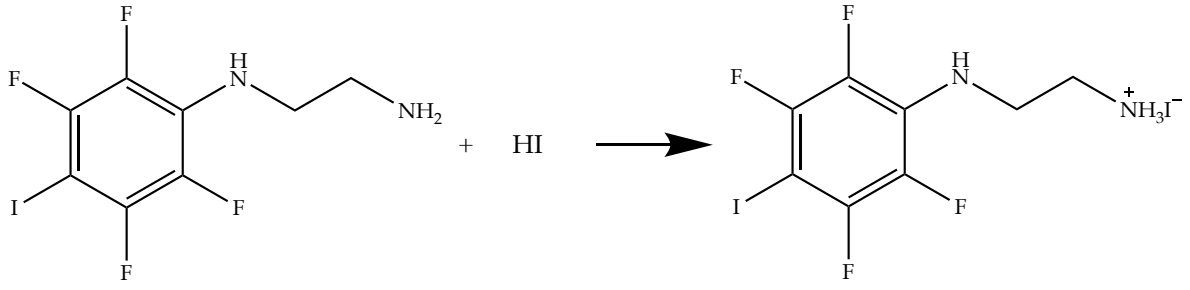

Figure 115. *Schematic representation of reaction for I-FEAI synthesis.*

Table 27. *Recap of reaction details.*

	Reagents		**Product (theoretical)**
Formula	$C_6IF_4NH(CH_2)_2NH_2$	HI	$(C_6IF_4NH(CH_2)_2NH_3)I$
PM [g/mol]	334.054	127.912	461.966
ρ [g/mL]	-	1.701	-
n [mmol]	0.658	0.658	0.658
eq	1.000	1.000	1.000
V [mL]	-	0.050	-
m [mg]	219.73	-	303.974

Table 28. *Yield for washed I-FEAI calculated as expected/measured mass percentage ratio.*

Measured mass [mg]	**Expected mass [mg]**	**Yield [%]**
183.68	303.97	60.43

(4-Bromo-2,3,5,6-tetrafluoroaniline)-ethan-1-ammonium Iodide, Br-FEAI. 208 mg of Br-FEA were dissolved in a minimum of methanol (0.5 mL) and the stoichiometric amount of hydrogen iodide (HI) (water-based solution, 57% wt.) was added into the same flask, in order to protonate only the primary amine. The precipitated solid product was washed with diethyl ether, filtered on Büchner (washed several times also on the filter) to eliminate the excess of acid and dried under vacuum. A white powder was obtained.

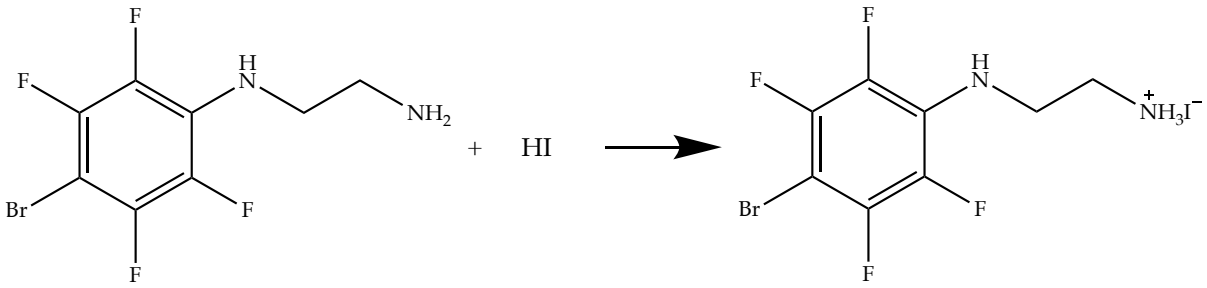

Figure 116. *Schematic representation of reaction for Br-FEAI synthesis.*

Table 29. *Recap of reaction details.*

	Reagents		**Product (theoretical)**
Formula	$C_6BrF_4NH(CH_2)_2NH_2$	HI	$(C_6BrF_4NH(CH_2)_2NH_3)I$
PM [g/mol]	287.054	127.912	414.966
ρ [g/mL]	-	1.701	-
n [mmol]	0.723	0.723	0.723
eq	1.000	1.000	1.000
V [mL]	-	0.10	-
m [mg]	207.50	-	300.020

Table 30. *Yield for washed Br-FEAI calculated as expected/measured mass percentage ratio.*

Measured mass [mg]	**Expected mass [mg]**	**Yield [%]**
215.87	300.02	71.95

(4-Chloro-2,3,5,6-tetrafluoroaniline)-ethan-1-ammonium Iodide, Cl-FEAI 345 mg of Cl-FEA were dissolved in a minimum of methanol (0.5 mL) and the stoichiometric amount of hydrogen iodide (HI) (water-based solution, 57% wt.) was added into the same flask, in order to protonate only the primary amine. The precipitated solid product was washed with diethyl ether, filtered on Büchner (washed several times also on the filter) to eliminate the excess of acid and dried under vacuum. A white powder was obtained.

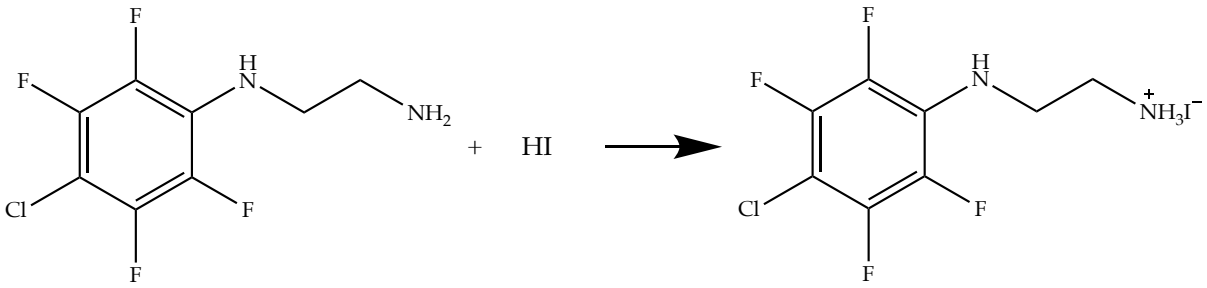

Figure 117. *Schematic representation of reaction for Cl-FEAI synthesis.*

Table 31. *Recap of reaction details.*

	Reagents		**Product (theoretical)**
Formula	$C_6ClF_4NH(CH_2)_2NH_2$	HI	$(C_6ClF_4NH(CH_2)_2NH_3)I$
PM [g/mol]	242.603	127.912	323.515
ρ [g/mL]	-	1.701	-
n [mmol]	1.424	1.424	1.424
eq	1.000	1.000	1.000
V [mL]	-	0.19	-
m [mg]	345.45	-	460.685

Table 32. *Yield for washed Cl-FEAI calculated as expected/measured mass percentage ratio.*

Measured mass [mg]	Expected mass [mg]	Yield [%]
267.21	460.69	58.00

5.1.3 Perovskites

Bis(benzylammonium) Tetraiodoplumbate, $(BA)_2PbI_4$. 260 mg of PbI_2 were dissolved in excess of HI (water-based solution, 57% wt.) and stirred up to 100°C in N_2 atmosphere. 0.26 mL of BA were injected in the same flask of the hot solution, and the resultant mixture was stirred at reflux for 45'. The solution was then allowed to crystallize by slowly cooling down to RT. The precipitated dark solids were washed with diethyl ether, filtered on Büchner (washed several times also on the filter) and dried under vacuum. Light orange powder was obtained as shown in Figure 119d.

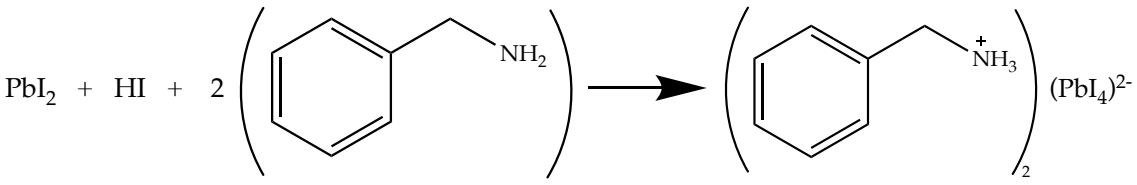

Figure 118. *Schematic representation of reaction for $(BA)_2PbI_4$ synthesis.*

Table 33. *Recap of reaction details.*

	Reagents			Product (theoretical)
Formula	PbI_2	HI	$C_6H_5CH_2NH_2$	$(C_6H_5CH_2NH_3)_2PbI_4$
PM [g/mol]	334.104	127.912	107.156	931.144
ρ [g/mL]	-	1.701	0.981	-

n [mmol]	0.780	22.740	2.338	0.780
eq	1.000	29.154	3.000	1.000
V [mL]	-	3.00	0.26	-
m [mg]	260.43	-	-	726.292

Table 34. *Yield for washed $(BA)_2PbI_4$ calculated as expected/measured mass percentage ratio.*

Measured mass [mg]	Expected mass [mg]	Yield [%]
561.12	726.29	77.26

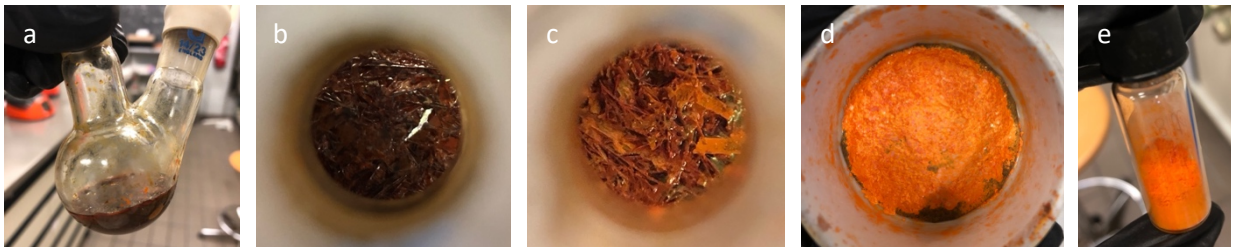

Figure 119. *$(BA)_2PbI_4$ (a) and (b) in the flask before cleaning, (c) in the flask after washing with diethyl ether, (d) on the filter after washing several times, (e) in the vial after drying.*

Bis(4-iodoanilinium) Tetraiodoplumbate, $(IA)_2PbI_4$. 298 mg of PbI_2 were dissolved in excess of HI (water-based solution, 57% wt.) and stirred up to 100°C in N_2 atmosphere. 585 mg of IA dissolved in a minimum of methanol were injected in the same flask of the hot solution, and the resultant mixture was stirred at reflux for 45'. The solution was then allowed to crystallize by slowly cooling down to RT. The precipitated dark solids were washed with diethyl ether, filtered on Büchner (washed several times also on the filter) and dried under vacuum. Yellow ochre powder was obtained as shown in Figure 121.

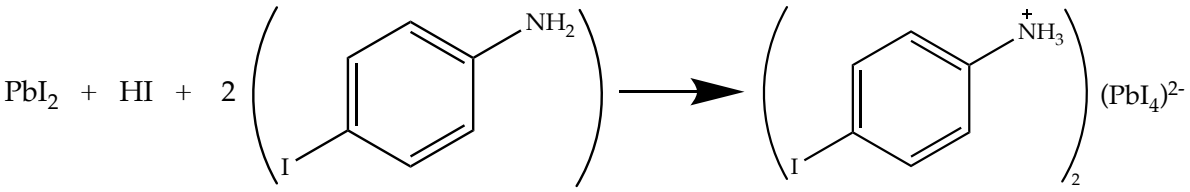

Figure 120. *Schematic representation of reaction for $(IA)_2PbI_4$ synthesis.*

Table 35. *Recap of reaction details.*

	Reagents			**Product (theoretical)**
Formula	PbI_2	HI	$IC_6H_4NH_2$	$(IC_6H_4NH_3)_2PbI_4$
PM [g/mol]	334.104	127.912	219.025	1 154.882
ρ [g/mL]	-	1.701	-	-
n [mmol]	0.891	22.740	2.673	0.891
eq	1.000	25.522	3.000	1.000
V [mL]	-	3.00	-	-
m [mg]	297.69	-	585.45	1 029.000

Table 36. *Yield for washed $(IA)_2PbI_4$ calculated as expected/measured mass percentage ratio.*

Measured mass [mg]	**Expected mass [mg]**	**Yield [%]**
561.12	1 029.00	77.26

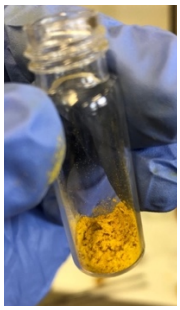

Figure 121. *Photo of $(IA)_2PbI_4$ after cleaning.*

Bis((4-iodo-2,3,5,6-tetrafluoroaniline)-ethan-1-ammonium) Tetraiodoplumbate, $(I\text{-}FEA)_2PbI_4$. 260 mg of PbI_2 were dissolved in excess of HI (water-based solution, 57% wt.) and stirred up to 100°C in N_2 atmosphere. 780 mg of I-FEA dissolved in a minimum of methanol were injected in the same flask of the hot solution, and the resultant mixture was stirred at reflux for 45'. The solution was then allowed to crystallize by slowly cooling down to RT. The precipitated dark solids were washed with diethyl ether, filtered on Büchner (washed several times also on the filter) and dried under vacuum. Bright crystalline orange powder was obtained as shown in Figure 123.

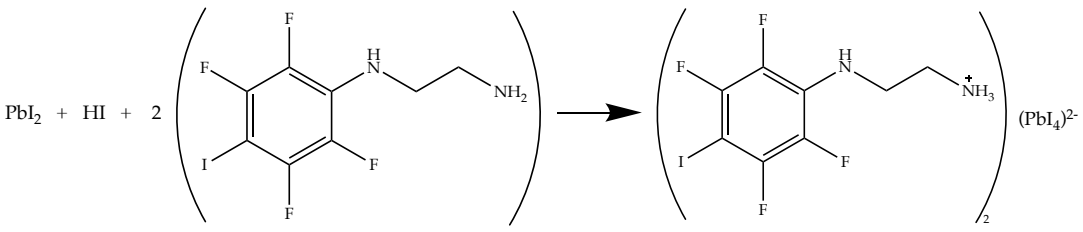

Figure 122. *Schematic representation of reaction for $(I\text{-}FEA)_2PbI_4$ synthesis.*

Table 37. *Recap of reaction details.*

	Reagents			Product (theoretical)
Formula	PbI_2	HI	$C_6IF_4NH(CH_2)_2NH_2$	$(C_6IF_4NH(CH_2)_2NH_3)_2PbI_4$
PM [g/mol]	334.104	127.912	334.054	1 384.940
ρ [g/mL]	-	1.701	-	-
n [mmol]	0.779	22.740	2.336	0.779
eq	1.000	29.191	3.000	1.000
V [mL]	-	3.00	-	-
m [mg]	260.21	-	780.350	1 078.868

Table 38. *Yield for washed $(I\text{-}FEA)_2PbI_4$ calculated as expected/measured mass percentage ratio.*

Measured mass [mg]	Expected mass [mg]	Yield [%]
565.65	1 078.87	52.43

Figure 123. *Photo of $(I\text{-}FEA)_2PbI_4$ after cleaning.*

Bis((4-bromo-2,3,5,6-tetrafluoroaniline)-ethan-1-ammonium) Tetraiodoplumbate, $(Br\text{-}FEA)_2PbI_4$. 180 mg of PbI_2 were dissolved in excess of HI (water-based solution, 57% wt.) and stirred up to 100°C in N_2 atmosphere. 464 mg of Br-FEA dissolved in a

minimum of methanol were injected in the same flask of the hot solution, and the resultant mixture was stirred at reflux for 45'. The solution was then allowed to crystallize by slowly cooling down to RT. The precipitated dark solids were washed with diethyl ether, filtered on Büchner (washed several times also on the filter) and dried under vacuum. Bright crystalline red/orange powder was obtained as shown in Figure 125.

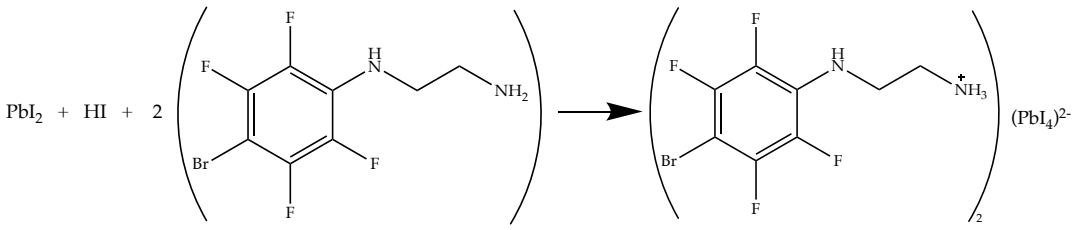

Figure 124. *Schematic representation of reaction for (Br-FEA)$_2$PbI$_4$ synthesis.*

Table 39. *Recap of reaction details.*

	Reagents			**Product (theoretical)**
Formula	PbI_2	HI	$C_6BrF_4NH(CH_2)_2NH_2$	$(C_6BrF_4NH(CH_2)_2NH_3)_2PbI_4$
PM [g/mol]	334.104	127.912	287.054	1 290.94
ρ [g/mL]	-	1.701	-	-
n [mmol]	0.539	15.160	1.617	0.539
eq	1.000	28.126	3.000	1.000
V [mL]	-	2.00	-	-
m [mg]	180.12	-	464.166	695.817

Table 40. *Yield for washed (Br-FEA)$_2$PbI$_4$ calculated as expected/measured mass percentage ratio.*

Measured mass [mg]	Expected mass [mg]	Yield [%]
451.98	695.81	64.96

Figure 125. *Photo of (Br-FEA)$_2$PbI$_4$ after cleaning.*

Bis((4-chloro-2,3,5,6-tetrafluoroaniline)-ethan-1-ammonium) Tetraiodoplumbate, (Cl-FEA)$_2$PbI$_4$. mg of PbI_2 were dissolved in excess of HI (water-based solution, 57% wt.) and stirred up to 100°C in N_2 atmosphere. mg of Cl-FEA dissolved in a minimum of methanol were injected in the same flask of the hot solution, and the resultant mixture was stirred at reflux for 45'. The solution was then allowed to crystallize by slowly cooling down to RT. The precipitated dark solids were washed with diethyl ether, filtered on Büchner (washed several times also on the filter) and dried under vacuum. Bright crystalline red/orange powder was obtained as shown in Figure 127.

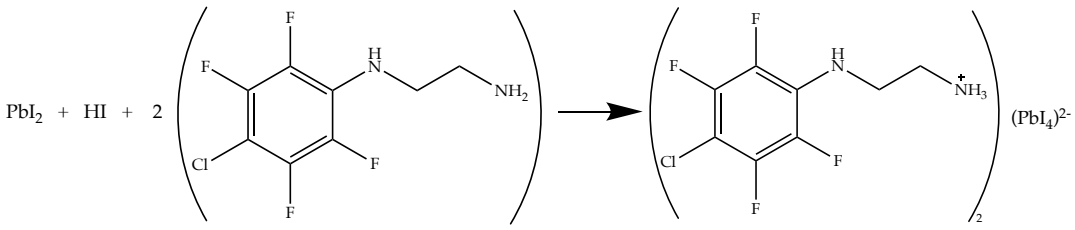

Figure 126. *Schematic representation of reaction for (Cl-FEA)$_2$PbI$_4$ synthesis.*

Table 41. *Recap of reaction details.*

	Reagents			**Product (theoretical)**
Formula	PbI_2	HI	$C_6ClF_4NH(CH_2)_2NH_2$	$(C_6ClF_4NH(CH_2)_2NH_3)_2PbI_4$
PM [g/mol]	334.104	127.912	242.603	1 202.038
ρ [g/mL]	-	1.701	-	-
n [mmol]	0.539	22.740	1.617	0.539
eq	1.000	42.189	3.000	1.000
V [mL]	-	3.00	-	-
m [mg]	180.08	-	392.289	647.898

Table 42. *Yield for washed (Cl-FEA)$_2$PbI$_4$ calculated as expected/measured mass percentage ratio.*

Measured mass [mg]	**Expected mass [mg]**	**Yield [%]**
378.21	647.90	58.37

Figure 127. *Photo of (Cl-FEA)$_2$PbI$_4$ after cleaning.*

5.1.4 Single Crystals

General methods. Single crystals of amines formed spontaneously during slow drying in rotovap, before obtaining powder after complete drying (Figure 128a). Single crystals of salts formed at initial steps of slower precipitation in more diluted methanol-based precursor solution. Perovskites single crystals were obtained through slow diffusion crystallization method. PbI_2 was dissolved in a large excess of HI. In the same vial a minimum of methanol was added such to form a thin interlayer and, as third layer, the amine (small excess) dissolved in methanol was slowly added (Figure 128b). After a couple of days at RT single crystals precipitated (Figure 128d) and were eventually washed in diethyl ether (Figure 128c).

Figure 128. *(a) Photo of single crystals of I-FEA. (b) Photo of layered solution prepared for precipitation of single crystals of $(IA)_2PbI_4$. (c) Photo of single crystals of $(BA)_2PbI_4$, washed in diethyl ether. (d) Photo of single crystals of $(IA)_2PbI_4$ formed at the vial walls.*

5.2 Characterization

5.2.1 Thin Layer Chromatography (TLC)

TLC was used to qualitative verify the purity of amines before and after Chromatography column. The solution samples were spotted on Silica gel F_{254}, the thin absorber material layer representing the stationary phase, coated onto aluminum sheet substrate. The mobile phase was represented by the samples dissolved in dichloromethane or chloroform. TLC plate was developed under exposure to UV lamp (λ = 254 nm) to detect aromatic species and/or by dipping into ninhydrin solution (ethanol-based) to detect aminic groups.

5.2.2 Nuclear Magnetic Resonance (NMR)

Brucker Avance III Nanobay 400 MHz and Brucker TopSpin 3.2 were used as instrument and software, respectively, for NMR analysis of samples in solution. Three types of experiments were done: ^{1}H NMR, ^{19}F NMR and ^{13}C NMR. Experiments details are provided in Table 43. MestReNova was adopted for elaboration of data, with the eventual help of simulations by Chemdraw.

Table 43. *NMR experiments parameters.*

	^{1}H NMR	**^{19}F NMR**	**^{13}C NMR**
Solvent	MeOD	MeOD	Acetone-d6
Size of fid	65 536	562 480	65 536
Temperature [K]	302	305	302
Number of scans	80	8	3072
Relaxation delay [s]	1	2	2
Spectral width [ppm]	20.0254	398.448	238.897
Transmitter frequency offset [ppm]	6.175	-100	99.995

5.2.3 Solid-State Nuclear Magnetic Resonance (SS-NMR)

Solid-state NMR experiments were performed using a Bruker Avance Neo 500 MHz with a rotor of 4 mm and a spinning speed of 12.5 kHz. ^{13}C {^{1}H} CP MAS (Cross-Polarization Magic Angle Spinning) NMR spectra were collected at various contact times between 50 μs and 7 ms. ^{13}C {^{19}F} CP MAS NMR spectra were collected at contact times of 50 μs and 2 ms.

5.2.4 Mass Spectroscopy (MS)

The ESI (Electrospray Ionization) MS experiments were performed using a Bruker Esquire 3000 PLUS (ESI Ion Trap LC/MSn System), equipped with an ESI source and a quadrupole ion trap detector (QIT). Some acquisition parameters are 4.5 kV of needle voltage and 40 V of cone voltage, with nitrogen flow rate of 10 L/h. Scan resolution was 13 000 (m/z)/s over the mass range m/z 35–900, obtained by direct infusion of methanol solution (1 mg/1 mL) of compounds at rate 4 μL/min. The assignment of some of species detected was confirmed by collision-activated decomposition (CID) mass spectrometry experiments (MS^2).

5.2.5 X-Ray Powder Diffraction (XRPD)

Powder X-ray diffraction data were collected on Brucker AXS D8 powder diffractometer with experimental diffractometer as follows: Cu-Kα radiation (λ = 1.5418 Å), scanning interval 3.5°–60° at 2θ, step size 0.015°, exposure time 1.5 s per step.

5.2.6 Single-Crystal X-Ray Diffraction (SC-XRD)

Data collection was performed with a Bruker Kappa Apex II diffractometer equipped with a sealed tube detector and CCD, using Mo-Kα radiation (λ = 0.71073 Å). Data collection was performed at room temperature. The diffraction data was indexed, integrated and scaled using SAINT. The structures were solved by SHELXS and refinements were performed from least squares to full matrix on F^2 using the SHELXL program. Anisotropic thermal motion refinement has been used for all atoms. Hydrogen atoms were included at calculated positions. Pictures were prepared using CCDC Mercury software. Essential crystal and refinement data are reported below (Table 44, Table 45 and Table 46).

Table 44. *Crystallographic data for IAI compound.*

Crystal data	**Chemical formula**	$C_6H_7I_2N$
	M_r	346.94
	Crystal system, space group	Monoclinic, *P*2/*n*
	Temperature [K]	100
	***a*, *b*, *c* [Å]**	10.2989 (9), 10.6394 (10), 16.8837 (16)
	β [°]	93.606 (6)
	***V* [Å³]**	1846.4 (3)
	Z	8
	Radiation type	Mo *Kα*
	μ [mm⁻¹]	6.74
Data collection	**Diffractometer**	Bruker *APEX*-II CCD
	No. of measured, independent and observed [$I \geq 2u(I)$] reflections	17315, 5629, 4069
	R_{int}	0.045
	(sin θ/λ)$_{max}$ [Å⁻¹]	0.715
Refinement	$R[F^2 > 2\sigma(F^2)]$, $wR(F^2)$, S	0.033, 0.062, 0.98
	No. of reflections	5629
	No. of parameters	167
	H-atom treatment	H-atom parameters constrained
	Δϱ$_{max}$, Δϱ$_{min}$ [e Å⁻³]	1.86, −1.46

Table 45. *Crystallographic data for $(IA)_2PbI_4$ compound.*

Crystal data	**Chemical formula**	**$I_2Pb_{0.5}{\cdot}C_6H_7IN$**
	***M*r**	577.42
	Crystal system, space group	Monoclinic, $P2_1/c$
	Temperature [K]	296
	***a*, *b*, *c* [Å]**	15.747 (3), 8.2898 (12), 9.1526 (15)
	β [°]	100.200 (8)
	***V* [Å^3]**	1175.9 (3)
	Z	4
	Radiation type	Mo $K\alpha$
	μ [mm^{-1}]	15.05
Data collection	**Diffractometer**	Bruker *APEX*-II CCD
	No. of measured, independent and observed [$I \geq 2u(I)$] reflections	11826, 3323, 2526
	R_{int}	0.052
	$(\sin \theta/\lambda)_{max}$ [Å^{-1}]	0.697
Refinement	**$R[F^2 > 2\sigma(F^2)]$, $wR(F^2)$, S**	0.046, 0.120, 1.09
	No. of reflections	3323
	No. of parameters	98
	H-atom treatment	H-atom parameters constrained
	$\Delta\varrho_{max}$, $\Delta\varrho_{min}$ [e Å^{-3}]	3.04, −1.22

Table 46. *Crystallographic data for I-FEA compound.*

Crystal data	**Chemical formula**	$C_8H_7F_4IN_2$
	M_r	334.06
	Crystal system, space group	Triclinic, *P*1
	Temperature [K]	296
	***a*, *b*, *c* [Å]**	4.8136 (3), 6.1647 (4), 8.5834 (5)
	β [°]	92.719 (3), 99.016 (3), 91.636 (3)
	***V* [Å³]**	251.11 (3)
	Z	1
	Radiation type	Mo *Kα*
	μ [mm⁻¹]	3.21
Data collection	**Diffractometer**	Bruker *APEX*-II CCD
	No. of measured, independent and observed [$I \geq 2u(I)$] reflections	5072, 2827, 2824
	R_{int}	0.021
	(sin θ/λ)$_{max}$ [Å⁻¹]	0.720
Refinement	$R[F^2 > 2\sigma(F^2)]$, $wR(F^2)$, S	0.021, 0.053, 1.07
	No. of reflections	2827
	No. of parameters	146
	No. of restraints	4
	H-atom treatment	H atoms treated by a mixture of independent and constrained refinement
	Δϱ$_{max}$, Δϱ$_{min}$ [e Å⁻³]	0.51, −0.38

5.2.7 Fourier Transform Infrared (FT-IR) Spectroscopy

Varian 640-IR was used to perform FT-IR measurements. Transmittance scanning type selected with laser wavelength of 632.8 nm. PIKE Technologies MIRacle accessory allowed for attenuated total reflectance (ATR) mode analysis. The samples were placed onto ZnSe crystal plate and pressed hard against it by flat pressure tip. Dry nitrogen was used as purge gas. Varian Resolution Pro Software was used to elaborate data. All spectra were collected with 64 scans in 400-4000 cm^{-1} wavenumber range.

5.2.8 Raman Spectroscopy

The Horiba Jobin Yvon LabRAM HR800 UV system was used as Raman spectrometer. All the sample were excited with a laser of 632.81 nm wavelength through a Melles Griot 05-LHP-927 He-Ne laser. Spectra were collected in the spectral range of 80-4000 cm^{-1} with a power of 1 mW. Each spectrum was obtained with 7 acquisitions in 10 s of integration time each.

5.2.9 Optical Microscope

Binocular Olympus BX41 Microscope was used to verify the crystallinity of single-crystal samples. The same optical microscope model was mounted onto Raman spectrometer with a camera allowing the precise placement and focus of sample and laser beam.

5.2.10 X-Ray Photoelectron Spectroscopy (XPS)

Surface composition of samples was analyzed through a M-PROBE surface spectrometer with a source of Al (Kα) and with a spot between 0.15 mm and 1 mm of diameter size. An applied voltage of 10 V and high vacuum (10^{-7}-10^{-8} Torr) were used. Scanning was made in a range of binding energy 0-1100 eV, using a spot of 800 μm of

diameter size, with an energetic resolution of 4eV. ESCA Hawk software was used to analyze data.

5.2.11 Thermogravimetric Analysis (TGA)

TGA was employed to study degradation temperature of samples and to verify their stoichiometry. TA Instruments Q500 and TA Instruments Software were used to perform TGA and to elaborate data. Aluminum standard pans (75 μL) were used for samples insertion in the furnace.

5.2.12 Differential Scanning Calorimetry (DSC)

DSC analyses were performed by Mettler Toledo DSC823^e instrument at a scan rate of 10K/min in sealed aluminum standard crucibles (40 μL) under air. An electrical resistance and nitrogen cooling system controlled the temperature. The furnace temperature was in the maximum range of -225K and 573K for these samples. STAR^e Software (Version 12.10) was used for data elaboration.

5.2.13 UV-vis Absorption Measurements

The absorption spectra were recorded using a Varian Cary 50 spectrophotometer.

5.2.14 Photoluminescence (PL) Measurements

The photoluminescence measurements were performed using a pulsed diode laser at 355 nm (Edinburg Inst. EPL 405, 40 ps pulse width) as excitation source and collecting the emitted light with a charged coupled device coupled to a spectrometer. Time-resolved photoluminescence experiments were conducted using the excitation source and collecting with a time-correlated single photon counting unit coupled to a monochromator and a photomultiplier tube. All PL measurements were performed

with power density of 100 nJ/cm^2. Measurements were carried out at room temperature for all samples and in the temperature range 20K-300K for (I-FEA)$_2$PbI$_4$.

6. Conclusion and Outlook

Novel 2D perovskites containing XB-donor cations with different XB-donor ability have been synthesized and characterized. In particular, 4-iodoanilinium (IA^+) and (4-X-2,3,5,6-tetrafluoroaniline)-ethan-1-ammonium (X-FEA^+, with X = Cl, Br, I) have been selected as cations taking into account their XB-donor ability. The former was expected to be the weakest XB-donor, while X-FEA^+, due to ring fluorination, should have behaved as stronger XB-donors.

X-ray crystal structure of perovskite containing IA^+ cation showed the presence of a 2D layered structure, corresponding to $(IA^+)_2PbI_4^{2-}$ molecular formula, with corner-sharing PbI_6 octahedra layers alternated to IA^+ sheets. The cations form a very weak XB with inorganic sublattice, too weak to influence the structure.
XRPD spectra of perovskite containing X-FEA^+ cations suggested a similar 2D structure. Here, the occurrence of XB between cations and inorganic layers has great effects on crystal structure. In fact, the stronger is the interaction, the shorter is the distance between inorganic layers, despite the enlargement of cation. Vibrational spectroscopy, NMR and XPS demonstrated the presence of an intense XB in $(I\text{-}FEA)_2PbI_4$.

In addition, SS-NMR allowed to make some hypotheses about perovskite structure and suggested the possibility of high mobility of cations inside $(I\text{-}FEA)_2PbI_4$ structure, strictly correlated to the strength of XB interaction. According to the assumption, cations behave as bidentate ligands within the inorganic layers, with the ammonium moiety interacting with an inorganic sheet and the XB-donor group interacting through XB with the parallel inorganic sheet. In this way, the aromatic ring could be "free" to rotate, acting as a molecular rotor. Amphidynamic crystals, built with a

combination of static components that guide crystalline order, generally linked to dynamic elements that display conformational motion along well-defined directions, offer a platform to realize controlled dynamics and to modulate the functions of solids. Hence, their fabrication gained increased interest, but it has not been explored in depth yet.[98,99] The supposed rotational dynamics of I-FEA cations in perovskites should be further investigated by ^{1}H spin-lattice relaxation (T_1) experiment at variable temperature, in order to analyze the relaxation time of each atom in the organic cations and relate it to their mobility.

Moreover, since SC-XRD analysis did not allow to identify the crystalline structure of $(I\text{-}FEA)_2PbI_4$, even at low temperature (100K), synchrotron would be an essential tool for structure understanding.

Finally, the main technological application of the synthesized 2D perovskites could be the passivation of 3D layer surface/grain boundaries in perovskite-based photovoltaics or, after a more in-depth photophysical characterization, they could be applied in the fabrication of other stable optoelectronic devices. Another unexplored possible application of $(X\text{-}FEA)_2PbI_4$ materials is strictly related to their crystalline structure. If X-FEA cations were arranged such to have enough space for heavy noble gas molecules to be absorbed, these 2D perovskites would be used as gas sensors, behaving as task-specific porous materials.[100]

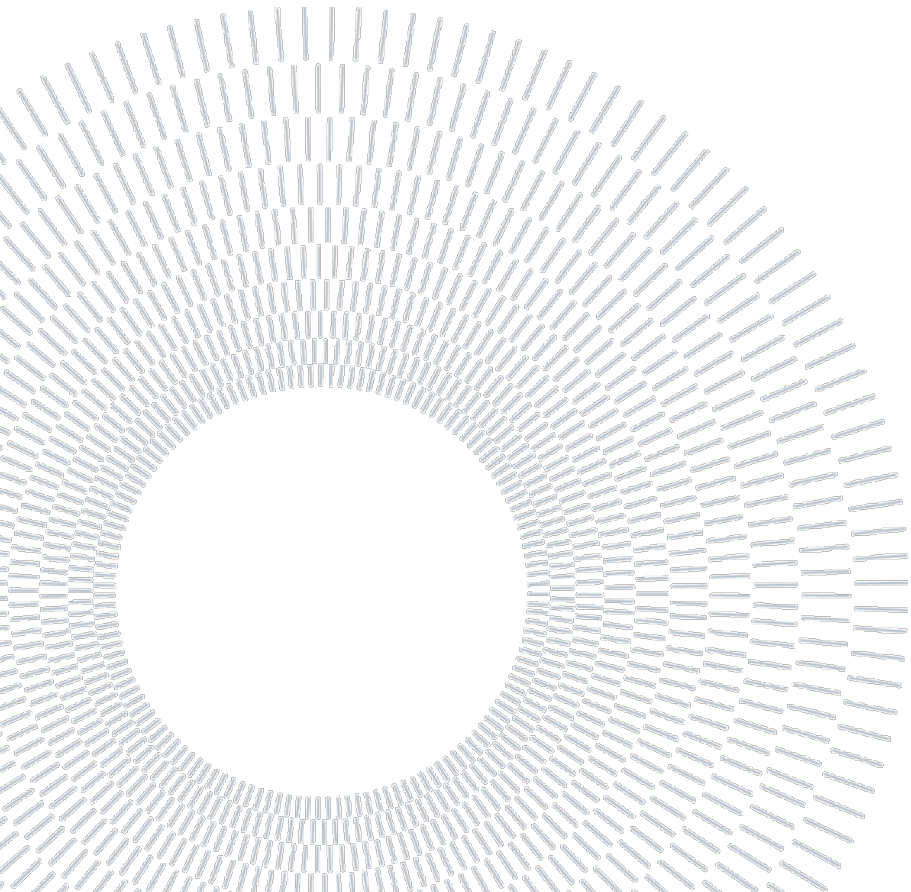

Bibliography

1. Gao, P., Grätzel, M. & Nazeeruddin, M. K. Organohalide lead perovskites for photovoltaic applications. *Energy Environ. Sci.* **7**, 2448–2463 (2014).
2. Ozório, M. S., Srikanth, M., Besse, R. & Da Silva, J. L. F. The role of the A-cations in the polymorphic stability and optoelectronic properties of lead-free ASnI3perovskites. *Phys. Chem. Chem. Phys.* **23**, 2286–2297 (2021).
3. Kim, H. S., Im, S. H. & Park, N. G. Organolead halide perovskite: New horizons in solar cell research. *J. Phys. Chem. C* **118**, 5615–5625 (2014).
4. Li, C. *et al.* Formability of ABX 3 (X = F, Cl, Br, I) halide perovskites. *Acta Crystallogr. Sect. B Struct. Sci.* **64**, 702–707 (2008).
5. Zhu, M. *et al.* Interaction engineering in organic-inorganic hybrid perovskite solar cells. *Mater. Horizons* **7**, 2208–2236 (2020).
6. Zhang, F. *et al.* Advances in two-dimensional organic-inorganic hybrid perovskites. *Energy Environ. Sci.* **13**, 1154–1186 (2020).
7. Liu, D. *et al.* Metal halide perovskite nanocrystals: application in high-performance photodetectors. *Mater. Adv.* **2**, 856–879 (2021).
8. Saliba, M. *et al.* A molecularly engineered hole-transporting material for efficient perovskite solar cells. *Nat. Energy* **1**, 1–7 (2016).
9. Yang, W. S. *et al.* High-performance photovoltaic perovskite layers fabricated through intramolecular exchange. *Science (80-.).* **348**, 1234–1237 (2015).
10. Chen, J., Zhou, S., Jin, S., Li, H. & Zhai, T. Crystal organometal halide perovskites with promising optoelectronic applications. *J. Mater. Chem. C* **4**, 11–27 (2015).
11. Zakutayev, A. *et al.* Defect tolerant semiconductors for solar energy conversion. *J. Phys. Chem. Lett.* **5**, 1117–1125 (2014).
12. Rincón, C. & Márquez, R. Defect physics of the CuInSe2 chalcopyrite semiconductor. *J. Phys. Chem. Solids* **60**, 1865–1873 (1999).

13. Brandt, R. E., Stevanović, V., Ginley, D. S. & Buonassisi, T. Identifying defect-tolerant semiconductors with high minority-carrier lifetimes: Beyond hybrid lead halide perovskites. *MRS Commun.* **5**, 265–275 (2015).

14. Agranovich, V. M., Basko, D. M., La Rocca, G. C. & Bassani, F. Excitons and optical nonlinearities in hybrid organic-inorganic nanostructures. *J. Phys. Condens. Matter* **10**, 9369–9400 (1998).

15. Basko, D., La Rocca, G. C., Bassani, F. & Agranovich, V. M. Förster energy transfer from a semiconductor quantum well to an organic material overlayer. *Eur. Phys. J. B* **8**, 353–362 (1999).

16. Yin, W. J., Shi, T. & Yan, Y. Unusual defect physics in CH3NH3PbI3 perovskite solar cell absorber. *Appl. Phys. Lett.* **104**, (2014).

17. Yang, W. S. *et al.* Iodide management in formamidinium-lead-halide-based perovskite layers for efficient solar cells. *Science (80-.).* **356**, 1376–1379 (2017).

18. Fu, F. *et al.* I2 vapor-induced degradation of formamidinium lead iodide based perovskite solar cells under heat-light soaking conditions. *Energy Environ. Sci.* **12**, 3074–3088 (2019).

19. Wang, S., Jiang, Y., Juarez-Perez, E. J., Ono, L. K. & Qi, Y. Accelerated degradation of methylammonium lead iodide perovskites induced by exposure to iodine vapour. *Nat. Energy* **2**, (2017).

20. Tumen-Ulzii, G. *et al.* Detrimental Effect of Unreacted PbI2 on the Long-Term Stability of Perovskite Solar Cells. *Adv. Mater.* **32**, 1–7 (2020).

21. Juarez-Perez, E. J. *et al.* Photodecomposition and thermal decomposition in methylammonium halide lead perovskites and inferred design principles to increase photovoltaic device stability. *J. Mater. Chem. A* **6**, 9604–9612 (2018).

22. Sha, W. E. I., Ren, X., Chen, L. & Choy, W. C. H. The efficiency limit of CH3NH3PbI3 perovskite solar cells. *Appl. Phys. Lett.* **106**, (2015).

23. Wang, X. *et al.* Recent progress in organometal halide perovskite photodetectors. *Org. Electron.* **52**, 172–183 (2018).

24. Akbulatov, A. F. *et al.* Light or Heat: What Is Killing Lead Halide Perovskites under Solar Cell Operation Conditions? *J. Phys. Chem. Lett.* **11**, 333–339 (2020).

25. Han, Y., Yue, S. & Cui, B. Bin. Low-Dimensional Metal Halide Perovskite Crystal Materials: Structure Strategies and Luminescence Applications. *Adv. Sci.* **8**, 1–21 (2021).

26. Jiang, X. *et al.* Dion-Jacobson 2D-3D perovskite solar cells with improved efficiency and stability. *Nano Energy* **75**, 104892 (2020).

27. Fu, X. *et al.* Halogen-halogen bonds enable improved long-term operational stability of mixed-halide perovskite photovoltaics. *Chem* **7**, 3131–3143 (2021).

28. Smith, M. D. & Karunadasa, H. I. White-Light Emission from Layered Halide Perovskites. *Acc. Chem. Res.* **51**, 619–627 (2018).

29. Selivanov, N. I., Rozhkova, Y. A., Kevorkyants, R., Emeline, A. V. & Bahnemann, D. W. The effect of organic cations on the electronic, optical and luminescence properties of 1D piperidinium, pyridinium, and 3-hydroxypyridinium lead trihalides. *Dalt. Trans.* **49**, 4390–4403 (2020).

30. Wong, J. & Yang, K. 2D Hybrid Halide Perovskites: Synthesis, Properties, and Applications. *Sol. RRL* **5**, 53–56 (2021).

31. Li, X., Hoffman, J. M. & Kanatzidis, M. G. The 2D halide perovskite rulebook: How the spacer influences everything from the structure to optoelectronic device efficiency. *Chem. Rev.* **121**, 2230–2291 (2021).

32. Tremblay, M. H. *et al.* Structures of (4-Y-C6H4CH2NH3)2PbI4 {Y = H, F, Cl, Br, I}: Tuning of Hybrid Organic Inorganic Perovskite Structures from Ruddlesden-Popper to Dion-Jacobson Limits. *Chem. Mater.* **31**, 6145–6153 (2019).

33. Mao, L., Stoumpos, C. C. & Kanatzidis, M. G. Two-Dimensional Hybrid Halide Perovskites: Principles and Promises. *J. Am. Chem. Soc.* **141**, 1171–1190 (2019).

34. Stoumpos, C. C. *et al.* Ruddlesden-Popper Hybrid Lead Iodide Perovskite 2D Homologous Semiconductors. *Chem. Mater.* **28**, 2852–2867 (2016).

35. Mao, L. *et al.* Hybrid Dion-Jacobson 2D Lead Iodide Perovskites. *J. Am. Chem. Soc.* **140**, 3775–3783 (2018).

36. Straus, D. B. & Kagan, C. R. Electrons, Excitons, and Phonons in Two-Dimensional Hybrid Perovskites: Connecting Structural, Optical, and Electronic Properties. *J. Phys. Chem. Lett.* **9**, 1434–1447 (2018).

37. Fu, Y. *et al.* Cation Engineering in Two-Dimensional Ruddlesden-Popper Lead Iodide Perovskites with Mixed Large A-Site Cations in the Cages. *J. Am. Chem. Soc.* **142**, 4008–4021 (2020).

38. Passarelli, J. V. *et al.* Tunable exciton binding energy in 2D hybrid layered perovskites through donor–acceptor interactions within the organic layer. *Nat. Chem.* **12**, 672–682 (2020).

39. Neogi, I. *et al.* Broadband-Emitting 2 D Hybrid Organic–Inorganic Perovskite Based on Cyclohexane-bis(methylamonium) Cation. *ChemSusChem* **10**, 3765–3772 (2017).

40. Alberto García-Fernández, Juan Manuel Bermúdez-García, Socorro Castro-García, Antonio Luis Llamas-Saiz, Ramón Artiaga, Jorge José López-Beceiro, Manuel Sánchez-Andújar, and M. A. S.-R. [(CH3)2NH2]7Pb4X15 (X = Cl– and Br–), 2D-Perovskite Related Hybrids with Dielectric Transitions and Broadband Photoluminiscent Emission. *Inorg. Chem.* **57**, 3215–3222 (2018).

41. Lingling Mao, Yilei Wu, Constantinos C. Stoumpos, Michael R. Wasielewski, and M. G. K. White-Light Emission and Structural Distortion in New Corrugated Two-Dimensional Lead Bromide Perovskites. *Inorg. Chem.* **137**, 5210–5215 (2017).

42. Mao, L. *et al.* Structural Diversity in White-Light-Emitting Hybrid Lead Bromide Perovskites. *J. Am. Chem. Soc.* **140**, 13078–13088 (2018).

43. Kamminga, M. E. *et al.* Confinement Effects in Low-Dimensional Lead Iodide Perovskite Hybrids. *Chem. Mater.* **28**, 4554–4562 (2016).

44. Kamminga, M. E., De Wijs, G. A., Havenith, R. W. A., Blake, G. R. & Palstra, T. T. M. The Role of Connectivity on Electronic Properties of Lead Iodide Perovskite-Derived Compounds. *Inorg. Chem.* **56**, 8408–8414 (2017).

45. Fabini, D. H. *et al.* Dynamic Stereochemical Activity of the Sn2+ Lone Pair in Perovskite CsSnBr3. *J. Am. Chem. Soc.* **138**, 11820–11832 (2016).

46. Zhang, H. Y., Zhang, Z. X., Song, X. J., Chen, X. G. & Xiong, R. G. Two-Dimensional Hybrid Perovskite Ferroelectric Induced by Perfluorinated Substitution. *J. Am. Chem. Soc.* **142**, 20208–20215 (2020).

47. Du, K. Z. *et al.* Two-Dimensional Lead(II) Halide-Based Hybrid Perovskites Templated by Acene Alkylamines: Crystal Structures, Optical Properties, and Piezoelectricity. *Inorg. Chem.* **56**, 9291–9302 (2017).

48. Rodríguez-Romero, J. *et al.* Tuning optical/electrical properties of 2D/3D perovskite by the inclusion of aromatic cation. *Phys. Chem. Chem. Phys.* **20**, 30189–30199 (2018).

49. Passarelli, J. V. *et al.* Enhanced Out-of-Plane Conductivity and Photovoltaic Performance in n = 1 Layered Perovskites through Organic Cation Design. *J. Am. Chem. Soc.* **140**, 7313–7323 (2018).

50. Jeremy L. Knutson, James D. Martin, and D. B. M. Tuning the Band Gap in Hybrid Tin Iodide Perovskite Semiconductors Using Structural Templating.

Inorg. Chem. **44**, 4699–4705 (2005).

51. Paek, S. *et al.* Molecular Design and Operational Stability: Toward Stable 3D/2D Perovskite Interlayers. *Adv. Sci.* **7**, 1–11 (2020).

52. Shi, P. P. *et al.* Two-Dimensional Organic-Inorganic Perovskite Ferroelectric Semiconductors with Fluorinated Aromatic Spacers. *J. Am. Chem. Soc.* **141**, 18334–18340 (2019).

53. Du, Y. *et al.* Dendritic PAMAM polymers for strong perovskite intergranular interaction enhancing power conversion efficiency and stability of perovskite solar cells. *Electrochim. Acta* **349**, 136387 (2020).

54. Yao, K., Wang, X., Xu, Y. X., Li, F. & Zhou, L. Multilayered Perovskite Materials Based on Polymeric-Ammonium Cations for Stable Large-Area Solar Cell. *Chem. Mater.* **28**, 3131–3138 (2016).

55. Dohner, E. R., Hoke, E. T. & Karunadasa, H. I. Self-Assembly of Broadband White-Light Emitters. 2–5 (2014).

56. Guo, Y. *et al.* Phenylalkylammonium passivation enables perovskite light emitting diodes with record high-radiance operational lifetime: the chain length matters. *Nat. Commun.* **12**, (2021).

57. Proppe, A. H. *et al.* Photochemically Cross-Linked Quantum Well Ligands for 2D/3D Perovskite Photovoltaics with Improved Photovoltage and Stability. *J. Am. Chem. Soc.* **141**, 14180–14189 (2019).

58. Zhang, L. *et al.* Ultra-long photoluminescence lifetime in an inorganic halide perovskite thin film. *J. Mater. Chem. A* **7**, 22229–22234 (2019).

59. Nakita K. Noel, Antonio Abate, Samuel D. Stranks, Elizabeth S. Parrott, Victor M. Burlakov, Alain Goriely, and H. J. S. Enhanced Photoluminescence and Solar Cell Performance via Lewis Base Passivation of Organic–Inorganic Lead Halide Perovskites. *ACS Nano* **8**, 9815–9821 (2014).

60. Liu, L., Fang, W. H., Long, R. & Prezhdo, O. V. Lewis Base Passivation of Hybrid Halide Perovskites Slows Electron-Hole Recombination: Time-Domain Ab Initio Analysis. *J. Phys. Chem. Lett.* **9**, 1164–1171 (2018).

61. Xiong, J. *et al.* Efficient and stable perovskite solar cells via shortwave infrared polymer passivation. *Sol. Energy Mater. Sol. Cells* **220**, 110862 (2021).

62. Li, B. *et al.* Surface passivation engineering strategy to fully-inorganic cubic CsPbI3 perovskites for high-performance solar cells. *Nat. Commun.* **9**, 1–8 (2018).

63. Xiong Hao, Giovanni DeLuca, Yichuan Rui, Boxin Zhang, Yaogang Li, Qinghong Zhang, Hongzhi Wang, and E. R. Modifying Perovskite Films with Polyvinylpyrrolidone for Ambient-Air-Stable Highly Bendable Solar Cells. *ACS Appl. Mater. Interfaces* **10**, 35385–35394 (2018).

64. Fairfield, D. J. *et al.* Structure and chemical stability in perovskite-polymer hybrid photovoltaic materials. *J. Mater. Chem. A* **7**, 1687–1699 (2019).

65. Song, D. *et al.* Dual function interfacial layer for highly efficient and stable lead halide perovskite solar cells. *J. Mater. Chem. A* **4**, 6091–6097 (2016).

66. Xu, J. *et al.* Perovskite-fullerene hybrid materials suppress hysteresis in planar diodes. *Nat. Commun.* **6**, 1–8 (2015).

67. Steven E. Wheeler & K.N. Houk. Origin of substituent effects in edge-to-face aryl–aryl interactions. *Mol. Phys.* **107**, 749–760 (2009).

68. Lin, Y. *et al.* π-Conjugated Lewis Base: Efficient Trap-Passivation and Charge-Extraction for Hybrid Perovskite Solar Cells. *Adv. Mater.* **29**, 1–6 (2017).

69. Hu, J. *et al.* Aryl-Perfluoroaryl Interaction in Two-Dimensional Organic-Inorganic Hybrid Perovskites Boosts Stability and Photovoltaic Efficiency. *ACS Mater. Lett.* **1**, 171–176 (2019).

70. Straus, D. B. *et al.* Longer Cations Increase Energetic Disorder in Excitonic 2D Hybrid Perovskites. *J. Phys. Chem. Lett.* **10**, 1198–1205 (2019).

71. Hassel, O., Hvoslef, J., Vihovde, E. H. & Sörensen, N. A. The Structure of Bromine 1,4-Dioxanate. *Acta Chemica Scandinavica* vol. 8 873–873 (1954).

72. Metrangolo, P., Meyer, F., Pilati, T., Resnati, G. & Terraneo, G. Halogen bonding in supramolecular chemistry. *Angew. Chemie - Int. Ed.* **47**, 6114–6127 (2008).

73. Rissanen, K. Halogen bonded supramolecular complexes and networks. *CrystEngComm* **10**, 1107–1113 (2008).

74. Saccone, M. & Catalano, L. Halogen Bonding beyond Crystals in Materials Science. *J. Phys. Chem. B* **123**, 9281–9290 (2019).

75. Priimagi, A., Cavallo, G., Metrangolo, P. & Resnati, G. The Halogen Bond in the Design of Functional Supramolecular Materials: Recent Advances. *Acc. Chem. Res.* **46**, 2686–2695 (2013).

76. Cavallo, G. *et al.* The halogen bond. *Chem. Rev.* **116**, 2478–2601 (2016).

77. Metrangolo, P., Canil, L., Abate, A., Terraneo, G. & Cavallo, G. Halogen Bonding

in Perovskite Solar Cells: A New Tool for Improving Solar Energy Conversion. *Angew. Chemie* (2021) doi:10.1002/ange.202114793.

78. Abate, A. *et al.* Supramolecular halogen bond passivation of organic-inorganic halide perovskite solar cells. *Nano Lett.* **14**, 3247–3254 (2014).

79. Ruiz-Preciado, M. A. *et al.* Supramolecular Modulation of Hybrid Perovskite Solar Cells via Bifunctional Halogen Bonding Revealed by Two-Dimensional 19F Solid-State NMR Spectroscopy. *J. Am. Chem. Soc.* **142**, 1645–1654 (2020).

80. Bi, S. *et al.* Halogen bonding reduces intrinsic traps and enhances charge mobilities in halide perovskite solar cells. *J. Mater. Chem. A* **7**, 6840–6848 (2019).

81. Wolff, C. M. *et al.* Perfluorinated Self-Assembled Monolayers Enhance the Stability and Efficiency of Inverted Perovskite Solar Cells. *ACS Nano* **14**, 1445–1456 (2020).

82. Zhang, L. & Chen, Y. Atomistic understanding on molecular halide perovskite/organic/TiO2 interface with bifunctional interfacial modifier: A case study on halogen bond and carboxylic acid group. *Appl. Surf. Sci.* **502**, 3–10 (2020).

83. Papavassilioua, G. C., Mousdisa, G. A., Raptopouloub, C. P. & Terzisb, A. Organic-Inorganic Hybrid Compounds. 3–7 (1999).

84. Bondi, A. Van der Waals Volumes and Radii. *J. Phys. Chem.* **68**, 441–451 (1964).

85. Shannon, R. D. Revised Effective Ionic Radii and Systematic Studies of Interatomic Distances in Halides and Chalcogenides. *Acta Crystallogr. Sect. A* **A32**, 751–767 (1976).

86. Dai, H. *et al.* Crystal structure of bis(4-bromophenylaminium) tetraiodoplumbate(II), (BrC6H4NHa)2PbI4. *Zeitschrift fur Krist. - New Cryst. Struct.* **224**, 149–150 (2009).

87. Vijaya Prakash, G. *et al.* Structural and optical studies of local disorder sensitivity in natural organic-inorganic self-assembled semiconductors. *J. Phys. D. Appl. Phys.* **42**, (2009).

88. García-Benito, I. *et al.* Fashioning Fluorous Organic Spacers for Tunable and Stable Layered Hybrid Perovskites. *Chem. Mater.* **30**, 8211–8220 (2018).

89. Messina, M. T. *et al.* Infrared and Raman analyses of the halogen-bonded non-covalent adducts formed by α,ω-diiodoperfluoroalkanes with DABCO and other electron donors. *J. Mol. Struct.* **524**, 87–94 (2000).

90. Dey, A., Jetti, R. K. R., Boese, R. & Desiraju, G. R. Supramolecular equivalence of halogen, ethynyl and hydroxy groups. A comparison of the crystal structures of some 4-substituted anilines. *CrystEngComm* **5**, 248–252 (2003).

91. John, N. L., Abraham, S., Sajan, D., Sarojini, B. K. & Narayana, B. Quantum chemical studies of molecular structure, vibrational spectra and nonlinear optical properties of p-iodoaniline and p-bromoaniline. *J. Mol. Struct.* **1222**, 128939 (2020).

92. Abate, A. *et al.* Halide anions driven self-assembly of haloperfluoroarenes: Formation of one-dimensional non-covalent copolymers. *J. Fluor. Chem.* **130**, 1171–1177 (2009).

93. Allen, K. A Raman Spectroscopic and Computational Study on the Effects of Electron Withdrawing Groups on Halogen Bonding. (University of Mississippi, 2017).

94. Sheikh, T., Shinde, A., Mahamuni, S. & Nag, A. Possible Dual Bandgap in (C4H9NH3)2PbI4 2D Layered Perovskite: Single-Crystal and Exfoliated Few-Layer. *ACS Energy Lett.* **3**, 2940–2946 (2018).

95. Jacek Karwowski. Assignment of the electronic transitions in benzene. *J. Mol. Struct.* **19**, 143–166 (1973).

96. Wan, K. M. *et al.* Investigation of thermochromic photoluminescent, dielectric and crystal structural properties for an inorganic-organic hybrid solid of [1-hexyl-3-methylimidazolium][PbBr3]. *New J. Chem.* **40**, 8664–8672 (2016).

97. Tong, Y. B., Ren, L. Te, Duan, H. B., Liu, J. L. & Ren, X. M. An amphidynamic inorganic-organic hybrid crystal of bromoplumbate with 1,5-bis(1-methylimidazolium)pentane exhibiting multi-functionality of a dielectric anomaly and temperature-dependent dual band emissions. *Dalt. Trans.* **44**, 17850–17858 (2015).

98. De Nicola, A. *et al.* Collective dynamics of molecular rotors in periodic mesoporous organosilica: a combined solid-state 2 H-NMR and molecular dynamics simulation study . *Phys. Chem. Chem. Phys.* **24**, 666–673 (2022).

99. Catalano, L. *et al.* Rotational dynamics of diazabicyclo[2.2.2]octane in isomorphous halogen-bonded co-crystals: Entropic and enthalpic effects. *J. Am. Chem. Soc.* **139**, 843–848 (2017).

100. Pizzi, A. *et al.* Tight Xenon Confinement in a Crystalline Sandwich-like Hydrogen-Bonded Dimeric Capsule of a Cyclic Peptide. *Angew. Chemie - Int. Ed.*

58, 14472–14476 (2019).

Appendix

Table 47. *List of abbraviations used in Table 1 and Table 2*.[30]

Acronym	Complete name
BA	Butylammonium
PEA	Phenylethylammonium
AMP	m-(Aminomethyl)piperidinium
GA	Guanidinium
DA	Dodecylammonium
HDA	n-Hexadecylammonium
ODA	n-Octadecylammonium
CA	Cyclopropylammonium
CHE	2-Cyclohexenylethanamine
CBA	Cyclobutylammonium
CPE	Cyclopentylammonium
DDA	Dodecyl diammonium
CM	Cyclohexylmethanamine
PMA	Phenylmethanammonium
TPM	2-Thiophenemethylamine
TFM	(Tetrahydrofuran-2-yl)methanamine
MFM	5-Methyl-2-furanmethanamine
BZA	Benzylammonium
PEA	Phenylethylammonium
MA	Methylammonium
BDA	1,4-Butanediammonium
PEIM	Phenylethanimidamidine
DMEN	2-(Dimethylamino)-ethylammonium

DMAPA	3-(Dimethylamino)-1-propylamine
DMABA	4-Dimethylaminobutylammonium
EDBE	2,20- (Ethylenedioxy)-bis(ethylammonium)
HIA	Histammonium

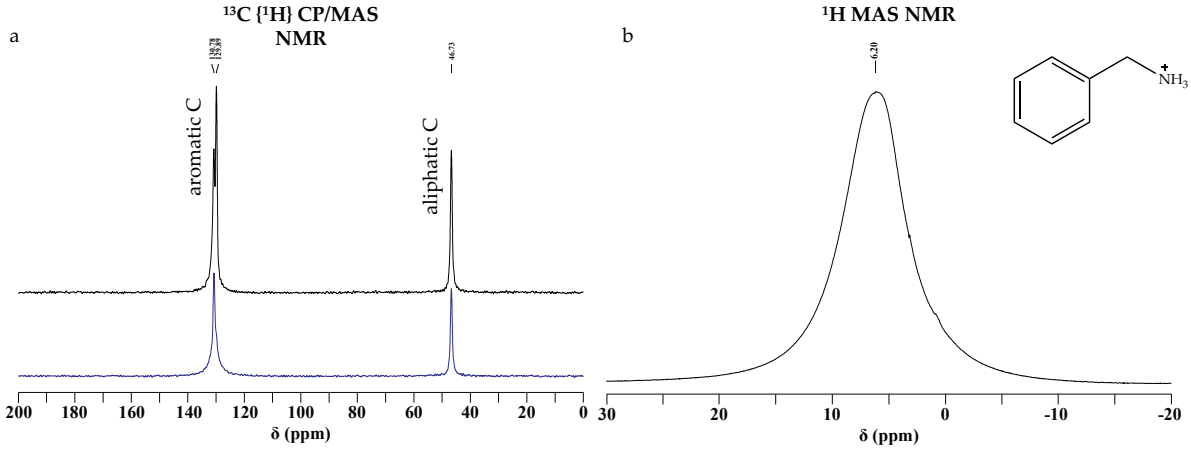

Figure 129. *SS-NMR spectra of $(BA)_2PbI_4$ compound.*

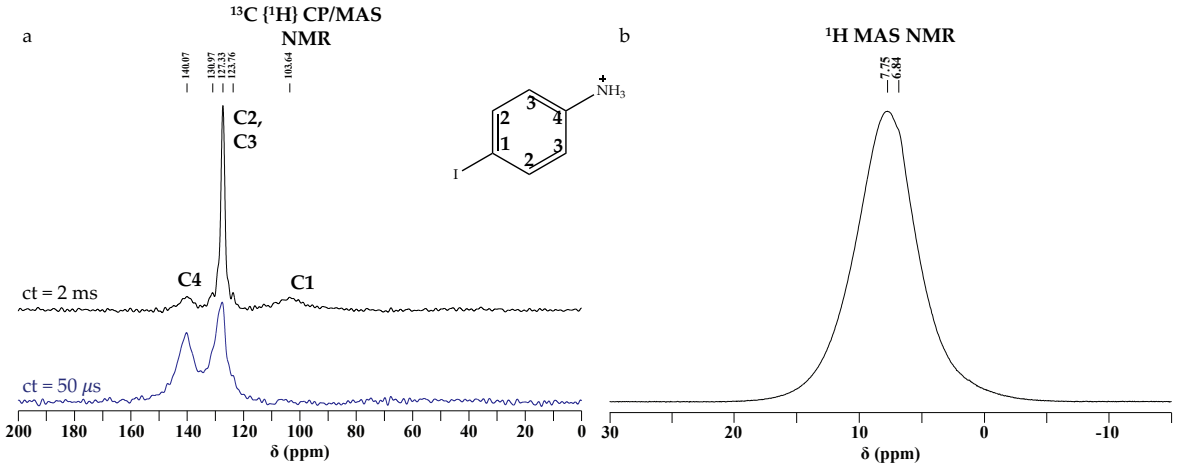

Figure 130. *SS-NMR spectra of $(IA)_2PbI_4$ compound*

List of Figures

List of Tables

Acknowledgements

This work was fulfilled thanks to the valuable contributions of Università degli Studi di Milano Bicocca (UniMib) and Università degli Studi di Milano Statale (UniMi). In particular, grateful acknowledgments to Prof. S. Bracco and Ph.D. student S. Piva for SS-NMR experiments, to Prof. S. Brovelli, Dr. V. Pinchetti and Dr. M. L. Zaffalon for optical measurements, and to Dr. M. Schiavoni for XPS analyses.

Warm thanks also to Prof. M. M. S. Tommasini and Prof. A. Lucotti, W. Panzeri and M. Ferro from Politecnico di Milano (PoliMi) for helping in Raman spectroscopy, MS and SS-NMR analyses.

Finally, the greatest thanks goes to all the members of SupraBioNanoLab (SBNlab), especially to Prof. G. Cavallo, that, besides her role of supervisor, has always been helpful and patient, to Prof. G. Terraneo for SC-XRD analyses, to Prof. P. Metrangolo for helping in data interpretation, and to D. Ricci, for sharing time and ideas together.